

# **Integrated Physics-based Modeling and Experiments for Improved Prediction of Combustion Dynamics in Low-Emission Systems**

*William E. Anderson  
Purdue University, West Lafayette IN*

*Robert P. Lucht  
Purdue University, West Lafayette IN*

*Hukam Mongia  
Purdue University, West Lafayette IN*

Prepared under contract NNX11AI62A

**JANUARY 2015**

## Acknowledgments

This work was done under NASA Research Announcement (NRA) grant number NNX11AI62A with Kimlam Pham and Julie Fowler as Program Managers, and Kevin Breisacher of NASA Glenn Research Center as Technical Monitor. Additional financial support through a fellowship was provided by John Zink Company. Graduate students Cheng Huang performed most of the computational work, and Rohan Gejji performed most of the experimental work. They were assisted by Guoping Xia, Changjin Yoon, Chris Fugger, Carson Slabaugh, Andrew Pratt, Pratikash Panda, and Varun Lakshmanan. The fuel nozzle used in the study was provided by Dr. Phil Lee of Woodward, and significant experimental guidance was provided by Dr. Clarence Chang. Special acknowledgements go to Professor Charles Merkle who set the original direction of the study and Dr. Venkatesh Sankaran of AFRL who provided critical advice on the modeling effort.

# Contents

ABSTRACT .....	5
1. INTRODUCTION AND SUMMARY .....	6
2. EXPERIMENTAL DESIGN AND PARAMETRIC STUDY .....	10
2.1. EXPERIMENTAL ARRANGEMENT .....	11
2.2. RESULTS .....	14
2.2.1. Effect of geometry on the combustion dynamics: .....	16
2.2.2. Effect of Operating Conditions on Combustion Dynamics:.....	19
2.2.3. Modulation of the pressure signal:.....	23
2.2.4. Switching of dominant modes:.....	24
2.2.5. Effect of fuel used on the combustion dynamics:.....	25
2.3. SUMMARY AND CONCLUSIONS.....	26
2.4. SPRAY MEASUREMENTS: .....	28
2.4.1. Results.....	30
3. OH PLANAR LASER INDUCED FLUORESCENCE MEASUREMENTS:.....	34
3.1. OPTICAL CHAMBER:.....	34
3.2. PLANAR LASER-INDUCED FLUORESCENCE:.....	35
3.3. OPERATING CONDITIONS: .....	36
3.4. RESULTS: .....	37
3.4.1. PLIF 22: High Equivalence Ratio Test-Case ( $\phi$ : 0.60) .....	37
3.4.2. PLIF 19: Low Equivalence Ratio Test-Case ( $\phi$ : 0.44).....	46
4. COMPUTATIONAL STUDY: .....	51
4.1. INLET STUDY.....	51
4.2. COMPUTATIONAL APPROACH .....	53
4.2.1. Computational Framework.....	53
4.2.2. Turbulence Model .....	54
4.2.3. Combustion Model.....	54
4.2.4. Fuel Spray Model.....	55
4.2.5. Computational Geometry and Operating Conditions .....	59
4.3. PRESSURE COMPARISON BETWEEN EXPERIMENT AND SIMULATION .....	59
4.4. EFFECT OF FUEL SPRAY MODELING IN COMBUSTION INSTABILITY PREDICTIONS.....	61

4.4.1. Effects of Secondary Breakup Model .....	62
4.4.2. Effects of Fuel Spray Distribution .....	66
4.5. EFFECTS OF CHEMICAL KINETICS .....	70
4.6. IDENTIFICATION OF INSTABILITY MECHANISMS.....	71
4.6.1. Open Geometry Simulation .....	72
4.6.2. Closed Geometry Simulation .....	76
5. CONCLUSIONS AND RECOMMENDATIONS .....	88
6. WORK IN PROGRESS .....	92
7. PUBLICATIONS .....	93
Conference Papers .....	93
Student Theses .....	93
REFERENCES .....	94

## ABSTRACT

Concurrent simulation and experiment was undertaken to assess the ability of a hybrid RANS-LES model to predict combustion dynamics in a single-element lean direct-inject (LDI) combustor showing self-excited instabilities. High frequency pressure modes produced by Fourier and modal decomposition analysis were compared quantitatively, and trends with equivalence ratio and inlet temperature were compared qualitatively. High frequency OH PLIF and PIV measurements were also taken. Submodels for chemical kinetics and primary and secondary atomization were also tested against the measured behavior. For a point-wise comparison, the amplitudes matched within a factor of two. The dependence on equivalence ratio was matched. Preliminary results from simulation using an 18-reaction kinetics model indicated instability amplitudes closer to measurement. Analysis of the simulations suggested a band of modes around 1400 Hz were due to a vortex bubble breakdown and a band of modes around 6 kHz were due to a precessing vortex core hydrodynamic instability. The primary needs are directly coupled and validated *ab initio* models of the atomizer free surface flow and the primary atomization processes, and more detailed study of the coupling between the 3D swirling flow and the local thermoacoustics in the diverging venturi section.

## 1. INTRODUCTION AND SUMMARY

The goal of this project was to assess the capability of high-fidelity simulation to predict combustion dynamics in low-emissions gas turbine combustors. To meet that goal, a model configuration of a lean-direct-inject (LDI) combustor was designed and then tested by simulation and experiment. The study combustor comprised a variable length air plenum and combustion chamber, air swirler, and fuel nozzle located inside a subsonic venturi. Test pressure was 1 MPa and variables included geometry and acoustic resonance, inlet air temperature, equivalence ratio, and fuel type. To ensure the same physics were represented in the experiment and the simulation, strict requirements were placed on self-excitation, boundary conditions, and measurement accuracy.

The parallel paths of simulation and experiment were closely coupled. The primary objective of the experimental component was to develop two sets of self-excited dynamics data. The first data set was a survey of combustion dynamics behavior that came from a well-instrumented metal chamber. High-frequency pressure measurements yielded frequencies and mode shapes as a function of inlet air temperature, equivalence ratio, fuel nozzle placement, and combustor acoustic resonances. The second set of dynamics data was based on high-response-rate laser-based combustion diagnostics using an optically accessible combustor section. High-frequency measurements of OH\*-chemiluminescence and OH-PLIF and velocity fields using PIV were also obtained at a relatively stable low equivalence ratio case and a less stable case at higher  $\phi$ .

The primary computational objective was to systematically test the ability of an in-house hybrid RANS-LES model to predict combustion dynamics behavior. Quantitative and qualitative comparisons were made for five different combinations of geometry and operating condition that yielded discriminating stability behavior in the experiment. Comparisons were made on the basis of trends and pressure mode data. Submodels for chemical kinetics and primary and secondary atomization were also tested against the measured behavior. The concurrent simulation exercise also provided significant benefits to the experiment, most importantly its use in interpreting experimental data and defining key variables and measurements.

Overall, the ability of the simulation to match experimental data and trends was encouraging. More specifically the dependence on equivalence ratio was matched. At the low equivalence ratio baseline condition, the predicted instability amplitude was 14.5 kPa compared to the measured value of 20 kPa. Another important area of general agreement was that both experiment and simulation typically presented a bimodal distribution of acoustic modes usually centered around 1400 and 6000 Hz. Although the exact modal energy distribution was not matched, the dominance of a few modes or bands was seen in both experiment and simulation for high-amplitude instabilities. The flatter distribution of energy over more modes at low amplitude instabilities was also seen in both experiment and simulation.

One trend that could not be matched was the effect of a change in the fuel nozzle placement. Whereas measurements indicated greater stability when the fuel nozzle was located upstream of the throat of the subsonic venturi, the simulations predicted more stable behavior when the nozzle was located at the throat. Since the conditions in the throat are very dynamic (high values of  $u'$ ) and can have a strong effect on the Weber-number adaptive submodels that are used for secondary atomization, a more detailed study on the effect of atomization model was conducted. The results showed that a fixed input drop size could provide improved results in terms of matching measured instability amplitude, whereas predictions using the We-number adaptive models gave better results with respect to the energy distribution of the dominant acoustic modes. These and other results strongly indicate the importance and necessity of reliable and validated *a priori* models of atomization.

The rest of this report provides details on the experiments, simulations, and methods for comparison that were developed during the project. Pressure measurements are used as the basis for assessing the simulation capability. Additionally, status is provided on the high-frequency optical measurements (OH PLIF and PIV) and their analysis that were planned to be part of the comparison, but which are not complete at this time.

The experiment and its results are described in detail in Section 1. The design of a model LDI combustor capable of producing self-excited combustion instabilities and the results from a parametric investigation of its combustion dynamics behavior as a function of combustor geometry, inlet air temperature and global equivalence ratio are presented. The parametric survey was a significant effort, with over 100 tests on eight configurations. A second synthetic fuel type was also tested.

The survey measurements showed a very strong dependence of instability amplitude on the geometric configuration of the combustor, i.e., its acoustic resonance characteristics. Measured pressure fluctuation amplitudes ranged from 5 kPa (0.5% of mean pressure) for a 3/8-wave air plenum, ½-wave combustion chamber configuration to 200 kPa (~20% of mean pressure) for a ¼-wave air plenum, ¼-wave combustor configuration. Except for the most stable cases at low equivalence ratio, the dominant unstable mode was consistently around 1400 Hz regardless of geometry.

The stability behavior also showed a consistent and pronounced dependence on equivalence ratio and inlet air temperature. Instability amplitude increased with higher equivalence ratio and with lower inlet air temperature. A band of high frequency modes around 6 kHz were also observed for most configurations and operating conditions. At certain conditions the acoustic power amplitudes of these higher frequency modes were comparable to the longitudinal modes around 1400 Hz.

Initial project goals included assessment of the simulation at pressure oscillation levels of about 1% of mean pressure, and at a frequency of about 400 Hz. The 3/8-wave air plenum, ½-wave configuration met the criteria at equivalence ratios near blowout. At the most stable conditions, acoustic energy is distributed across several (1L-5L) low amplitude modes in the combustor. Usually the 1L mode is of low amplitude at higher equivalence ratios but increases in amplitude when the equivalence ratio is below 0.45. The increase in the 1L mode amplitude coincides with a reduction in amplitude of modes around 1400 Hz and 6000 Hz. A strong modulation in the dynamic pressure is present, with oscillations ranging from 0.5% to 2% of mean pressure. The significant difference in the energy spectrum between the high equivalence ratios cases, where a dominant 4L mode is observed, versus the low equivalence ratio case with energy distributed across modes provides a strongly discriminating case with which to test the simulation.

A pronounced effect of fuel nozzle location on the combustion dynamics was also observed. For the base configuration, the combustion instabilities with fuel nozzle at the throat of the venturi throat were stronger than in the configuration with fuel nozzle 2.6 mm upstream of the nozzle. At higher equivalence ratios, the 4L mode was dominant for both configurations with amplitudes between 40 and 82 kPa. As mentioned above, at lower equivalence ratios the energy was spread across the first five modes in the combustor, with the 1L mode dominant when fuel nozzle was upstream while the 5L mode was consistently dominant when the fuel nozzle was at the throat.

Spray measurements are also described in Section 1. A phase Doppler particle analyzer (PDPA) was used to measure the drop size distribution and droplet velocities for an unconfined spray at atmospheric pressure. The measurements were performed with and without a co-flow of air around the fuel nozzle. Drop sizes of 15-70  $\mu\text{m}$ , axial droplet velocities up to 15 m/s and a spray cone angle of 68-70° were measured. Simulations at the conditions of the spray experiment were performed in which the measured spray cone angle and drop sizes were input to the model.

Use of atmospheric pressure drop size measurements as input to the simulation did not provide the results that matched the high pressure, reacting flow measurements. Accurate measurements for the multi-distillate fuel sprays high pressure, reacting flow conditions are critically needed validation data.

Optical measurements are described in Section 2. OH-PLIF measurements at 10 kHz were performed at the central cross-section of the combustor for equivalence ratios ranging from 0.44 to 0.6 at an inlet air temperature of 800 K. A gradient-based edge detection routine was used to extract the flame-front location from the OH-PLIF images. Planar flame surface density calculated using the extracted flame-front shows a compact flame ( $L_f \sim 25$  mm) at  $\phi=0.6$  and a more diffuse flame ( $L_f \sim 35$  mm) at  $\phi=0.44$ . DMD analysis of the flame front shows a strong flame response at the 4L and 8L acoustic mode frequencies for  $\phi=0.6$  and at the 3L frequency for  $\phi=0.44$ , while a response at the other acoustic mode frequencies is not captured. PIV measurements were performed at 5 kHz for non-reacting flow but glare from the cylindrical quartz chamber limited the field of view to a small region in the combustor. Data analysis of the OH-PLIF and PIV measurements and comparisons with the simulation results are still in work.

The computational framework used for the assessment was the General Equation and Mesh Solver (GEMS), described in Section 3. GEMS is a fully unstructured, density-based finite volume solver with a second-order numerical scheme and an implicit, dual-time procedure for time-accuracy. It solves Navier-Stokes equations in a hybrid RANS/LES mode along with the continuity, energy and species equations. More than 15 two-dimensional cases were run for a parametric assessment of the code's predictive capability. A total of 25 3D cases were run for experimental configurations (two fuel nozzle locations and three equivalence ratios). Another five 3D cases were run with an unconfined geometry to study the hydrodynamic effects. Two cases at  $\phi=0.36$  and 0.60 are still running with an 18-reaction-set kinetics model and will provide results for comparison with simulations using two-step global reactions.

Overall, the simulations can predict reasonable pressure amplitudes and capture the dominant acoustic frequencies measured in the experiments for both high and low equivalence ratios when the fuel nozzle is upstream of the throat, but it does not capture the high frequency modes between 6 and 8kHz. Larger disagreement between experiment and simulation is observed when fuel nozzle at the throat. It is speculated that at least some of this disagreement may be due to the Weber-number-adaptive models that may be overly sensitive to the strong dynamics in the throat region.

Replacing the primary breakup model with a specified spray drop distribution and applying moderate adjustment in the distribution had a significant effect on the prediction. Hence, for a limited range of application, a simple and efficient model could potentially give good results. The predictions can be very sensitive to the stipulated distribution and its adjustment needs to be performed carefully to reach good agreement with the measurement. It is important to understand the limits of the model's applicability. Any model should be tested against the most relevant experimental data available.

Preliminary results from the simulation using an 18-reaction kinetics model indicate that the predicted pressure oscillation amplitude is closer to measurement but still a bit under-predicted. Similar to the experiment, the 4L acoustic mode is dominant at higher equivalence ratio. The simulation predicts similar strength of the 5L mode, which is not observed in the simulation using two-step chemistry or the experiment. A higher number of predicted modes may be a consequence of the finer gradients calculated with the detailed reaction set.

Finally in Section 3, simulation results are used to study potential instability mechanisms. Dynamic mode decomposition (DMD) analysis of simulations of an “open-domain” combustor with

presumably weak acoustic influences indicated the presence of a vortex breakdown bubble (VBB) mode, with a distinct response in the range around 1400 Hz, near the same frequency where the highest pressure oscillations were measured in the combustor. The VBB has strong spatial and temporal character and represents the contour of a surface representing local flow stagnation, with high potential for strong modal (temporal and spatial) interactions with the combustor thermoacoustics.

The DMD analysis also showed that the pressure oscillations measured around 6-8 kHz were due to strong and dynamic swirling behavior in the diverging section of the venturi, i.e., a Precessing Vortex Core (PVC) instability. Guided by other investigations of premixed gaseous fuel swirl combustors, nonlinear coupling between the dominant acoustic modes (5L/6L) and the PVC hydrodynamic mode was speculated to be the source of the generally weak pressure oscillations around 4.6 kHz, whose relative strength was highest for the case of the fuel nozzle located at the throat and high  $\phi$ .

Investigation of the coupling mechanisms continued with using DMD to calculate heat release and pressure modes predicted by the simulation. These were then used to calculate the Rayleigh index spectrum, which was used to identify sources and sinks according to the Rayleigh criterion at 5L/6L and PVC frequencies. Axial slices of the Rayleigh index showed complex and highly three-dimensional reacting flow in the diverging section of the venturi.

The report concludes with recommendations for future study. The detailed analysis of the simulation results provide sharper focus for validation measurements. Specifically, the use of the detailed chemistry set allows prediction of OH concentrations which can be more directly compared to the OH PLIF and OH\* chemiluminescence measurements. For more precise validation, fiber-optic emission measurements can be made in strategic locations identified from the simulations.

The results from the spray modeling study point to the need for more directly coupled *ab initio* models of the atomizer free surface flow and the primary atomization processes, thereby avoiding *ad hoc* assumptions of droplet distributions that are likely to be problem-dependent. In the near-term, and for limited ranges of operation, the use of two-constant empirical models (like We-dependent mean drop size and a stipulated shape of distribution) should be explored. Time- and space-resolved measurements of drop size distributions in a dynamic, high-pressure, reacting flow are needed to test all the models.

In parallel with developing the atomization capability, testing with a gaseous fuel for which a good reaction set exists will eliminate the variables associated with atomization, vaporization, and drop transport and will allow validation of a case with simpler physics. Experiments should use test hardware designed for adiabatic operation so that the conditions in the simulations are better matched. Although it was not part of this study, the use of turbulent combustion models, such as Dynamic Thickened Flame models or flamelet models should be considered in future studies.

Complex nonlinear coupling processes between heat release, acoustics, and hydrodynamics have been shown to exist in premixed-gas, sudden-expansion combustors with swirl. The swirling, expanding flows in the diverging venturi section with complicated acoustic reflections may be introducing physics that are not easy to detect or understand. More specific study of the complex interactions between the expanding, swirling flow and the thermoacoustics in a diverging cross section is needed, first with a gaseous fuel. A systematic variation in geometry and swirl number that includes the sudden expansion used in most configurations may lead to a better understanding of these effects in the LDI configuration.

## 2. EXPERIMENTAL DESIGN AND PARAMETRIC STUDY

The management of combustion dynamics in gas turbine combustors has become more challenging over the past three decades as strict NOx/CO emission standards have led to engine operation in a narrow, lean regime [1, 2]. While premixed or partially premixed flame configuration concepts such as Lean Premixed Pre-vaporized (LPP), Rich Quench Lean burn (RQL), and Lean Direct Injection (LDI) have been largely successful in reducing NOx emissions, they have also shown likelihood for positive coupling between acoustic, flow and combustion processes that can lead to combustion instabilities [2]. Focus of the work on combustion instabilities for these concepts has been typically limited to frequencies corresponding to longitudinal and/or circumferential modes that are present at a few hundred hertz [3].

The present work is based on a single element LDI configuration where liquid fuel is injected into a highly inertial air flow accelerated by a converging-diverging subsonic venturi [4, 5]. The success of the LDI design depends on rapid fuel-air vaporization and mixing and swirl stabilized combustion. Several studies conducted over the past two decades have been focused on the characterization of the flow-field in the combustor and the NOx emissions. A few studies at lower chamber pressure (~0.3 MPa) have investigated combustion instabilities. Santavicca et al [6-8] studied a Jet-A fueled combustor and found pressure fluctuations amplitudes as high as 8% of the mean chamber pressure and measured the temporal and spatial CH\*-chemiluminescence downstream of the combustor dump-plane. Dependencies of equivalence ratio, incoming air flow rate and air temperature were reported. It is interesting to note that the observations were similar to those made in premixed, low-pressure gas systems [9, 10].

Swirl stabilized combustion is presently common in gas turbine combustors. Combustion dynamics in swirl stabilized flames have been attributed to swirl-acoustic interactions [11]. Candel et al [9, 10, 12-14] reported a non-linear interaction between the hydrodynamic precessing vortex core (PVC) mode and the thermo-acoustic modes in the combustor in premixed methane-air flames. Similar observations were reported in atmospheric pressure flames studied by Stohr et al. [15-17]. A recent review paper by Candel et al [12] presented a large body of work on the topic of instabilities in swirl-stabilized flames. However, as pointed out in the paper, majority of this work is based on atmospheric pressure premixed gaseous flames. Introduction of a poly-disperse liquid spray results in stratification of fuel and air transported to the flame, leading to change in the flame structure caused by the inhomogeneity in mixture fraction. The uneven response of fuel and air to incident acoustic waves can also alter the swirling flame characteristics. While some studies at atmospheric and moderate pressures have been reported [18, 19] with non-premixed and partially premixed flames in liquid fueled combustors, work on high pressure unstable spray flames is necessary for investigation of these mechanisms at operating conditions relevant to aviation gas turbines. Computational studies performed on the same geometry and operating conditions used in this study have been performed at Purdue [20, 21] and show the significance of the swirl acoustic interactions, especially the formation of a vortex breakdown bubble (VBB) that plays a significant part in the flame

holding and stabilization processes that consequently dictate the combustion response to the combustor acoustics.

The present work aims to build on the body of available work on LDI and other swirl stabilized combustors and extend it to a liquid fueled, single element gas turbine combustor operating at a high chamber pressure (1 MPa) and capable of generating self-excited combustion instabilities. The objective of the current paper is to explore the effect of various parameters such as combustor geometry, inlet air temperature, global equivalence ratio, fuel nozzle location and the fuel composition on combustion instabilities using high frequency pressure measurements located at multiple locations in the combustor. The experimental study is part of a larger study to assess the capability of high-fidelity computations to predict combustion dynamics.

The design of the experimental arrangement and instrumentation is described in the first section of the paper. Results from detailed high frequency pressure measurements in the combustor describing the effect of combustor geometry, inlet air temperature, global equivalence ratio, fuel nozzle location and the fuel used are described thereafter. Conclusions based on the parametric study are presented at the end of the paper. The pressure measurements show that the instabilities increase with equivalence ratio and are higher at lower inlet air temperatures. The dominant unstable mode consistently lies in the 1200-1600 Hz frequency range irrespective of the geometric configuration of the combustor. The pressure fluctuation amplitude varies significantly with configuration from 0.5-2% P'/Pc at a detuned combustor configuration to as high a 20% P'/Pc at short combustor configuration. A pronounced effect of fuel nozzle location on the combustion dynamics is observed, with the instabilities higher when the fuel-nozzle is at the throat of the converging-diverging venturi section of the LDI element and lower when it is upstream. High frequency modes in the 5-7 kHz range are observed for most combustor configurations and operating conditions. The pressure fluctuation amplitudes at these frequencies are often comparable to the dominant longitudinal modes in the combustor. The parametric study shows discriminating behavior in terms of dominant modes and amplitudes with changes in geometric and operational parameters. This provides a valuable data-set for validation of computational models.

## 2.1. EXPERIMENTAL ARRANGEMENT

The single element LDI combustor design is based on axial mode combustion dynamics with a fundamental frequency between 300-400 Hz. Combustion instability amplitudes less than 0.5-3% of the mean chamber pressure are desired so that the instabilities are a fraction of the pressure drop across the subsonic venturi of the LDI element and representative of instabilities that may be observed in gas turbine combustors. The major dimensions of the combustor are determined at operating conditions tabulated in Table 1 below based on a 1-D linearized Euler equation (LEE) solver [22-24]. The combustor operates at a mean chamber pressure of 1 MPa. The combustor uses kerosene fuel (Jet-A/ FT-SPK) and heated air up to a temperature of 800 K.

Table 1: Summary of design envelope and nominal operation parameters

Fuel	Jet-A and FT-SPK
Inlet Air Temperature	650 – 800 K
Equivalence Ratio	0.37 - 0.7
Inlet Boundary Condition	Constant mass inflow from a choked orifice
Exit Boundary Condition	Choked nozzle
Diameter of combustor	50.8 mm
Diameter of air plenum	25.4 mm

A schematic of the LDI combustor is shown in Figure 1. The combustor is divided into an air inlet section, air plenum, swirler-venturi-injector assembly, combustion chamber, and exit nozzle. A converging-diverging subsonic venturi with an included angle of 90° at the inlet and outlet is located at the downstream end of the air plenum. The combustion chamber is 50.8 mm in diameter and its length can be varied in discrete increments from 0.28 m to 1.08 m similar to the air plenum. To approach an adiabatic wall boundary condition, thermal barrier coating (MCraly bond coat and Yttria stabilized Zirconia coating) is applied to the first 100 mm of the combustion chamber and the diverging section of the venturi where the maximum heat release occurs in the combustor. This allows better comparison with computational results where adiabatic wall boundary conditions are commonly used for the combustor walls. A choked nozzle at the end of the combustion chamber controls the chamber pressure at ~1 MPa.

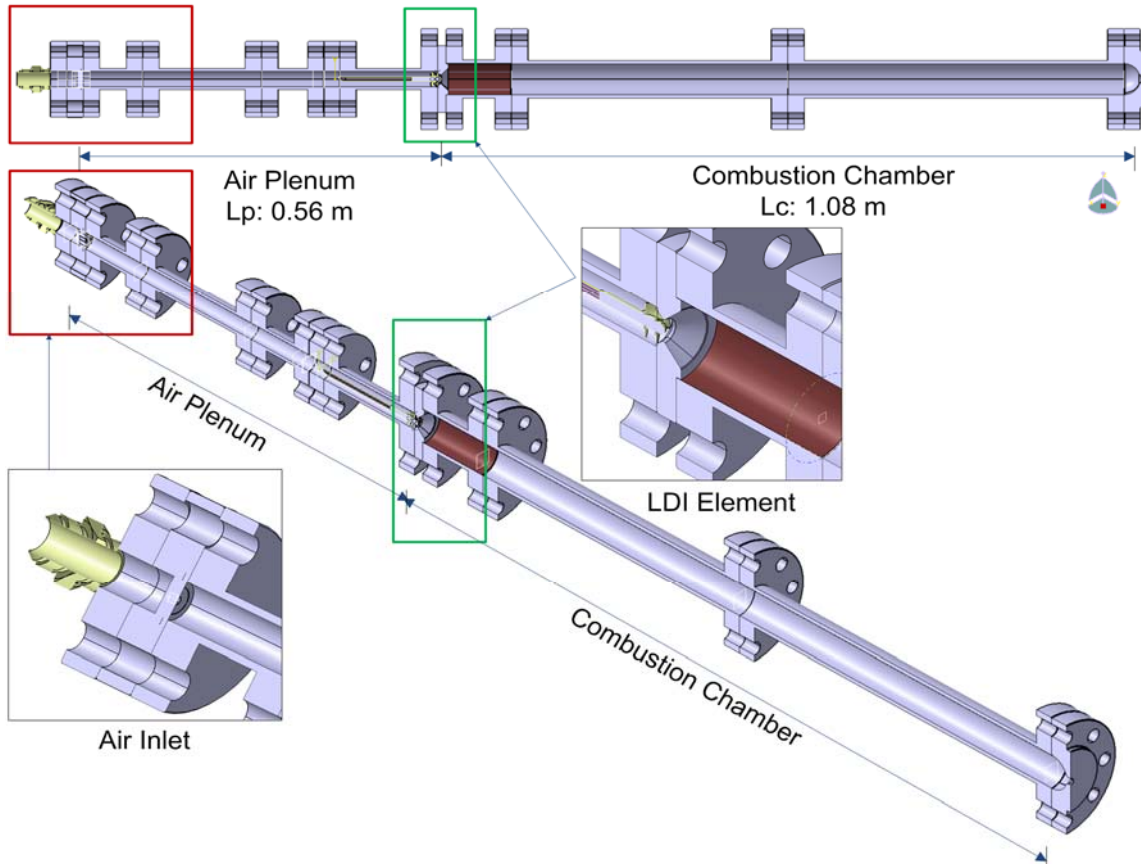
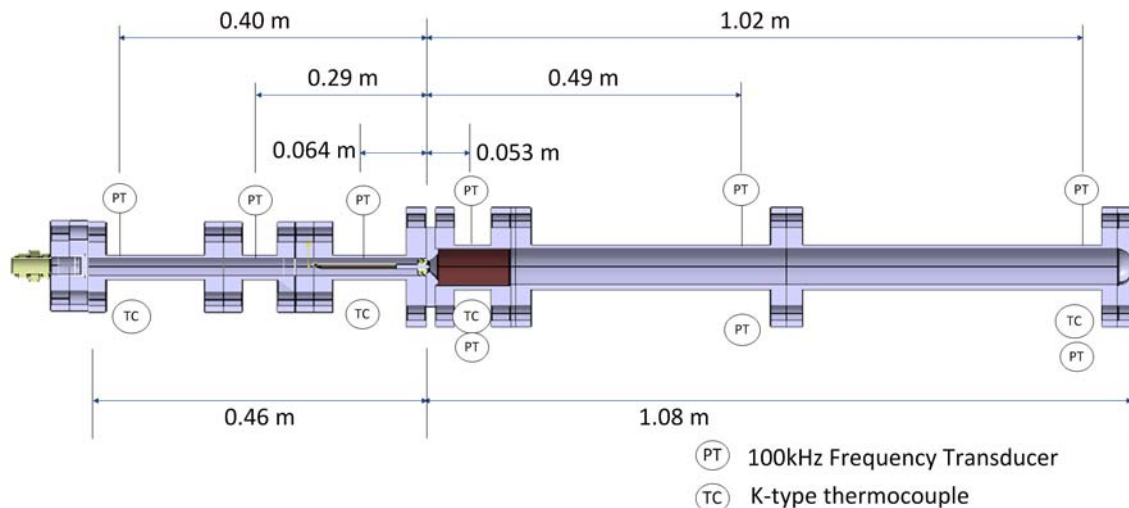


Figure 1: Schematic of the LDI combustor

Air, heated using an 80 kW electrical heater, enters the combustor through a slotted choked orifice plate, designed to minimize shock-induced unsteadiness [25]. The air mass flow rate is calculated across a sonic venturi with a known co-efficient of discharge. The pressure and temperature upstream of the orifice plate is monitored to maintain a constant air flow rate during the test. The length of the air plenum can be changed in discrete increments from 0.19 m to 0.56 m. A helical vane axial flow swirler with six vanes each with a tip angle of 60° is located at the end of the air plenum. A hollow cone pressure swirl atomizer with a flow number of 1.32 is used to supply fuel to the combustor and is located at the end of the air plenum. A Coriolis flow meter (Micro Motion Coriolis ELITE, 0.1% accuracy) is used to measure the mass flow-rate of fuel used in the experiment. The fuel is sparged using nitrogen prior to testing to remove any dissolved air content from the fuel. The oxygen content in the fuel is monitored and ensured to be below 1% (by volume) during tests to avoid coking of fuel in the feed lines in the combustor.

The combustor is instrumented at multiple locations with piezoresistive pressure transducers (Kulite WCT-312M-10/35/70 BARA). The transducers are mounted recessed from the combustor inner wall to avoid high thermal loading on the sensor element. The recess cavity is designed as a Helmholtz resonator with a resonant frequency that is much higher (~14 kHz) than frequencies of interest in the experiment. The transducers are located at six axial locations, three in the air plenum and three in the combustion chamber. Two transducers are located at each axial location in the combustion chamber diametrically opposite to each other for identification of modes that are not purely longitudinal in nature. Data is collected from these transducers at 100 KHz. Figure 2 depicts the pressure instrumentation in the combustor for the  $\frac{3}{8}$  wave air plenum and  $\frac{1}{2}$  wave combustion chamber configuration of the combustor. Temperature measurements are obtained using k-type thermocouples (Omega GKMQSS-062G) mounted flush with the inner diameter of the combustor at the same axial locations as the pressure measurements. Feed system and combustor pressures are obtained at a lower sampling rate (100 Hz– 2 kHz) using GE Sensing (UNIK 50E6 series; 0.04% accuracy) pressure transducers to control and monitor combustor operating conditions.



A summary of the parametric changes in the combustor in terms of its geometry and operating conditions is tabulated in Table 2 and illustrated in Fig. 3. The check marks in the second and third column of the table indicate that the particular geometry combination with corresponding air plenum configuration was tested. Cross mark indicates that the geometry was not tested. The resonance for the air plenum and combustion chamber uses as a reference a 1L (first longitudinal) mode with a frequency of 350 Hz.

Table 2: Summary of combustor configurations and operating conditions

Air plenum	Geometric Parameters		Operational parameters	
	Combustion chamber		$\phi$	Tair (K)
	1/4 wave (short combustor)	1/2 wave (long combustor)		
1/4 wave	✓	✓		650
3/8 wave	✗	✓	0.7- 0.37	700
1/2 wave	✓	✓		750
Full wave	✗	✓		800

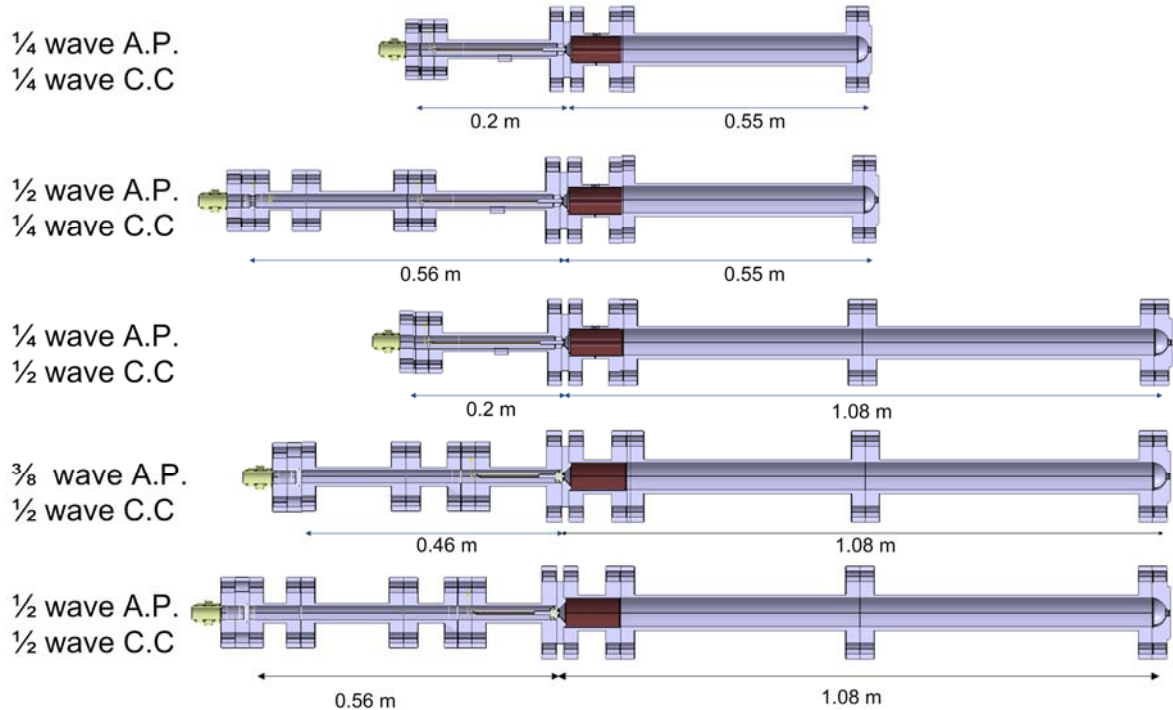


Figure 3: Geometric configurations of the LDI combustor

## 2.2. RESULTS

A typical test performed in the LDI combustor is approximately 30 s long. During the test, the combustor geometry, fuel nozzle location, air mass flow rate and the inlet air temperature are held constant. The flow rate of fuel is varied through the test duration to

attain a range of equivalence ratios. Chamber pressure, and global equivalence ratio measurements obtained during a representative test are shown in Figure 4 below. The air temperature measured near the inner wall in the combustor is shown in Figure 5. The test was performed at an 800 K inlet air temperature with a  $\frac{3}{8}$  wave air plenum and  $\frac{1}{2}$  wave combustion chamber configuration.

Ignition was obtained at the beginning of the test using a spark igniter (Champion AA134S-1) at a high equivalence ratio ( $\phi \sim 0.7$ ) and the fuel flow rate is swept down to lean blow-out of the flame ( $\phi \sim 0.36$ ). The equivalence ratio is held constant for a time period of 3-5 s before the fuel flow rate is reduced to a lower value. At lean blow-out large pressure fluctuations are observed at a very low frequency of 20-30 Hz. The pressure fluctuations immediately after ignition rise with an approximately exponential profile to a near limit-cycle amplitude. The temperature profile follows the equivalence ratio profile closely during the test as expected.

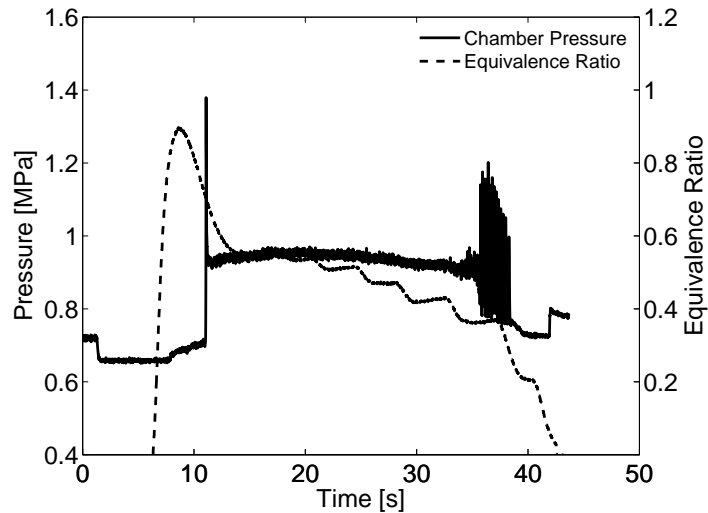


Figure 4: Combustion chamber pressure and global equivalence ratio during a typical LDI test

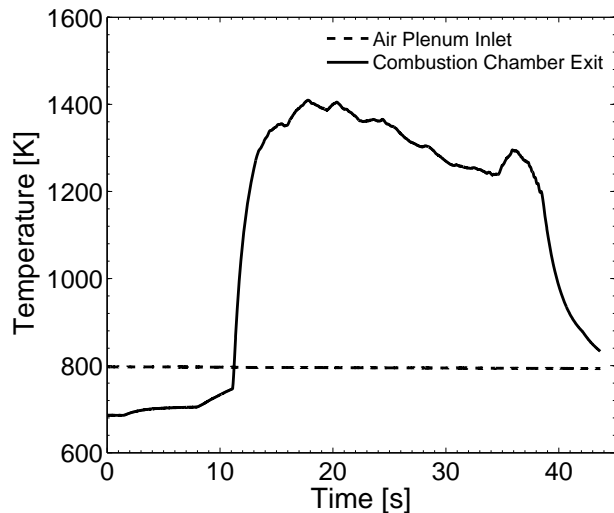


Figure 5: Air plenum and combustion chamber gas phase temperature during the course of a typical LDI test

### **2.2.1. Effect of geometry on the combustion dynamics:**

The primary method to vary the level of instability attained in the combustor was to vary the LDI combustor geometry, namely the lengths of the air plenum and the combustion chamber. Figure 6 shows a compilation of results for all geometrical configurations of the combustor. Each data-point corresponds to pressure fluctuation amplitude obtained from band-passed pressure data at dominant frequencies identified from power spectral density analysis for each test case.

The instability amplitudes have a significant variation with combustor configuration ranging from pressure fluctuation amplitudes of 5-80 kPa (0.5-8% P'/Pc) for the 3/8 wave air plenum- 1/2 wave combustion chamber configuration to as high as 200 kPa (~20%P'/Pc) for the 1/4 wave air plenum-1/4 wave combustion chamber configuration. Irrespective of the combustor configuration, the amplitude of instability levels is consistently high at around 1200-1500 Hz, and suggests that the fluid mechanics that control combustion respond strongly to pressure and velocity oscillations is in this range of frequency. The 3/8 wave air plenum and 1/2 wave combustion chamber was chosen as the baseline geometry for the study as it presents instabilities in the target amplitude ranges at low equivalence ratios.

The trend-wise behavior seen in Figure 3 was investigated via concurrent simulations of the model combustor [26], that indicated the presence of a vortex breakdown bubble (VBB) with a distinct response in the range around 1400 Hz, indicating potential for strong interactions between the swirling flow and combustor thermoacoustics. The harmonics of this frequency are also of high amplitude, peaking at an amplitude of 200 kPa (~20% P'/Pc) at 2.8 kHz for the 1/4 wave A.P. - 1/4 wave C.C. configuration. Another observation is the presence of high amplitude modes in the 6-8 kHz frequency range observed in all configurations at higher equivalence ratios ( $\phi > 0.5$ ). Nonlinear coupling between heat release, acoustics, and hydrodynamics is a possibility that needs to be further explored. A better understanding of the potentially very complex interactions between the expanding, swirling flow and thermoacoustics in the diverging part of the venturi also needs more specific study.

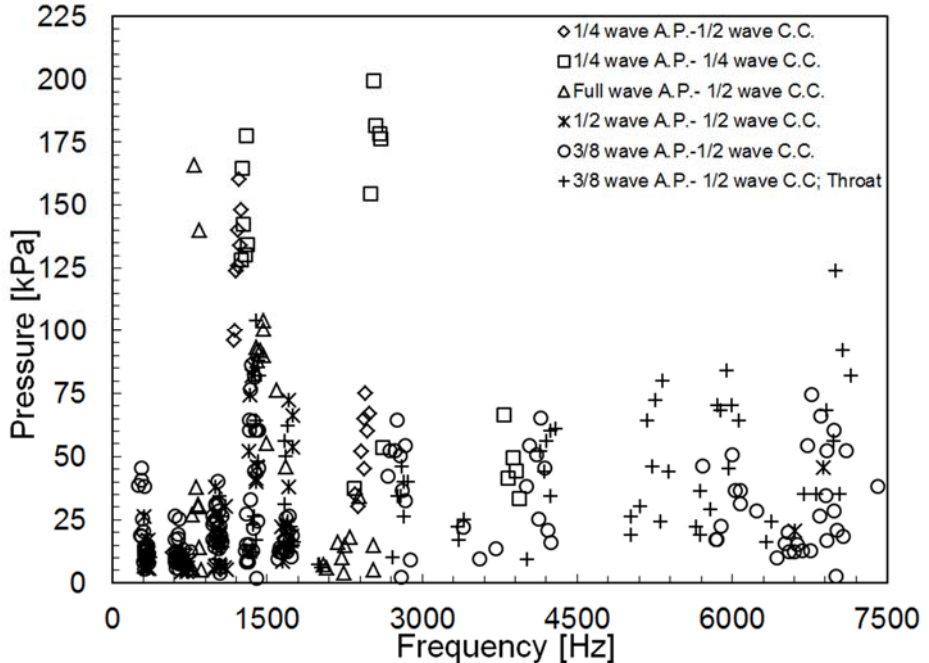


Figure 6: Summary of pressure fluctuation amplitudes as a function of frequency for all test configurations

To illustrate the large variation in behavior with geometry, a comparison in the pressure signals obtained between the highly unstable  $\frac{1}{4}$  wave air plenum-  $\frac{1}{4}$  wave combustion chamber configuration and the moderately unstable  $\frac{3}{8}$  wave air plenum-  $\frac{1}{2}$  wave combustion chamber configuration is shown in Figure 7 below. The comparison is made using high-pass filtered pressure data and the power spectral density diagrams for tests run at a high equivalence ratio of 0.6 and at an air temperature of 800 K. The data are high-pass filtered at 70 Hz using a Butterworth filter of 2<sup>nd</sup> order to remove any electrical noise in the data that may be present at 60 Hz. From the PSD plots, it can be seen that the many modes in the long-chamber configuration (b) are coalesced into fewer, much stronger modes in the shorter chamber. The  $\sim 1400$  Hz mode dominates both spectra; it is the 2L mode for the shorter combustor and the 4L mode for the longer combustor. The oscillation amplitude in the shorter combustor configuration is approximately twice that of the longer combustor configuration.

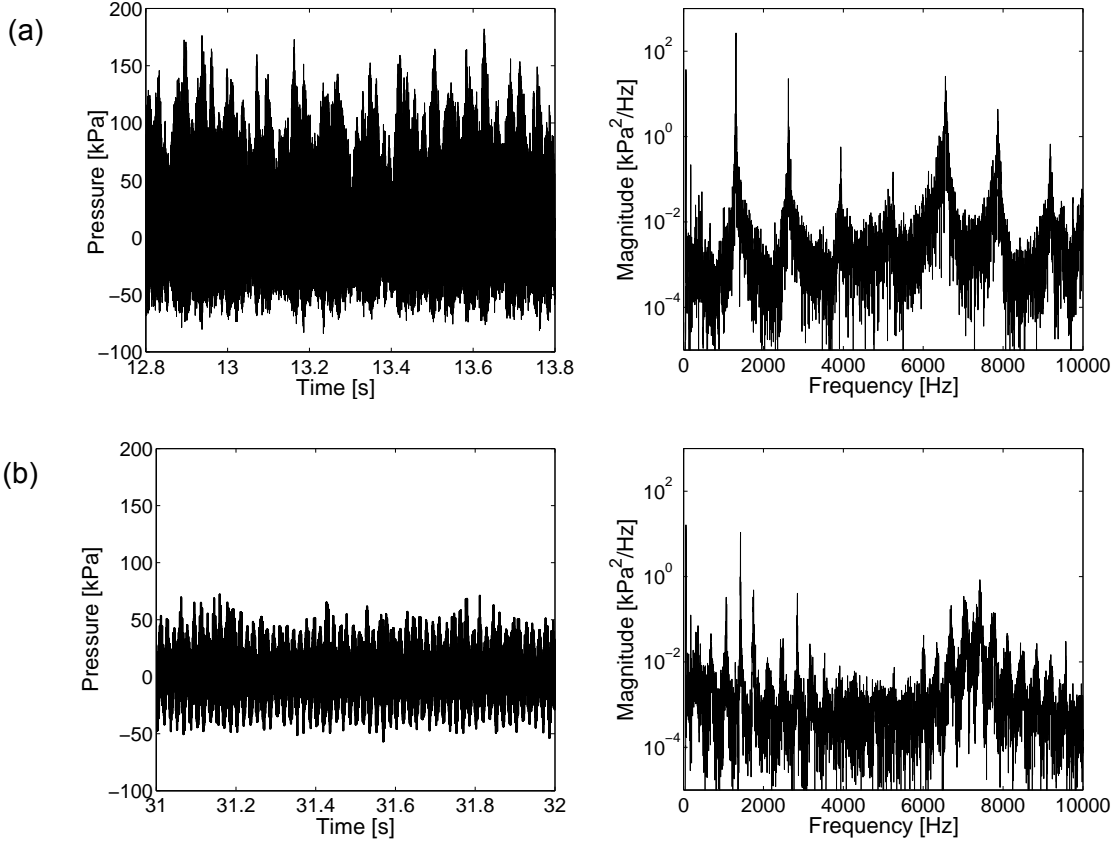


Figure 7: High-pass filtered pressure data and power spectral density for (a) 1/4-wave air plenum, 1/4-wave combustion chamber and (b) 3/8 wave air plenum, 1/2-wave combustion chamber configurations ( $\phi \sim 0.60$ ,  $T_{air}=800$  K). The modes around 1400 Hz (2L in 1/4-wave and 4L in 3/8-wave) are dominant.

Pressure data obtained at different locations in the combustor were used to identify the pressure mode-shapes in the combustor. The measured mode-shapes are compared with those calculated using the linearized Euler equation (LEE) solver and with data obtained from the high fidelity hybrid RANS-LES simulations. The mode shapes calculated based on the experimental data agree fairly well with the simulations. The agreement validates the definition of the longitudinal pressure mode shapes and helps rank the dominant modes. Representative plots of the mode-shape comparison for the 3/8 wave air plenum, 1/2 wave combustion chamber are shown in Figure 8 below. The tests were performed at an inlet air temperature of 800 K and with the fuel injector 2.6 mm upstream of the venturi throat. The pressure data from two transducers located diametrically opposite to each other 0.053 m (2.1") downstream of the venturi throat were used to calculate the phase difference between the pressure signals. For the 1L- 4L modes, the signals were in phase ( $\pm 10^\circ$ ) indicating that these modes are predominantly longitudinal. For the higher frequency modes in the 6-8 kHz range, the pressure signals were not in phase with each other indicating the pressure mode are not purely longitudinal and have contribution from the circumferential or transverse modes of the chamber.

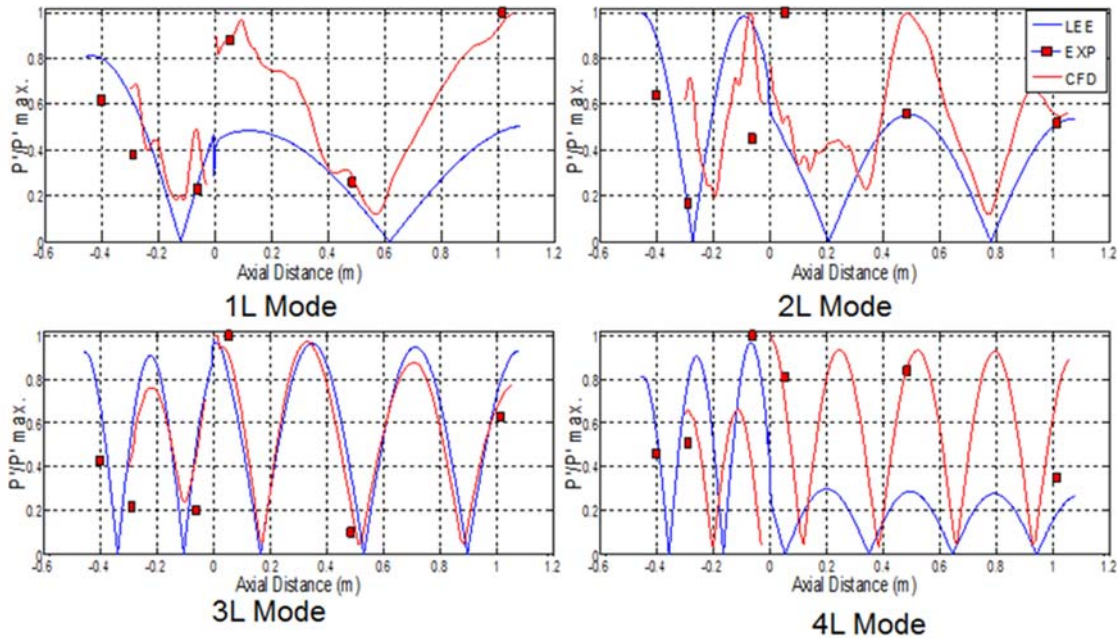


Figure 8: 1L, 4L mode-shape reconstruction using band-passed pressure data at multiple locations in the combustor for the 3/8 wave air plenum- ½ wave combustion-chamber configuration

### 2.2.2. Effect of Operating Conditions on Combustion Dynamics:

#### 2.2.2.1. Effect of inlet air temperature:

The inlet air temperature to the combustor was varied in steps of 50 K from 650 K to 800 K for all the combustor configurations. For the same equivalence ratio, and air and fuel mass flow rates, the overall instability levels are typically lower at higher inlet air temperatures. The maximum instability levels are observed at an air temperature of 700 K. Figure 9 shows pressure fluctuation amplitudes for the 3/8 wave air plenum-1/2 wave combustion chamber as a function of the inlet air temperature for the first five longitudinal modes in the combustors. The raw pressure signal is band-passed using the 2<sup>nd</sup> order Butterworth filter to obtain amplitudes at individual pressure modes. For this configuration, the 4L mode is dominant at  $\phi > 0.45$  and the 1L mode is dominant at  $\phi < 0.45$ . The 4L mode is stronger at lower inlet air temperatures (maximum at 700 K) as shown in Figure 9 below whereas the trend is reversed for the 1L mode where the amplitudes are higher at higher temperatures (maximum at 750 K). The higher frequency modes (not presented in Figure 9 for clarity) show similar trends as the 4L mode with changes in the inlet air temperature. The lower amplitudes at the high air temperatures are promising as these temperatures ( $\geq 800$  K) are more representative of typical T3 temperatures in aviation gas turbine combustors.

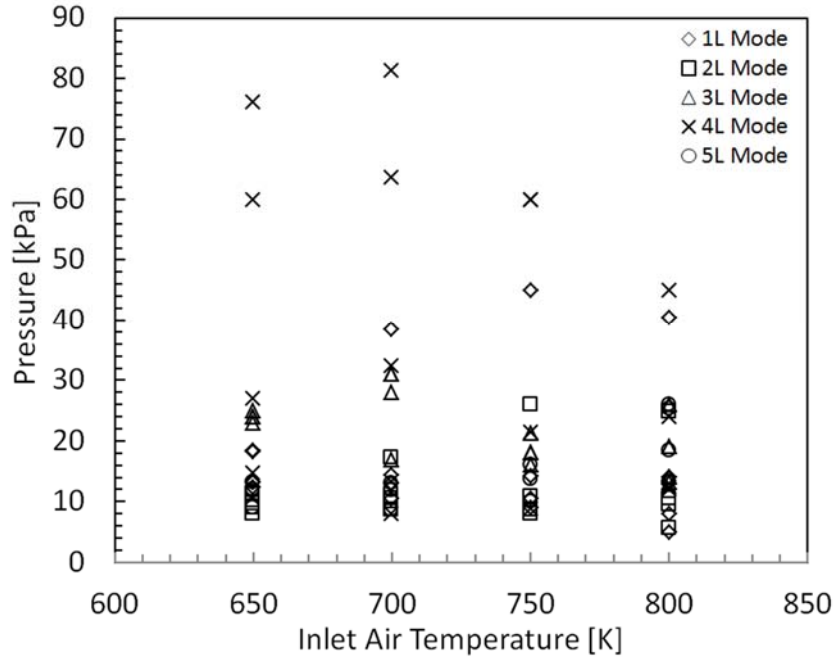


Figure 9: Peak to peak pressure fluctuations in the combustor as a function of inlet air temperature (3/8 wave air plenum- 1/2 wave combustion chamber)

#### 2.2.2.2. *Effect of equivalence ratio:*

Global equivalence ratio (based on fuel and air mass flow rates) in the combustor was varied during every test and data extracted at multiple time instances. Figure 10 shows the influence of equivalence ratio on the combustion instability in the combustor for the 3/8 wave air plenum, ½-wave combustion chamber configuration. The overall instability amplitude increases with the equivalence ratio. The 4L mode is dominant at higher equivalence ratios ( $>0.45$ ) while the 1L mode is stronger at equivalence ratios lower than 0.45. At low equivalence ratios, the energy is distributed in the first five longitudinal modes with the variation in amplitude between each mode being relatively small. At higher equivalence ratios above 0.45, the 4L mode amplitude is significantly higher than the 1L-, 3L, and the 5L modes.

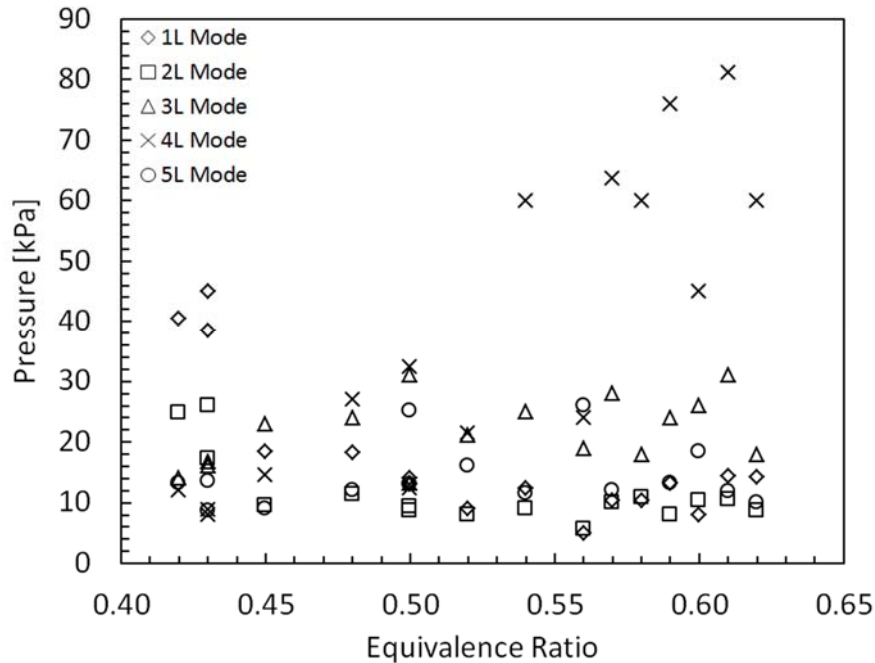


Figure 10: Peak to peak pressure fluctuations in the combustor as a function of global equivalence ratio (3/8 wave air plenum, 1/2 wave combustion chamber)

#### 2.2.2.3. Effect of Fuel Nozzle Location on Combustion Dynamics:

For the 3/8 wave air plenum and 1/2 wave combustion chamber configuration, the effect of the fuel injector location with respect to the throat of the converging-diverging venturi was measured. The configuration with the fuel nozzle at the throat was more unstable than the configuration with fuel nozzle upstream of the throat. Representative test results for the 3/8 wave air plenum- ½ wave combustion chamber configuration at an air temperature of 800 K and two equivalence ratios, 0.6 and 0.42, are used to highlight the important differences in the instabilities.

##### 2.2.2.3.1. Air Inlet Temperature: 800 K, Equivalence Ratio: 0.6

Figure 11 below shows the comparison of high-pass filtered pressure data and power spectral density based on the pressure data for the case (a) with the fuel injector 2.6 mm upstream of the venturi throat and (b) the fuel injector at the throat respectively at an equivalence ratio of 0.6. The 4L mode is the dominant mode for both the fuel nozzle locations. The case with the fuel nozzle at the throat has an amplitude of 82 kPa (peak to peak) at the 4L mode ( $\sim 8\% P'/P_c$ ) while the case with the fuel nozzle upstream has an amplitude of 45 kPa (peak to peak) at the 4L mode ( $\sim 4.5\% P'/P_c$ ). Strong modes with amplitudes as high as the dominant longitudinal mode are observed in the 6-8 kHz range for both cases. The higher frequency modes have larger amplitudes (max.  $P' = 82$  kPa) when the fuel nozzle is at the throat than when the nozzle is upstream (max.  $P' = 50$  kPa). The 1L mode pressure fluctuations are  $\leq 1\%$  of mean chamber pressure.

A small shift of the spray injection location may result in nonlinear changes in the spray and consequently on the flame behavior. Concurrent simulations (discussed in Section 3.3) also show differences in the spray break-up as well as the hydrodynamic modes- VBB and PVC, with small changes in the fuel nozzle locations. These differences can

significantly affect the combustion response and consequently the instability amplitudes and dominant pressure modes.

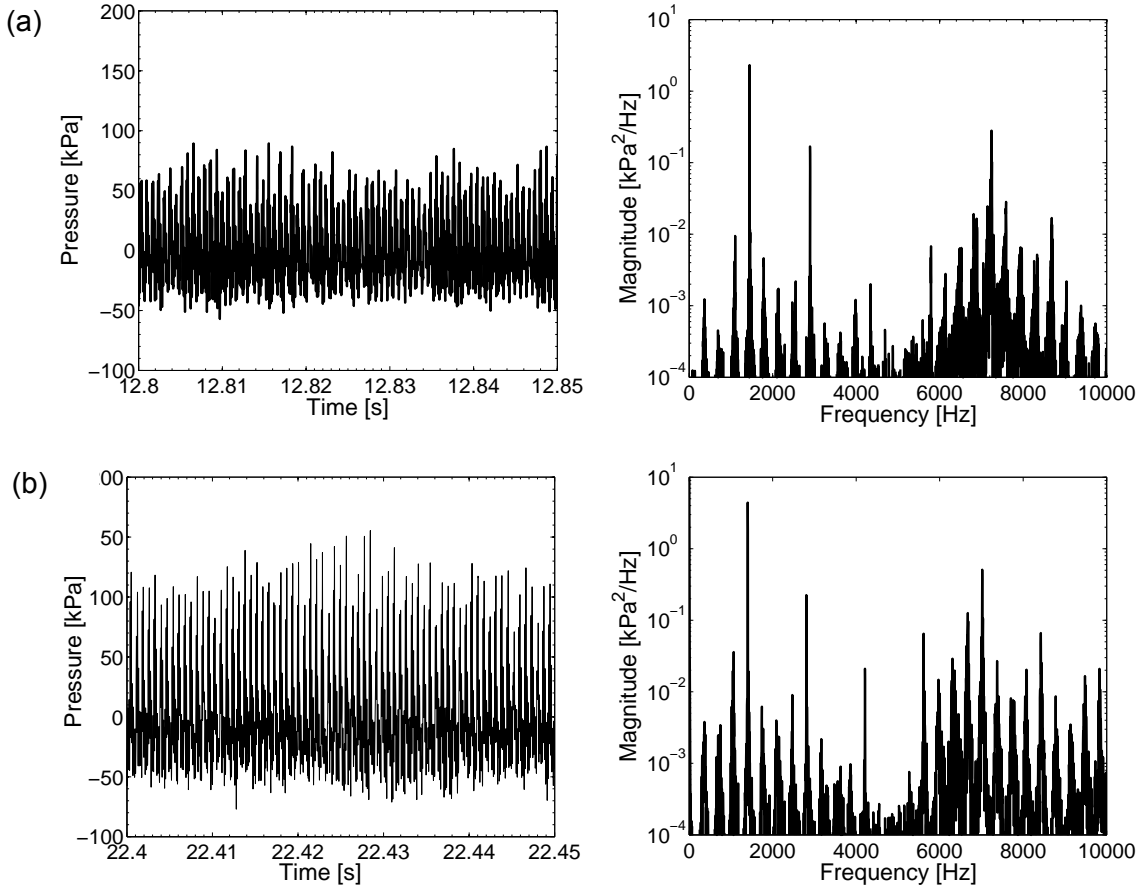


Figure 11: High pass filtered pressure data and power spectral density (PSD) for an equivalence ratio of 0.6 and inlet air temperature of 800 K when the fuel injector is (a) 2.6 mm upstream of the venturi throat and, (b) at the venturi throat.

#### 2.2.2.3.2. Air Inlet Temperature: 800 K, Equivalence Ratio: 0.42

Figure 12 below shows the comparison of high-pass filtered pressure data and power spectral density based on the pressure data for the case (a) with the fuel injector 2.6 mm upstream of the venturi throat and (b) the fuel injector at the throat respectively at an equivalence ratio of 0.42. The pressure data show a dominant 1L mode in the combustor when the fuel injector is upstream of the venturi throat with pressure fluctuation amplitude of 40 kPa at the 1L frequency of 325 Hz. The 5L mode (1675 Hz) is the strongest mode in the combustor with pressure fluctuation amplitude of 56 kPa when the injector is located at the throat of the venturi. Based on overall pressure amplitudes, the configuration with the fuel injector at the throat is more unstable than the configuration with the injector upstream of the throat. The energy spectra for both these cases are spread across the first few modes in the combustor. This is significantly different from the behavior at higher equivalence ratios where a dominant 4L mode is observed. This absence of a strong single dominant mode may indicate presence of multiple subtle physical mechanisms participating in driving/damping the instabilities. This case was further studied with optical measurements.

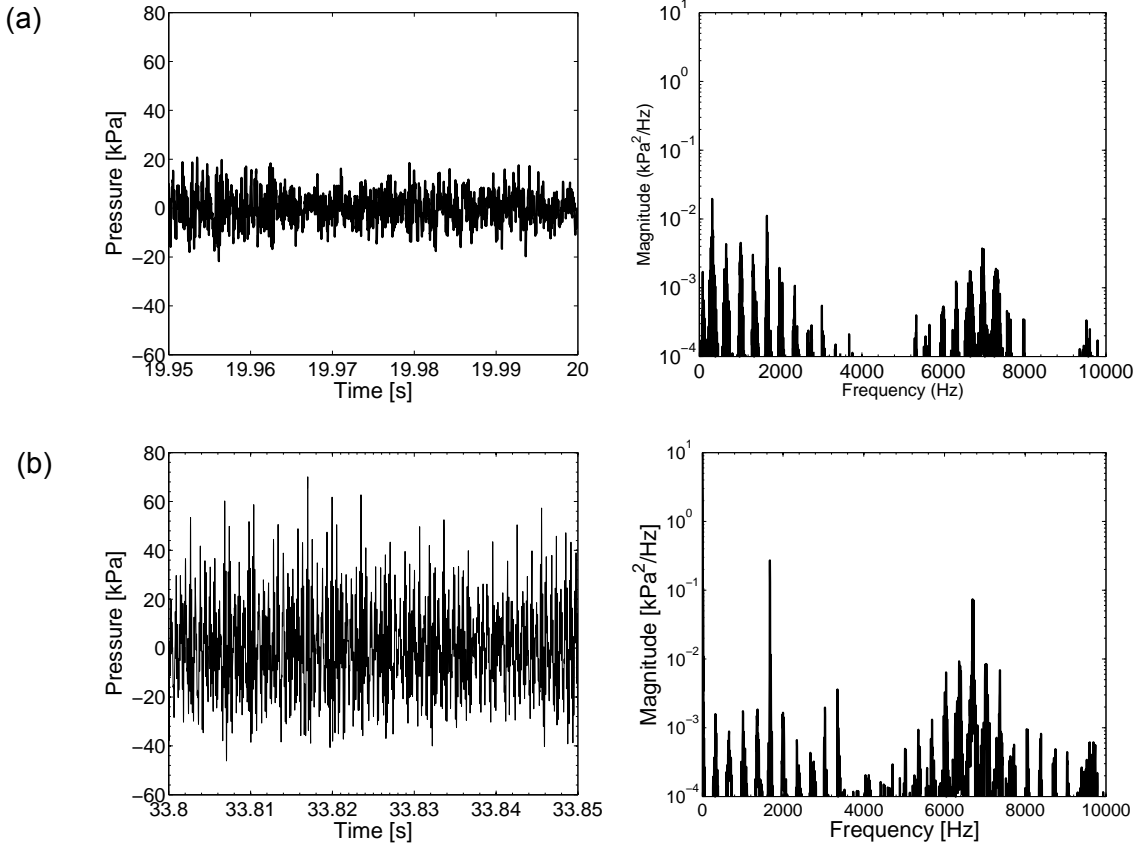


Figure 12: High pass filtered pressure data and power spectral density (PSD) for an equivalence ratio of 0.42 and inlet air temperature of 800 K when the fuel injector is (a) 2.6 mm upstream of the venturi throat and, (b) at the venturi throat.

### 2.2.3. Modulation of the pressure signal:

A strong 4L mode is observed at a frequency of  $\sim$ 1400 Hz in the combustor for equivalence ratios exceeding 0.45 in the combustor. Below this equivalence ratio, the energy is more distributed across the 1L-5L modes with significantly lower overall pressure oscillation amplitudes. At the high amplitudes (4L mode) at high equivalence ratios, the pressure signal shows a limit cycle behavior where it reaches a stationary high amplitude. On the other hand, at lower equivalence ratios and lower pressure oscillation amplitudes, a significant modulation of pressure is observed. When short time slices are selected for analysis within these modulating periods, modes switch between the 1L-5L but remain fairly low in amplitude. This behavior is shown in Figure 13 below using band-passed pressure data for the 3/8 wave air plenum- ½ wave combustion chamber configuration.

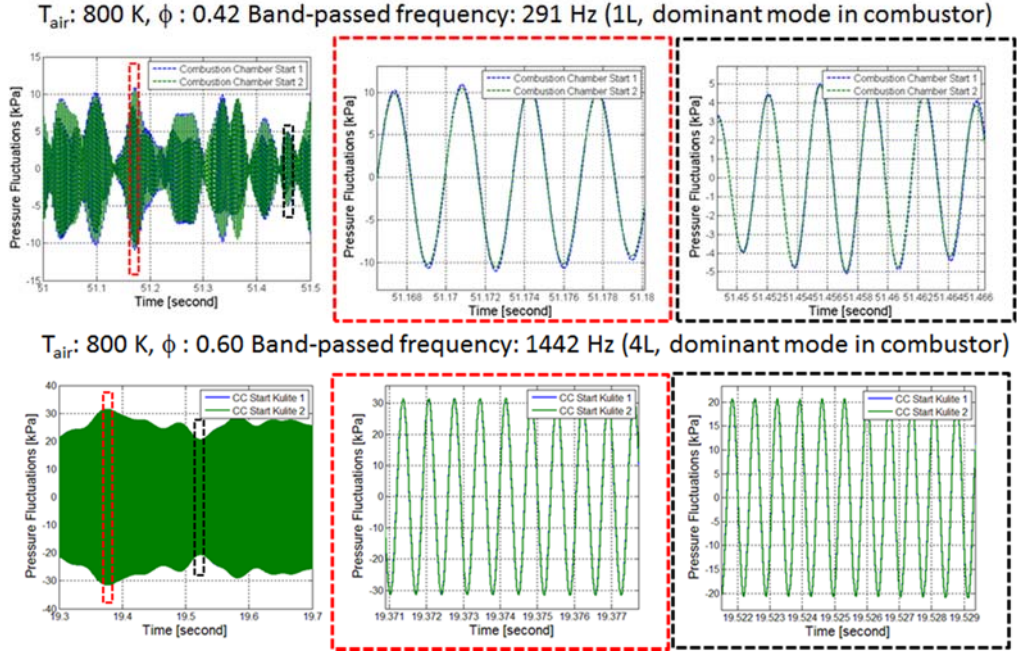


Figure 13: Modulation of pressure signal at low and high pressure fluctuation amplitudes in the LDI combustor (3/8 wave air plenum-1/2 wave combustion chamber)

#### 2.2.4. Switching of dominant modes:

During a typical test, the equivalence ratio is varied from a high value  $\sim 0.7$  to lean blow-out. The instability levels vary significantly with equivalence ratio as previously discussed. Along with the overall pressure fluctuation amplitudes, the value at each dominant mode also varies during the test. Figure 14 below shows the variation in pressure fluctuation amplitudes for the 1L mode (325 Hz), 4L mode (1420 Hz) and the high frequency mode at 7100 Hz using band-passed data. The pressure data is band-passed using a Butterworth filter of 2<sup>nd</sup> order with a band-width of  $\pm 50$  Hz and normalized using the maximum P' value at the particular mode frequency- 15 kPa at 1L mode, 95 kPa at 4L mode, and 80 kPa at 7100 Hz. A wide band-width is used to account for changes in the frequency with change in equivalence ratio during the test.

The 1L mode shows low amplitude that remains fairly constant at all high equivalence ratios and increases in amplitude when the equivalence ratio is below 0.45. The increase in the 1L mode amplitude coincides with the reduction in amplitudes of the 4L mode and the 7100 Hz mode. The 4L mode is the most dominant mode in the combustor for a large portion of the test duration. The 4L mode amplitude decreases with  $\phi$  and its amplitude is  $< 1\%$  of chamber pressure at near lean blow-out equivalence ratios. The high frequency mode at 7100 Hz mode reaches high amplitude immediately after ignition with amplitudes comparable to the 4L mode. Its amplitude decreases significantly in the equivalence ratio range of 0.7 to 0.6 before increasing again in amplitude. Similar to the 4L mode, its amplitude decreases significantly at lean equivalence ratios near flame blow-out.

The distinct behavior of the dominant combustor modes as a function of equivalence ratio imply that the flame shape, hydrodynamics and the interactions between them vary significantly during the test duration. The physical mechanisms that drive each mode are highly dependent on the equivalence ratio.

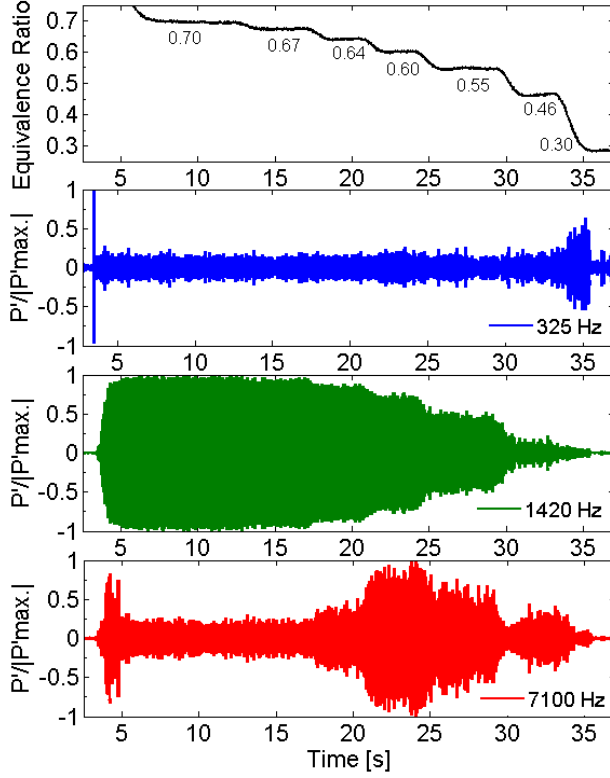


Figure 14: Equivalence ratio and band-passed pressure data ( $\pm 50$  Hz band-width) at the 1L, 4L and the 7 kHz frequencies for test performed at 800 K in the 3/8 wave air plenum-1/2 wave combustion chamber configuration (fuel nozzle at throat)

#### 2.2.5. Effect of fuel used on the combustion dynamics:

The LDI combustor was operated using two fuels, Jet-A and FT-SPK. Table 3 below shows a comparison between the major properties of the fuel that were obtained from the vendors. The major difference between the two fuels is the negligible amount of aromatics present in the FT-SPK fuel.

Table 3: Comparison between Jet-A and FT-SPK fuels used

Property	Phillips 66 Jet A	PetroSA PS 150
Density [ $\text{kg/m}^3$ ] (at 293 K)	775-840	765
Kinematic Viscosity [ $\text{cm}^2/\text{s}$ ]	0.015-0.025	0.016
Flash Point [K (F)]	310-338 (100-150)	340 (153)
Vapor Pressure [kPa] (at 293 K)	0.0533	0.06
Auto-ignition Temperature [K (F)]	483 (410)	500 (442.4)
Aromatic Content	18%-20%(25% max)	0.006%(0.05% max)

The combustion dynamics behavior for the two fuels show distinct differences as the air temperature and equivalence ratio is changed. Instability results with FT-SPK fuel show more stable behavior of the LDI element at lower equivalence ratios ( $\phi < 0.45$ ) and more unstable behavior at higher equivalence ratios ( $0.46 < \phi < 0.66$ ) than corresponding tests

performed using Jet-A. The dominant modes at different equivalence ratios regimes remain similar for the fuels. The 4L mode and its harmonics are dominant at higher equivalence ratios. The modes in the 7 kHz range remain as strong as the dominant longitudinal modes. For the lower equivalence ratio range near lean blow-out ( $\phi < 0.45$ ) the energy is distributed in the 1L-5L modes and the amplitudes are significantly lower than at higher  $\phi$ .

Figure 15 below shows a comparison of the high pass filtered pressure data for FT-SPK (figures (a) and (b) on the left) and Jet-A (figures (c) and (d) on the right). The tests were performed in a 3/8 wave air plenum-1/2 wave combustion chamber configuration with the fuel nozzle 2.6 mm upstream of the venturi throat. The amplitudes with FT-SPK are higher at higher equivalence ratio of 0.6 than Jet-A while they are lower near lean blow-out at  $\phi=0.37$ . A similar trend is observed for other inlet air temperatures as well. This short study highlights the necessity of detailed study of the effect of fuel composition, especially for liquid fuels, on combustion instabilities in combustors.

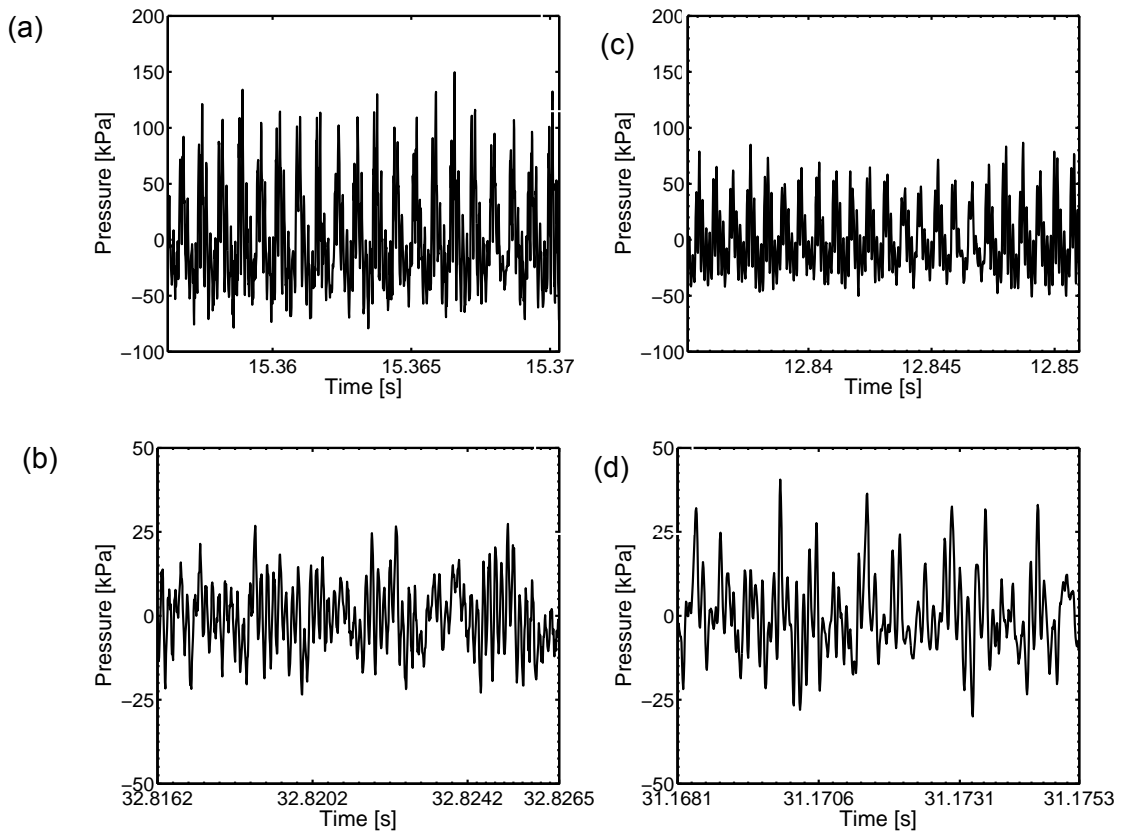


Figure 15: High-pass pressure data for tests performed using FT-SPK ((a)  $\phi=0.6$  and (b)  $\phi=0.37$ ) and using Jet-A ((c)  $\phi=0.6$  and (d)  $\phi=0.37$ ) as the fuels in the 3/8 wave air plenum-1/2 wave combustion chamber configuration.  $T_{air}= 800$  K.

### 2.3. SUMMARY AND CONCLUSIONS

Design of a model LDI combustor capable of producing self-excited combustion instabilities has been described. A parametric investigation of combustion dynamics behavior of the LDI combustor was performed and effects of combustor geometry, inlet air temperature and global equivalence ratio was studied. Based on experiments with discrete

changes in the length of the air plenum and the combustion chamber, the 3/8 wave air plenum ( $L_p$  - 0.46 m) and 1/2 wave combustion chamber ( $L_c$  = 1.08 m) length was selected as the base configuration that presented combustion instability amplitudes close to the targeted 1-3% of mean chamber pressure at high air temperature, low equivalence ratio conditions. The combustor shows distinct discriminating instability characteristics with changes in geometry and operating conditions that are important for the validation of computational models.

The 1/4 wave air plenum ( $L_c$  = 0.2 m) and 1/4 wave combustion chamber ( $L_c$  = 0.56 m) was the most unstable combustor configuration with peak-to-peak pressure fluctuations as high as 20% of the mean chamber pressure. Generally, the dominant mode in the combustor was typically present in the frequency range 1200-1600 Hz corresponding to the 4L mode in the combustor. Higher frequency modes in the 6-8 kHz range are also seen to present high pressure fluctuation amplitudes, comparable to the 4L mode amplitude at high equivalence ratios.

For the base configuration, the combustion instabilities with fuel nozzle at the throat of the venturi throat was observed to be more unstable than the configuration with fuel nozzle 2.6 mm upstream of the nozzle. At higher equivalence ratios, the 4L mode was dominant for both configurations with amplitudes between 40 and 82 kPa. At lower equivalence ratios, the energy was spread across the first five modes in the combustor, with the 1L mode dominant when fuel nozzle was upstream while 5L mode dominant when fuel nozzle was at the throat.

At the low amplitude instability conditions at lower equivalence ratios, a strong modulation in the dynamic pressure is observed. Dynamic pressure energy is distributed across several (1L-5L) low amplitude modes in the combustor. The significant difference in the energy spectrum between the high equivalence ratios cases where a dominant 4L mode is observed versus the low equivalence ratio case indicates possibility of different driving/damping mechanism at the two equivalence ratios ranges.

## 2.4. SPRAY MEASUREMENTS:

A pressure swirl atomizer ( $\text{FN} = 1.32$ ) obtained from Dr. Phil Lee (Woodward Inc.) was used for the spray characterization tests. Phase Doppler Anemometry (PDA) and high speed videos are used to characterize drop sizes, velocities, and spray cone angle. For the spray, the fuel flow rate was maintained at the same values as the combustion experiments for equivalence ratios of 0.4, 0.5, and 0.6. The spray tests were performed at atmospheric pressure with and without a co-flow of air around the fuel injector. The fuel flow rate is measured across a cavitating venturi (0.635 mm throat diameter) and verified based on the pressure differential across the injector. For experiments with co-flow of air, the air flow rate is regulated to maintain a  $\Delta P/P$  of 4% across the injector which is similar in value measured during the combustion experiments. The air co-flow passes through the swirler and the subsonic venturi. The swirler has six helical axial vanes with a lead angle of  $60^\circ$  leading to a swirl number of approximately 0.8. A schematic diagram of the test arrangement is attached below in Figure 16.

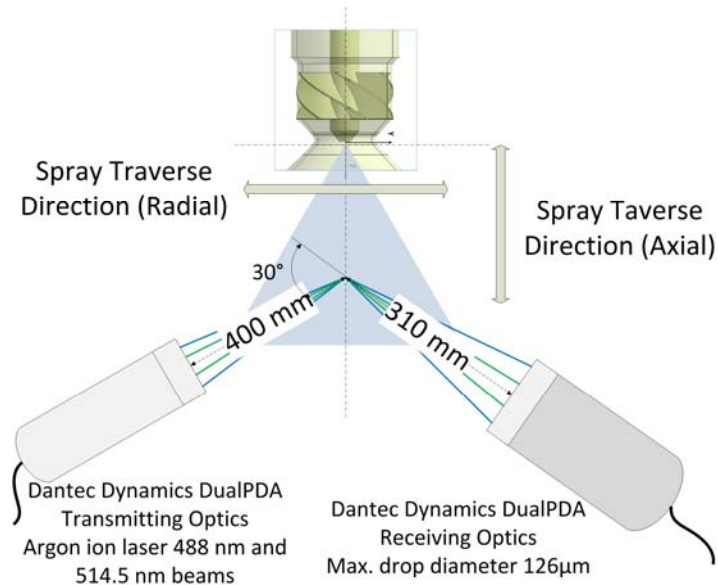


Figure 16: Schematic diagram of PDA test arrangement

Drop sizes and velocities were recorded with a phase Doppler anemometer (PDA). The PDA determines the velocity of individual particles based on the frequency shift of light which is reflected or refracted by a moving particle. Drop size is estimated by comparing the phase shift between two detectors at known locations. For the results reported here, a Dantec Dynamics Dual-PDA system was utilized. This system uses an argon-ion laser, beam splitter (514.5 and 488.0 nm wavelengths), and transmitter (400 mm focal length) to create orthogonal measurement volumes for simultaneous recording of two velocity components. The receiver (310 mm focal length) was placed at a scattering angle of  $45^\circ$ , resulting in a theoretical maximum detectable drop diameter of 126  $\mu\text{m}$ , as reported by the PDA software (BSA Flow Software version 4.00.00.42). To capture the local statistics, 10,000 to 20,000 individual drops were recorded based on the measurement location (10,000 where data rate was very low). Data rates (20–4300 Hz) and spherical validation values (90–100%) varied depending upon the operating conditions and measurement locations.

High speed visible imaging was also used to visualize the spray. A high-speed visible camera (Vision Research Phantom v7) with a 105 mm lens was mounted perpendicular to the spray axis, and a 150 W light source and diffuser plate were positioned behind the spray to provide

backlighting. The spatial resolution of the visible intensity measurements was 167  $\mu\text{m}$  for each pixel at the center of the spray. The visible camera integration time (20  $\mu\text{s}$ ) and aperture size ( $f/22$ ) were selected to optimize the camera sensitivity.

For the spray measurements, the uncertainty in measurement location in the spray was approximately +/- 1 mm for both axial and radial traverses. The fuel flow rate was measured across a choked venturi of known co-efficient of discharge. The uncertainty in measurement in the flow rate of fuel was at most 3%. The flow rate of air was based on pressure drop across the pressure swirl atomizer. This measurement was made using a differential pressure gauge with an uncertainty of 0.83 kPa.

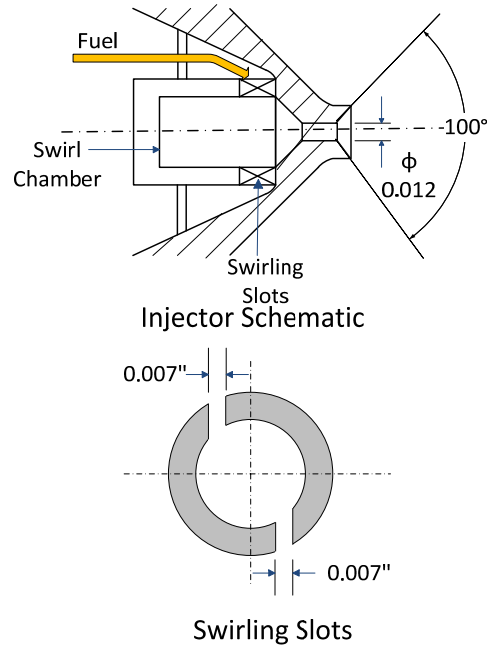


Figure 17: Schematic diagram of experimental arrangement in the laboratory along-with image of the experiment and spray

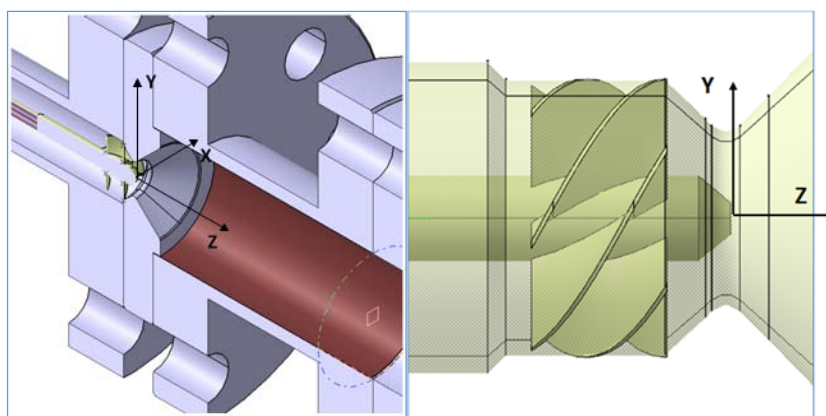


Figure 18: Schematic diagram of the fuel-injector-swirler-venturi configuration

## 2.4.1. Results

### 2.4.1.1. Spray measurements without co-flowing air

A snapshot from the high speed video taken from the experiment is shown in Figure 19. The spray-cone angle determined based on image data shows good agreement ( $\sim 6\%$ ) with computational results. The spray cone angle values measured based on the images are tabulated in Table 4 below.



Figure 19: Instantaneous snapshot of spray without co-flow of air

Table 4. Spray cone angle determined experimentally using high speed imaging data (no air co-flow)

$\dot{m}_f$ (g/s)	$\phi$	$\theta$
2.27	0.4	70°
2.84	0.5	69°
3.35	0.6	68°

Drop size distribution and axial velocity profiles based PDA measurements are presented in Fig. 20. The measurements were conducted at multiple radial locations in the spray at three axial planes. The z-direction as shown in Fig. 18 is in the axial direction of the spray with the origin being at the exit tip of the atomizer. The drop-sizes characterized by the Sauter Mean Diameter (SMD,  $D_{32}$ ) lie between 20-50 $\mu$ m.

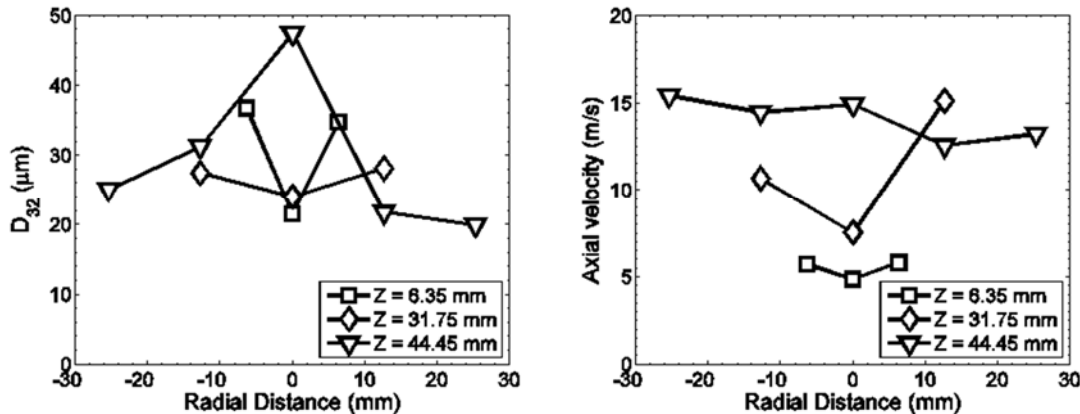


Figure 20:  $D_{32}$  (SMD) and mean axial velocity for PDA measurements at different locations in the spray. Jet-A flow rate 2.7 g/s

#### 2.4.1.2. Spray modeling and measurement with co-flowing air

The fuel spray measurements have also been conducted with a co-flow of air around the injector. The spirally distorted and spinning motion of the spray is observed in the experiment. An image from the high speed video of the spray is shown below in Fig. 21. The fuel injector tip is located approximately 15 mm upstream of the venturi exit which is visible in the image.

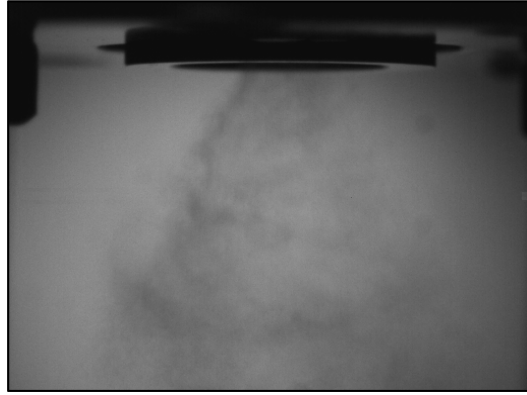


Figure 21: Instantaneous snapshot of spray with co-flow of air

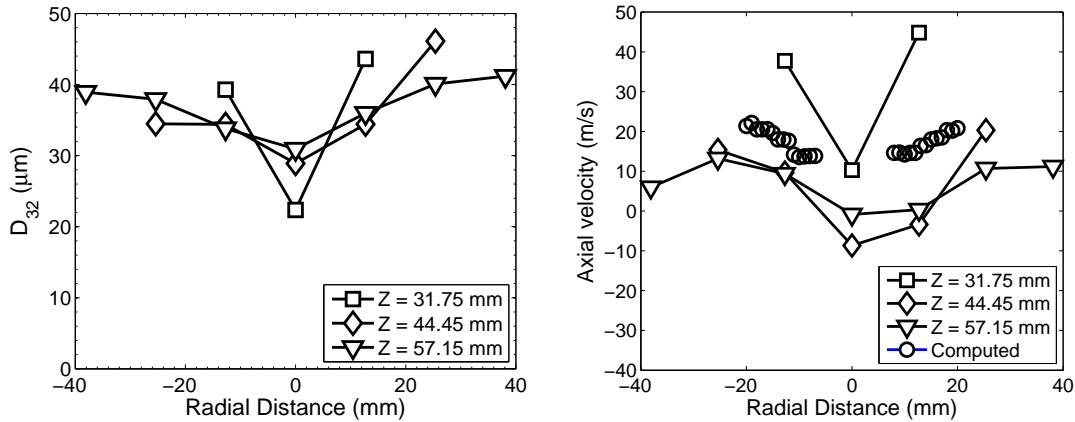


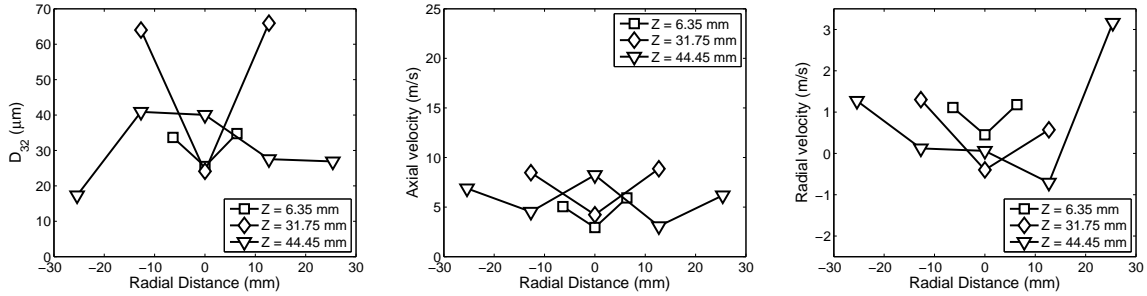
Figure 22:  $D_{32}$  (SMD) and mean axial velocity for PDA measurements at different locations in the spray. Jet-A flow rate 2.7 g/s.  $\Delta P/P$  4%

Drop size distribution and axial velocity profiles for the spray with co-flowing air are presented in Fig. 22 above. It is important to note that the axial slices at which measurements were made are different than the case with no co-flow of air. This is on account of not being able to access the region covered by the venturi. The overall level of drop size for the spray with co-flowing air is between 30–40 $\mu\text{m}$ . The drop-sizes for axial locations 44.75 mm and 57.15 mm are of the same order. The drop-size right downstream of the nozzle is smallest (~20 $\mu\text{m}$ ). The axial velocity by co-flowing air may contribute to reducing the relative velocity between spray drops and gas so that the larger drops are produced particularly away from the center. As indicated, larger axial velocity profile is shown at the near-nozzle plane,  $Z = 31.75 \text{ mm}$ , in Fig. 22. It is also noteworthy to observe the backflow in the middle at  $Z = 44.75$  and  $57.15 \text{ mm}$ . The swirl number of the jet in this experimental set-up is approximately 0.8. For such high swirl numbers, a central toroidal recirculation zone (CTRZ) is commonly observed on account of adverse axial pressure gradients exceeding the inertial forces of droplets leading to reversal in flow. Based on axial velocity distribution, the second plane,  $Z = 44.45 \text{ mm}$ , is the stagnation point and the third plane,  $Z = 57.15 \text{ mm}$ , is located in the CTRZ.

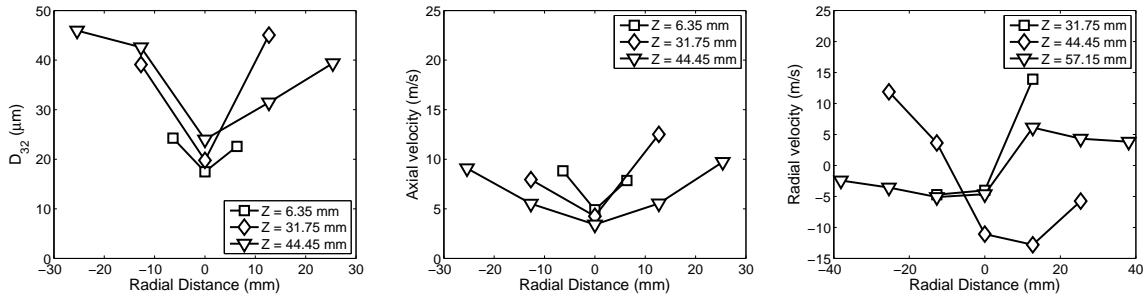
A compilation of spray measurements at other equivalence ratios, with and without a co-flow of air are presented below.

### Spray Measurements without co-flowing air:

#### Equivalence Ratio 0.40



#### Equivalence Ratio 0.50



#### Equivalence Ratio 0.60

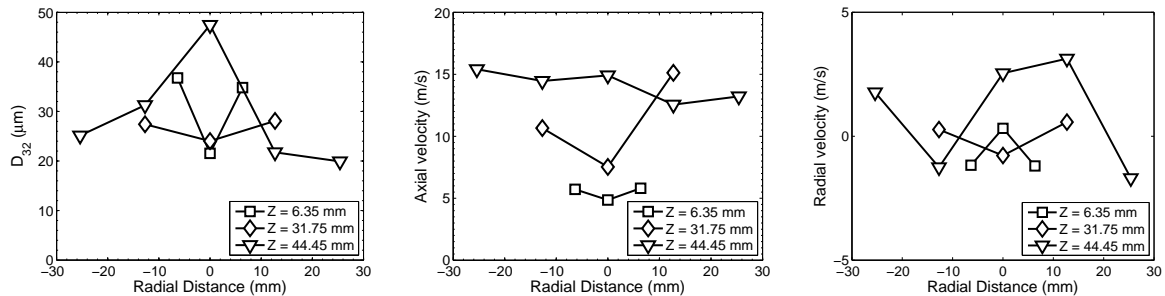
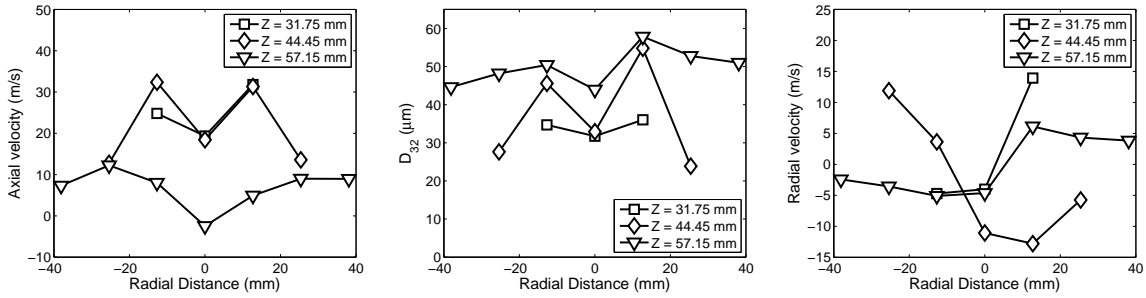


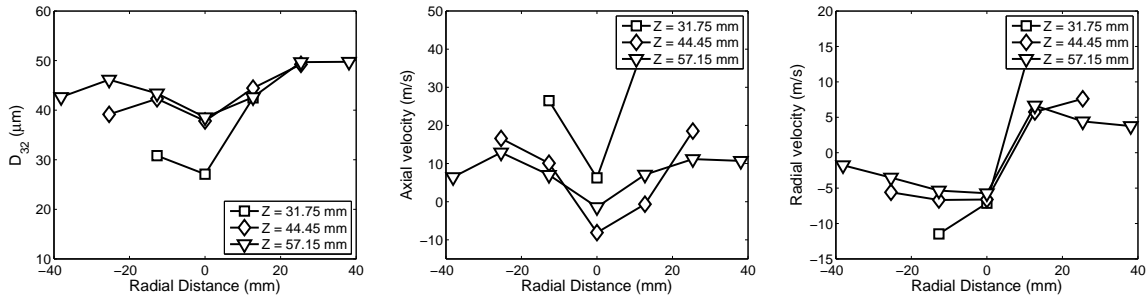
Figure 23: Spray measurement results without co-flow of air

## Spray Measurements with co-flowing air:

### Equivalence Ratio 0.40



### Equivalence Ratio 0.50



### Equivalence Ratio 0.60

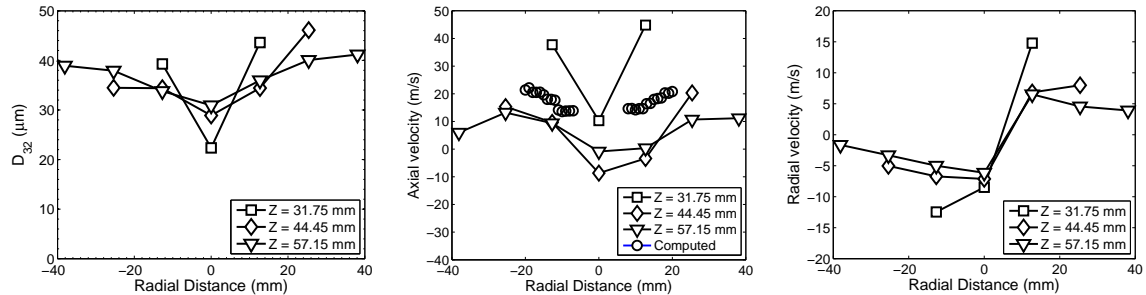


Figure 24: Spray measurement results with co-flow of air

### 3. OH PLANAR LASER INDUCED FLUORESCENCE MEASUREMENTS:

#### 3.1. OPTICAL CHAMBER:

An optically accessible section of the combustor was designed to allow high repetition rate laser based diagnostic measurements, both OH PLIF and PIV at 10 kHz. Results from the simulations indicated that the active combustion was isolated to a small region in the diverging section of the venturi and immediately downstream of the combustor dump-plane. Based on this information, the optical section was designed to obtain a field of view of ~100 mm x 50 mm starting at the combustor dump plane. The flame length for all operating conditions of the combustor is approximately one chamber diameter so the field of view was sufficient to measure the flame with PLIF as well as the important flow structures with PIV. The subsonic venturi section of the combustor however was not optically accessible.

The optical chamber section was designed with a double windowed design where the inner thin quartz tube (2.5 mm thickness) contains the flame. The outer quartz window is thicker (12.7 mm thickness) and the cavity between the window and the tube is pressurized using 800 K hot air to maintain a cavity pressure slightly higher than the combustion chamber pressure. This double windowed configuration with a pressurized cavity minimizes the pressure and temperature gradient across the inner thin quartz tube and allows operation with a thin cylindrical tube. A thin tube will minimize optical distortion of the image due to the cylindrical surface. The entire construction of the optical chamber was made using Hastelloy-X which provides excellent strength at high operating temperatures. All the static seals for the assembled parts of the optical chamber were made using 1/16" thick Grafoil (99% carbon) sheets. The chamber provides optical access on four sides, of which one is used to bring the laser sheets for OH-PLIF and PIV into the chamber, one for laser ignition and two for imaging. Schematic diagrams of the optical chamber are shown in Figure 25 and Figure 26 below.

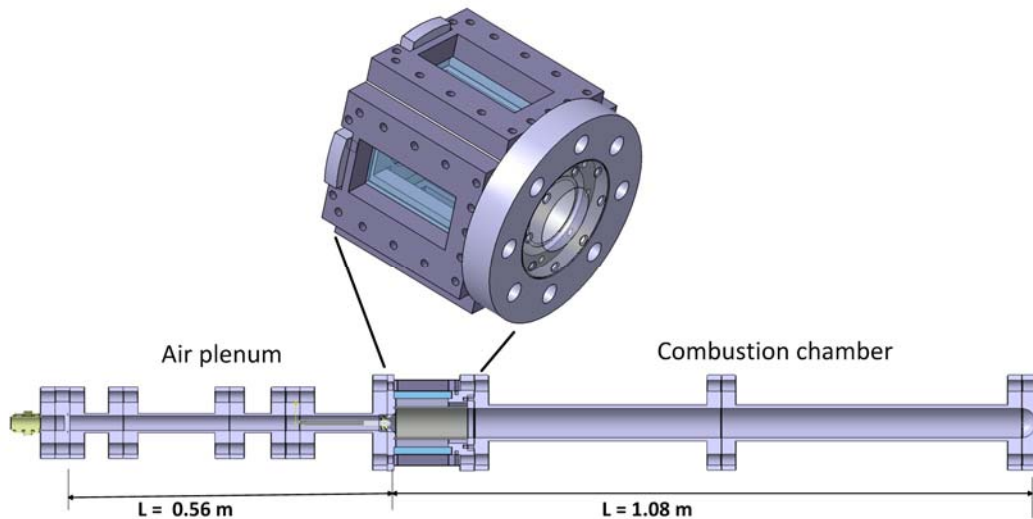


Figure 25: Location of the optical section on the LDI combustor

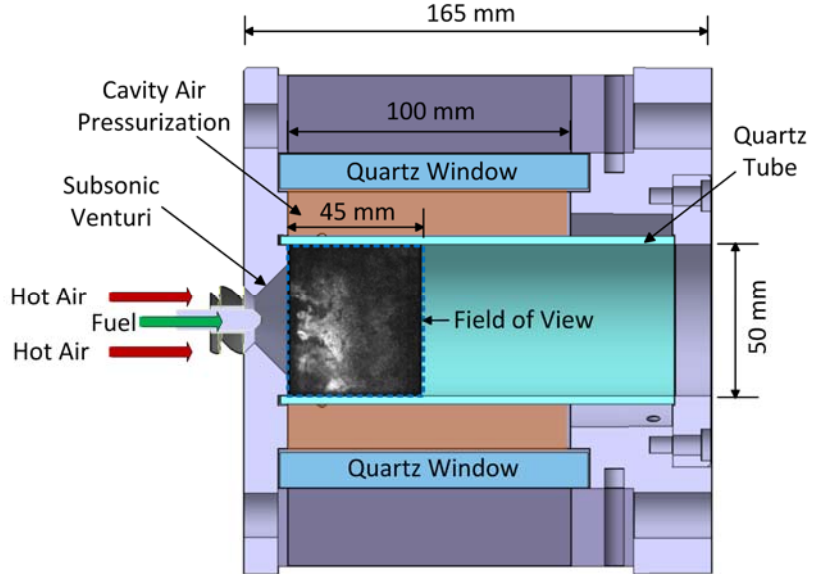


Figure 26: Schematic diagram of the optically accessible section of the LDI combustor

### 3.2. PLANAR LASER-INDUCED FLUORESCENCE:

OH-Planar laser-induced fluorescence (OH-PLIF) is used to measure the spatial distribution of the OH-radical in reacting flows along a two-dimensional plane. In laser induced fluorescence the absorption of a temporally- and spectrally-resolved plane of light helps excite the targeted molecules in its path to an excited state through an allowed transition. The spontaneous decay of the molecules from the excited state manifold to a lower energy manifold leads to the production of the fluorescence signal that is measured. Strong intermolecular collisions can cause molecules to decay from the excited energy level back to the ground state without emission of a photon through the process of quenching. In the linear regime, the fluorescence signal is linearly proportional to the number density of the targeted species in the ground state, the rate of stimulated absorption, and the ratio of the rate of spontaneous emission from the excited state manifold to the ground state manifold to the total rate population decay from the excited state [27].

In high pressure flames, there are several effects that can lead to difficulty in performing useful PLIF measurements. The number densities of the targeted species will be greater in high-pressure flames, leading to increased signal levels. However high number densities can also lead to significant absorption and attenuation of the excitation laser sheet as it propagates through the medium [28-31]. Re-absorption of the fluorescence signal as it propagates from the probe volume, through the flame, to the detection system is a well-known effect that can also become more pronounced under high-pressure conditions [29, 31]. Increased occurrences of collisional processes act as damping effects which broaden the frequency width of the resonance susceptibility, reducing the peak strength of the coupling between the transition and the incident laser field.

Another measurement limitation is related to the noise characteristics of the HS-CMOS/IRO detection systems, which can be very difficult to accurately quantify [32]. In this work, the detector noise was estimated using a series of homogeneous white-field images acquired at comparable levels of signal and gain. The single-pixel noise value was established as the standard deviation of the offset-corrected white-field signal, capturing the broadband, uncorrelated sensor noise. The mean SNR for the flames was 7.55 and 6.28 for the flames at equivalence ratios of 0.6 and 0.44 respectively.

The OH-PLIF laser system comprised a high-repetition rate, Q-switched, DPSS Nd: YAG pump laser (Edgewave INNOSLAB IS200-2-L) and a dye laser designed for efficient operation at low pulse energies and high average power (Sirah Credo). The frequency-doubled output from the pump laser provided 7.8 mJ/pulse at 10 kHz (78 W average power) with a 9.2 ns pulse duration. Using Rhodamine 590 Perchlorate dye (dissolved in ethanol), the 566.3986-nm fundamental wavelength was frequency doubled to 283.2 nm to excite the Q1 (8) line of the A  $^2\Sigma^+$  ( $v' = 1$ )  $\rightarrow$  X $^2(v'' = 0)$  transition. The average laser pulse energy at 283.2 nm was 0.68 mJ/pulse for 10 kHz operation (6.8 W average power). The first surface reflection from an uncoated fused silica window directed a small amount of the total beam energy through a Bunsen flame. The resulting LIF signal generated was collected with a photomultiplier tube and the average signal monitored with an SRS BOXCAR integrator and an oscilloscope.

The PLIF excitation sheet was formed using two cylindrical lenses ( $f_{PLIF, 1} = -25\text{mm}$ ,  $f_{PLIF, 2} = 300\text{mm}$ ) in a cylindrical telescope arrangement, resulting in a collimated sheet height of approximately 30 mm. A third cylindrical lens ( $f_{PLIF, 3} = 600\text{mm}$ ) was used to focus the sheet to the beam waist at the combustor centerline. The sheet width was measured by traversing a narrow slit through the sheet waist and measuring the transmitted power with a photodiode. On the combustor centerline, the sheet thickness was measured to be approximately 500  $\mu\text{m}$  (FWHM). The calculated Rayleigh range for sheet waist was approximately 35 mm; therefore, it was assumed that there was minimal variation in the laser fluence across the span of the combustor. The peak laser fluence was  $9 \times 10^7 \text{ W/mm}^2$ . The OH-PLIF signal was collected using a 100-mm focal length, f/2.8 objective lens (Cerco Sodern Type-2178). A multi-channel plate intensifier (LaVision HS-IRO) was used to amplify the signal, which was imaged by a high-speed CMOS camera (Phantom v411). The intensifier gate width was run at the minimum value possible (100 ns) to minimize background noise from flame luminosity. An optical band-pass filter (Semrock 320/40) was used to transmit the fluorescence from the A  $^2\Sigma^+$  ( $v' = 1$ )  $\rightarrow$  X $^2(v'' = 1)$  and A  $^2\Sigma^+$  ( $v' = 0$ )  $\rightarrow$  X $^2(v'' = 0)$  bands occurring over the 305–320 nm range of wavelengths. The effective filter width was sufficient to block the entire wavelength range of the intensifier photocathode sensitivity, removing elastic scattering of the laser beam from the seed particles and further reducing background flame luminosity. The filter had a transmission efficiency of >98 % over the selected bandwidth and an ultra-steep transmission cutoff (<1 nm). The maximum array size for the OH-PLIF CMOS camera, operating at a 10 kHz frame rate, was  $543 \times 585$  pixels. For the field of view indicated in Fig. 26, this resulted in an image resolution of 97.4  $\mu\text{m}/\text{pixel}$  in the raw data images.

### 3.3. OPERATING CONDITIONS:

The OH-PLIF measurements were performed at a range of equivalence ratios for constant inlet air temperature to the LDI combustor of 800 K. The 3/8 wave air plenum and 1/2 wave combustor chamber configuration of the combustor was used for all the tests with the fuel injector located 2.6 mm upstream of the venturi throat. Details of the operating conditions are tabulated in Table 5 below.

Table 5: OH-PLIF Summary of operating conditions

Test ID	$T_{air}$ (K)	$\phi$	$\dot{m}_{air}$ (g/s)	Camera and Laser settings				Laser Power (W) (UV)
				Intensifier Gain	Intensifier Gate (ns)	Camera Exposure ( $\mu\text{s}$ )		
PLIF 22	795	0.6	81.6	65	100	97		6.7
PLIF 25	795	0.55	81.6	65	100	97		6.7
PLIF 18	800	0.48	81.6	66	100	97		6.7
PLIF 19	800	0.44	81.6	65	100	97		7.0

### 3.4. RESULTS:

#### 3.4.1. PLIF 22: High Equivalence Ratio Test-Case ( $\phi: 0.60$ )

##### 3.4.1.1. Pressure and OH-PLIF Time History

The OH-PLIF measurements were conducted at varying equivalence ratios as highlighted by the operating conditions tabulated above. The high equivalence ratio test case ( $\phi=0.6$ ) is presented first. This test presents high amplitude instabilities between 80-150 kPa with the dominant pressure instability at the 4L mode at 1450 Hz. The harmonics of this mode are also strong in amplitude. The high frequency range between 5-7 kHz shows instabilities as high as the 4L mode in some cases. The lower modes 1L-3L are also present but at lower amplitudes. These become stronger in amplitude as the equivalence ratio is reduced while the higher frequency modes drop in amplitude. From the simulations it is clear that pressure and velocity resonances control the structure of the flame and where it stabilizes during a high amplitude instability. The presence of several strong modes adds complexity to the flame structure, especially at a lower equivalence ratio where the mode amplitudes are similar. At a higher equivalence ratio of 0.6, however, the structures are more coherent and easier to follow.

Figure 27 below shows the high pass filtered pressure data for a time-slice when the OH-PLIF images were obtained. The pressure-time history shows a near limit cycle like behavior with near constant pressure oscillation amplitude from cycle to cycle. A magnified image of the pressure data for a shorter time-slice is presented on the right of the figure. The pressure signal shows an overarching 4L cycle with multiple pressure peaks enveloped under it. These shorter pressure cycles correspond to the higher frequency peaks in the 5-7 kHz frequency range, which are not resolved by the OH-PLIF measurement which is limited to a repetition rate of 10 kHz. The power spectral density plot of pressure measured near the exit nozzle of the combustor is presented in Figure 28 (note PSD plots presented earlier were of data at the combustor head end, and had a somewhat different appearance). Possible, related sources for the large number of modes indicated by the PSD include the numerous couplings between the strong thermo-acoustics in a highly-confined combustion zone, hydrodynamic modes related to the high swirl number ( $S \sim 1$ ) flow entering the combustor, the continually changing cross-section area in the diverging section of the venturi that could lead to wave dispersion and complex interactions with heat release, and nonlinear couplings between hydrodynamics, heat release, and acoustics.

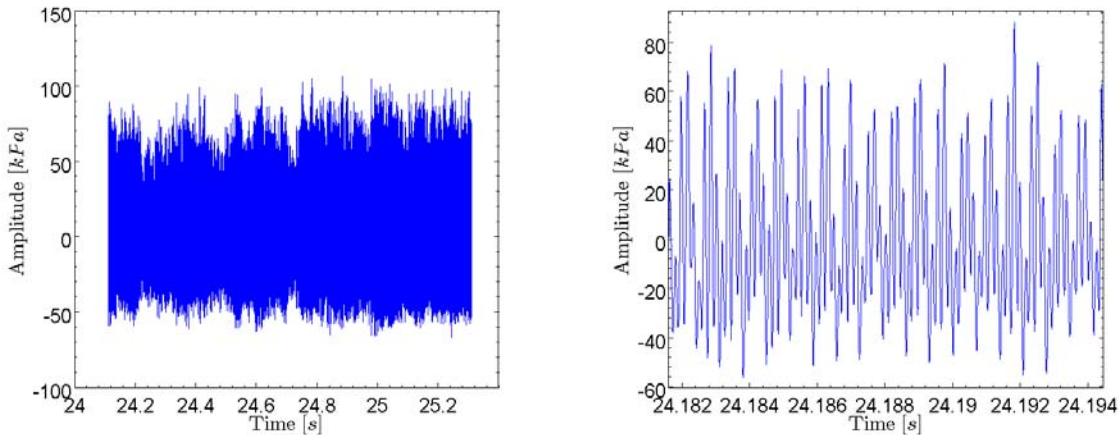


Figure 27: High pass filtered pressure measurements for PLIF 19 test case (a) over the time slice selected for image analysis (b) shorter time slice for better visualization of data

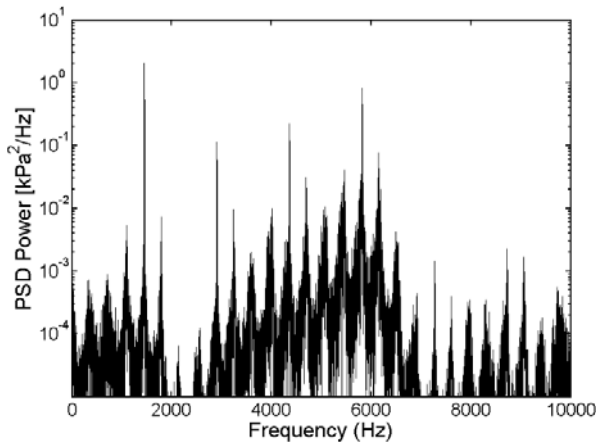


Figure 28: Power Spectral Density (PSD) of the pressure signal measured near the exit nozzle of the combustor (pressure anti-node)

The strong instability amplitudes at  $\phi=0.6$  lead to the formation, transport and breakdown of periodic and coherent flow structures. This case is presented in detail in the following section. Summaries of the various data analysis techniques that were used are provided as the results are presented.

### 3.4.1.2. Flame Front Extraction

For the study of the combustion response to the combustor acoustics, a key parameter of interest is the location of the flame-front. Since OH persists in the combustion zone for a longer time than the heat-releasing reactions, it cannot be directly used as a flame marker. However, the sharp spatial gradient in intensity of the OH-PLIF signal has been used as a marker of the reaction zone in lean premixed pre-vaporized flames [33, 34]. This method is sensitive to the SNR and becomes challenging in high power, high pressure turbulent non-premixed flames. In highly swirled flames where multiple vortex breakdown mechanisms help flame holding and stabilization through transport of combustion products and radicals back to the reaction front; the OH consumed through three body recombination reactions in the post combustion zone and the long residence time of the radicals in the low-velocity recirculation zones can make detection of the flame front challenging. The inherent 3-D nature of the highly wrinkled swirling flames can make understanding of the extracted flame-front challenging as well. As such, the high intensity in the OH-PLIF signal was used to demarcate the super-equilibrium OH formation while the low intensity regions were considered to be the lower temperature unburnt gases or combustion products [35, 36]. The procedure prescribed by Slabaugh et al [35] was used in this study.

Figure 29 below shows an instantaneous snapshot of the OH-PLIF image taken in the LDI combustor. First the raw image was corrected for distortion, camera sensitivity and laser sheet intensity and then binned using a  $2 \times 2$  pixel kernel to improve the SNR. This image is shown in Figure 29 (a). An edge-preserving nonlinear diffusion filter was then applied to remove uncorrelated detection system noise and low magnitude signal gradients in the burnt gases. A Gaussian smoothed spatial gradient was then extracted which was followed by binarizing of the gradient using on a user defined threshold based on the signal intensity. The smoothed image is shown in Figure 29(b). The obtained contour was finally morphologically thinned and filtered to obtain a flame front. The flame front overlaid over the enhanced image is shown in Figure 29 (c).

Good visual agreement is seen between the spatial location of the extracted contour and outer periphery of the corresponding regions of high OH signal intensity. The small breaks in the detected flame surface in regions where the spatial gradient in the OH-PLIF signal remain high

are the artifacts of morphological filtering operations, which were required for robust suppression of false-flame edges in the low SNR images. The flame front contour is extracted as a mathematical function that denotes the spatial location of the flame front.

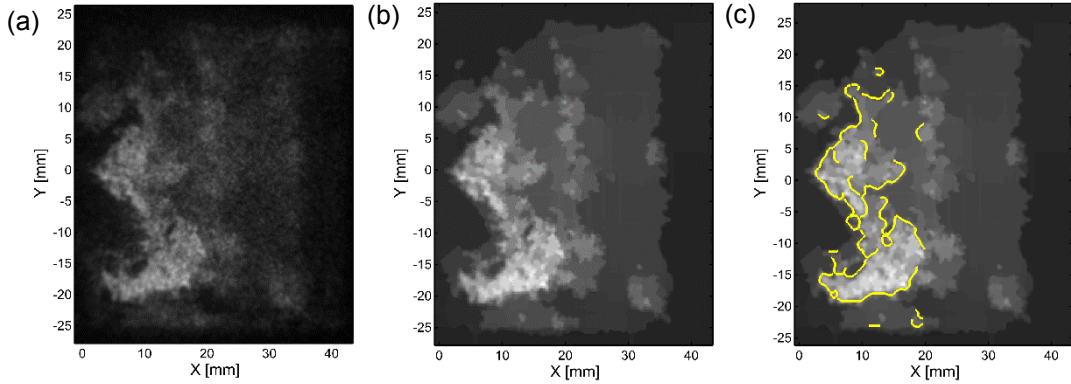


Figure 29: Instantaneous snapshots of the OH-PLIF measurements (a) corrected (b) enhanced and (c) overlaid with extracted flame-front

The length of the flame front is tracked through time and a power spectrum of the flame front length is presented alongside the pressure power spectral density in Figure 30 below. The flame spectrum shows a strong response at the frequency corresponding to the 4L mode in the combustor, and significant responses at the 3L and 8L mode frequencies.

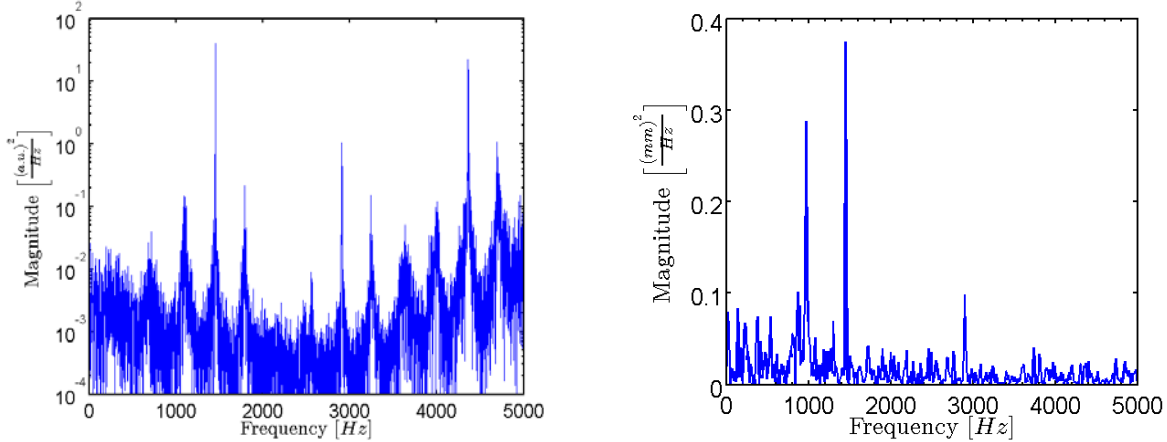


Figure 30: PSD of pressure and extracted flame front length

### 3.4.1.3. Flame Surface Density

A planar analog of flame surface density commonly used in simulations to denote the reaction rate was calculated from the flame front extracted from the experimental data. The planar flame surface density [35] is given by,

$$\Sigma = \frac{\partial A_f}{\partial V}$$

where,  $A_f$  is the flame surface area defined over a volume  $V$ . The domain was divided into 1 mm x 1 mm domains and the total flame front length in each domain was calculated over a range of 1000 OH-PLIF images and summed.

Figure 31 below shows the flame surface density contour. The flame contour shows a fairly symmetric distribution across the central axis of the combustor. A C-shaped pocket of higher amplitude flame surface density is seen about the central axis with a lower amplitude region located inside the C. This lower amplitude region includes the transport of combustion products through reversal of flow from the vortex breakdown bubble (VBB) region towards the flame front. The flame is stabilized approximately 3-4mm from the dump plane at the leading edge of the VBB.

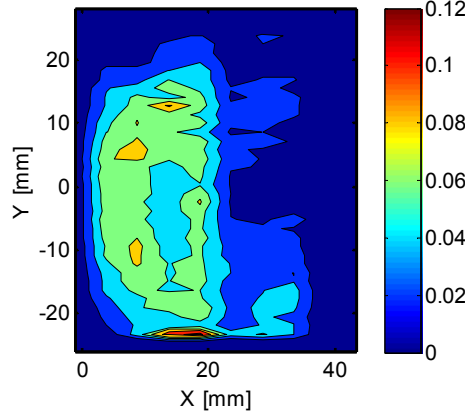
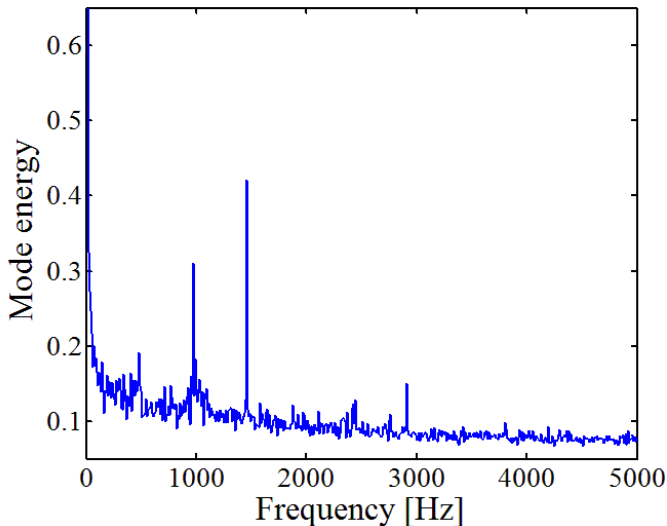


Figure 31: Flame Surface Density

#### **3.4.1.4. Dynamic Mode Decomposition Analysis**

The use of Dynamic Mode Decomposition (DMD) provides a clear insight into the dynamic patterns of the quantities of interest such as heat release, OH-signal intensity, velocity, species concentrations, etc. The DMD procedure is similar to Proper Orthogonal Decomposition (POD) that is widely used for the decomposition of large data-sets, but whereas POD modes typically contain multiple frequencies, each DMD mode is only of a single frequency. Comparisons between the DMD and POD analyses applied to axial combustion instabilities by Huang et al. [21] led to the conclusion that the underlying physics can be more efficiently understood with DMD, especially when there are strong instabilities present at multiple frequencies.

Figure 32 below shows the DMD mode spectrum calculated using 1000 images with a time separation of 0.1 ms between each. Strong peaks at 973 Hz and at the 4L (1459 Hz) and 8L (2909 Hz) mode frequencies and lower amplitude modes at 480 Hz and the 1L (340 Hz) are observed. The spatial mode-shape for some these modes is presented in the next section. The DMD modes for the 4L and 8L modes align well with the strongest frequencies present in the pressure spectrum shown in Figure 28 and Figure 30. Other acoustic modes do not show up on the DMD spectrum. The 973 Hz mode response is strong but is not present in the acoustic spectrum. This mode shows a strong swirling behavior as seen in the next section and its absence from the acoustic spectrum may be on account of 2D representation using OH-PLIF signal of a 3D phenomenon. It is important to note that these DMD modes of OH are limited to window downstream of the dump plane, and that significant combustion occurs in the diverging section of the venturi that is inaccessible to optical measurements.



*Figure 32: DMD Mode Spectrum*

#### 3.4.1.4.1. DMD Spatial Mode Shapes:

The spatial mode shapes for the dominant DMD modes are presented in Figure 33 through Figure 37 for frequencies of 340 Hz (1L), 480 Hz, 973 Hz, 1459 Hz (4L) and 2909 Hz (8L) respectively. For each mode two snapshots are presented,  $180^\circ$  out of phase with each other corresponding to a local maximum and minimum of the OH signal. The DMD analysis is performed using mean subtracted images so only the fluctuations in the OH-PLIF signal is visible.

For the low frequency modes, 340 Hz (1L) and 481 Hz, the response is primarily longitudinal in nature though both modes show some asymmetry in the radial direction that could be due to swirl. A more thorough examination of the cycle shows the mode has a longitudinal character overlaid with a slower swirling motion that follows the outer shear layer of the vortex recirculation bubble (VBB). The 481 Hz mode is absent from the pressure spectrum but is clearly present on the DMD spectrum, suggesting a combustion response to a purely hydrodynamic mode. The motion at the 481 Hz mode occurs along the V-shape of the flame.

The 3L (973 Hz) and 4L (1459 Hz) are strong in amplitude and clearly show evidence of a swirling flow. The 973 Hz mode shows opposite (red and blue) intensity lobes in the top and left half of the images that indicate a bulk swirling motion in the combustor. This frequency however does not correspond to any acoustic frequency presented in *Figure 28*. The 1459 Hz (4L) mode corresponds to the strongest acoustic mode in the combustor. The spatial mode shape show a symmetric high intensity region about the central axis of the combustor with two lobes on either side of it that are exactly opposite in intensity. A further analysis of this mode is described in the next section. The 2909 Hz mode is a harmonic of the 4L mode.

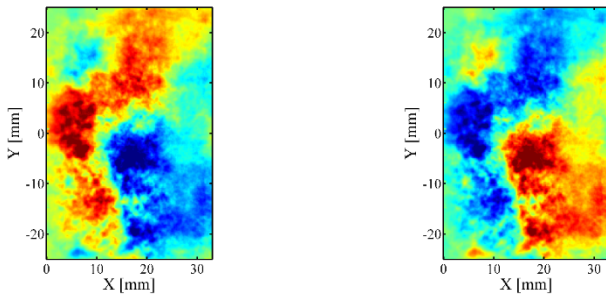


Figure 33: DMD spatial mode at f 340 Hz at the peak (left) and trough of the OH-signal (right)

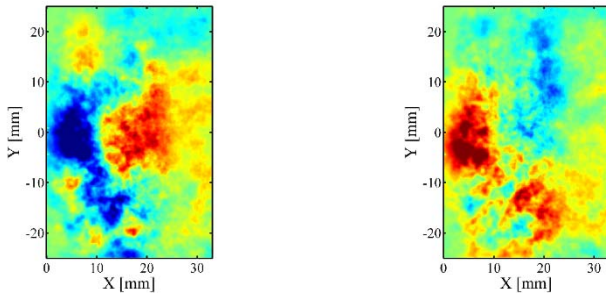


Figure 34: DMD spatial mode at f 481 Hz at the peak (left) and trough of the OH-signal (right)

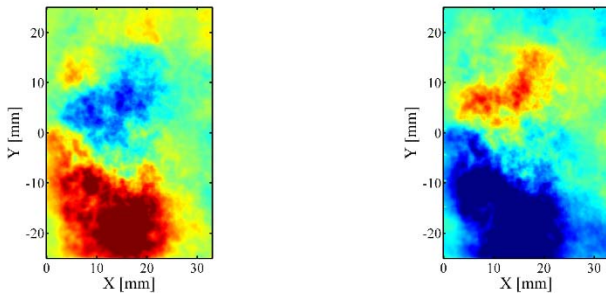


Figure 35: DMD spatial mode at f 973 Hz at the peak (left) and trough of the OH-signal (right)

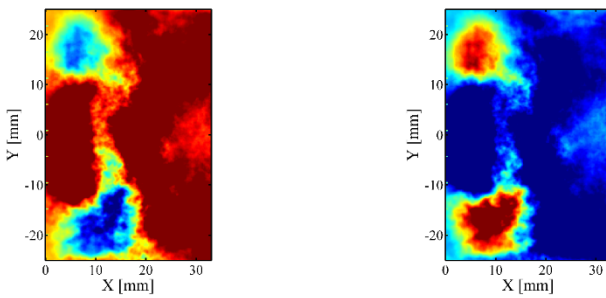


Figure 36: DMD spatial mode at f 1459 Hz at the peak (left) and trough of OH-signal (right)

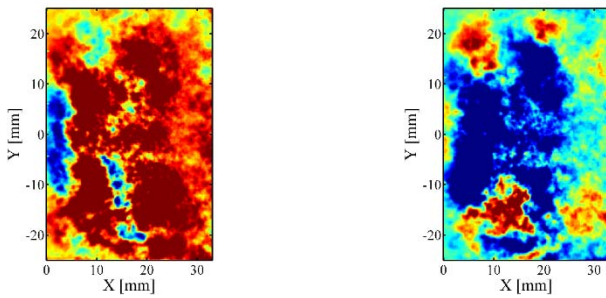


Figure 37: DMD spatial mode at f 2909 Hz at the peak (left) and trough of the OH-signal (right)

### 3.4.1.4.2. Cycle Analysis

Snapshots representing one cycle (0 to  $T$  s) of the 1459 Hz DMD mode of the OH signal are shown in *Figure 39* below. The cycle is extracted based on the temporal signal of the DMD mode. As shown in Figure 38 below, the band-pass filtered (at 1459 Hz) wall pressure measurement near the exit nozzle is in phase with the DMD temporal signal. For the 4L mode, the pressure near the exit nozzle is in phase with the pressure near the head end of the chamber. The acoustic compression and expansion processes are in phase with the OH-signal intensity where the PLIF signal is measured in the combustor. The separation in the time between snapshots is 1 ms, or  $1/T$ . At the start of the cycle, defined as a minimum in the OH signal, two high intensity lobes axisymmetric lobes are observed near the combustor wall close to the dump plane. These high intensity zones may correspond to leftover pockets of hot combustion products in the outer recirculation zones. As the OH-signal increases, high intensity lobes are replaced with a fresh mixture of fuel and air (low intensity lobes). When the OH-signal is at its maximum point in the cycle (at  $t = 4T/7$ ), the signal intensity is high across the PLIF sheet (except for the two low intensity lobes) and a V-shaped structure can be seen along the edges of possible a vortex breakdown bubble. This may suggest a reaction flame front along the shear layer of vortex recirculation bubble (VBB) that is anchored near the dump plane near its stagnation point. The stagnation point of the VBB is along the central axis of the combustor and at the upstream edge of the VBB. Due to the low velocity in the VBB and the pressure differential between the VBB and the surrounding shear layer, some of the combustion products may be transported back into the VBB and flow upstream towards the dump plane to pre-heat the incoming fuel and air. After this point in the cycle, the intensity across the PLIF sheet is lower, and high intensity lobes start forming close to the combustor wall near the dump plane. This may correspond to an acoustic expansion wave near the dump plane which draws in more fuel and air into the combustion chamber from  $t = 5T/7$  and  $t = 6T/7$ . The entire cycle repeats starting from  $t = T$ .

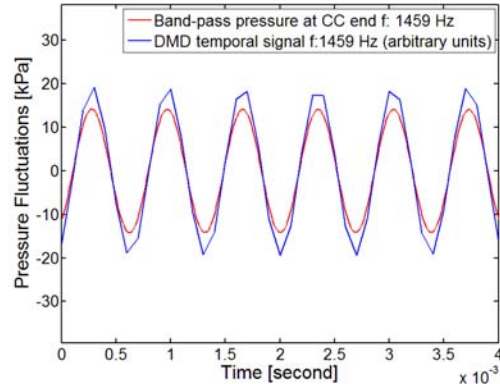


Figure 38: DMD temporal signal and band-pass filtered pressure measurement near the exit nozzle of the combustor at 1459 Hz

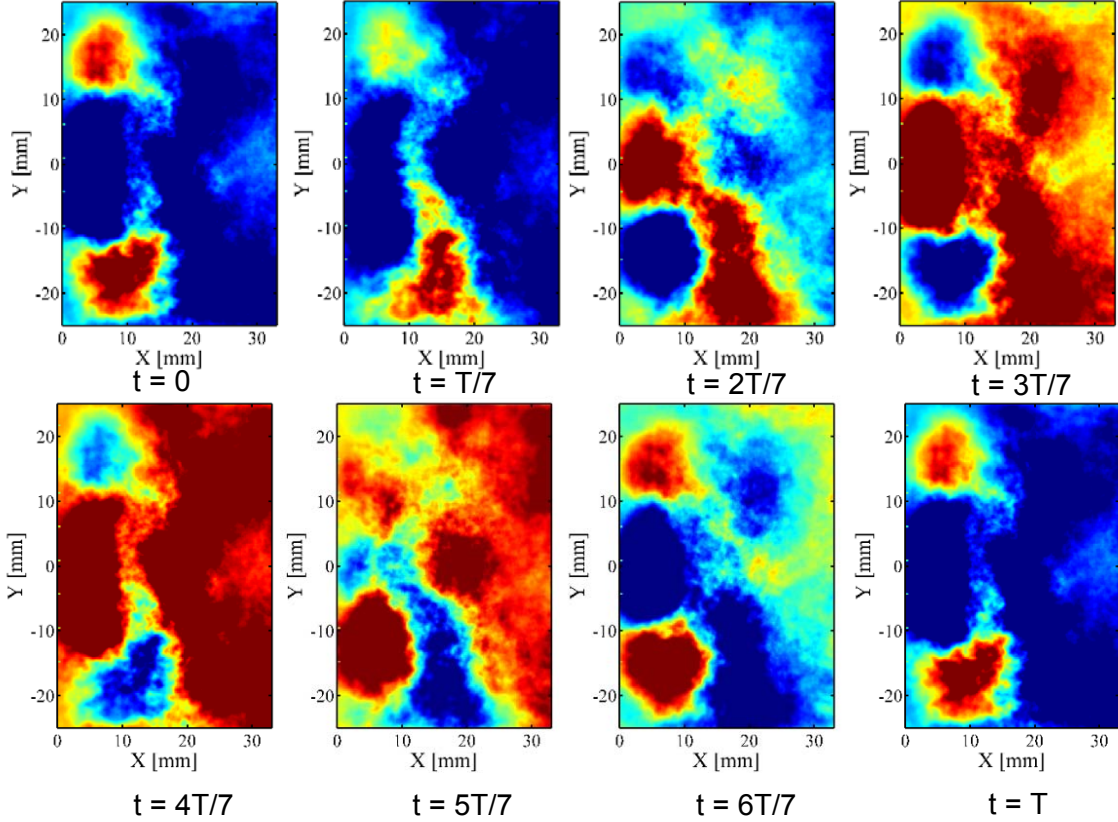


Figure 39: OH-PLIF images reconstructed from the DMD mode for an acoustic cycle at the 4L frequency of 1459 Hz

#### 3.4.1.5. *Analysis of raw corrected images:*

Corrected OH-PLIF images over a course of 2.4 ms (one cycle at the 4L mode is 4 frames) are shown in Figure 40 below. The images show a V-shaped flame that is anchored close to the dump plane of the combustor. The presence of multiple modes, from  $\sim 300$  Hz to 7 kHz makes tracking distinct flame structures from snapshot to snapshot difficult. As such tracking of flow structures without use of decomposition techniques such as DMD is difficult in such flows with large number of unsteady modes.

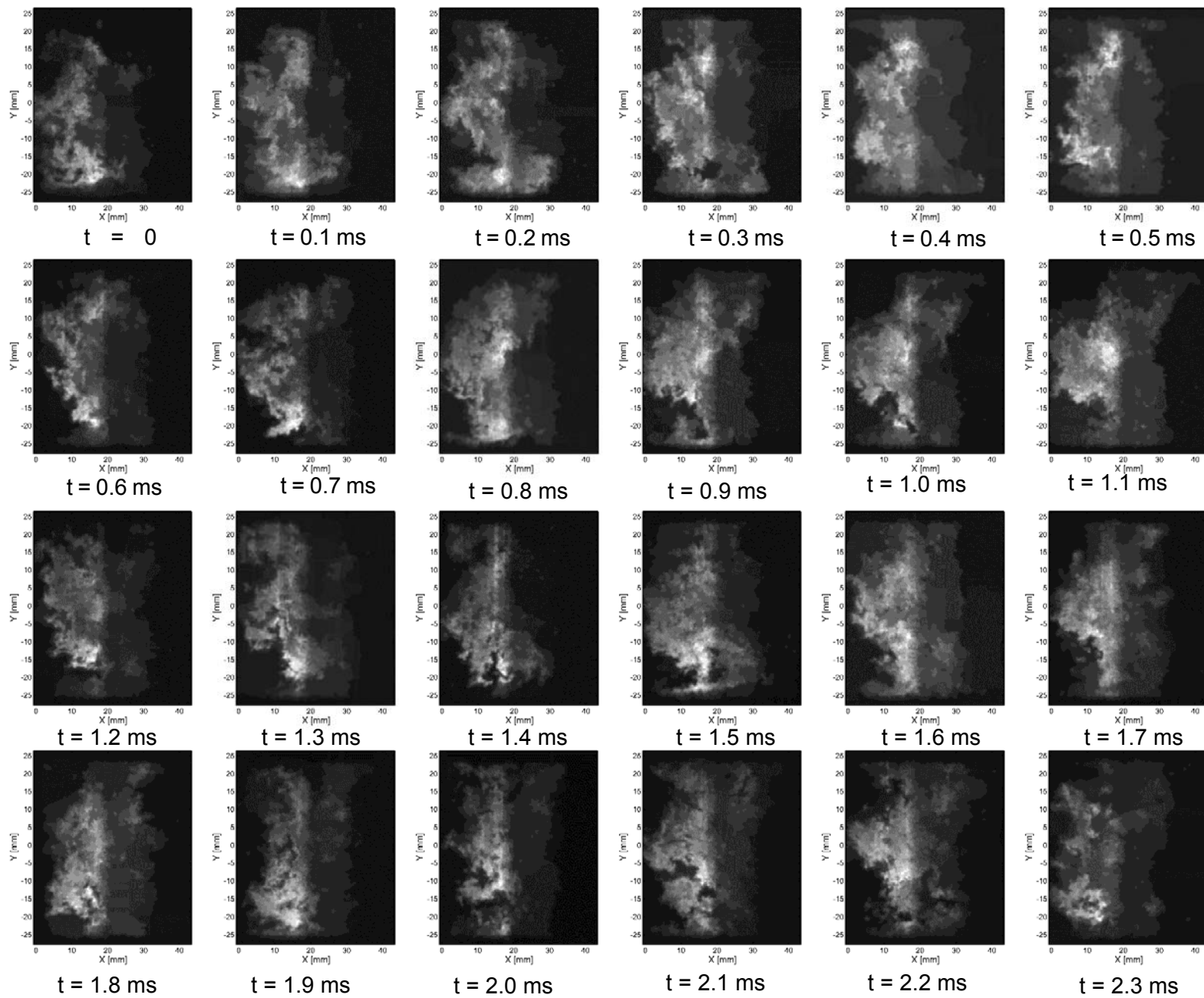


Figure 40: Instantaneous snapshots of the OH-PLIF signal over a 2.4 ms time period

### 3.4.2. PLIF 19: Low Equivalence Ratio Test-Case ( $\phi$ : 0.44)

#### 3.4.2.1. Pressure and OH-PLIF Time History

Figure 41 below shows the pressure time history for the low equivalence ratio (0.44) test case. Lean blow-out is observed in the combustor consistently at  $\phi$ : 0.43. The measured peak to peak pressure amplitude for this test was approximately 30-40 kPa. A magnified image over a shorter time period is shown in Fig. 41 (b). As seen from the figure, the pressure never reaches a limit cycle and continues to modulate in amplitude between 5 kPa to 30 KPa. This modulating behavior makes it challenging to analyze and find repeating patterns from the OH-PLIF measurements. Conversely, the highly modulating behavior allows a single test to capture combustion dynamics at a large spectrum of pressure fluctuation amplitudes. Fig. 41 (c) shows the computed flame front length in mm as a function of time. The flame front was extracted using a similar procedure described in the previous section for the high equivalence ratio case. The flame front length also shows large variations in time from almost a completely extinguished flame to a flame length of ~85 mm. This data is used to calculate the flame surface density.

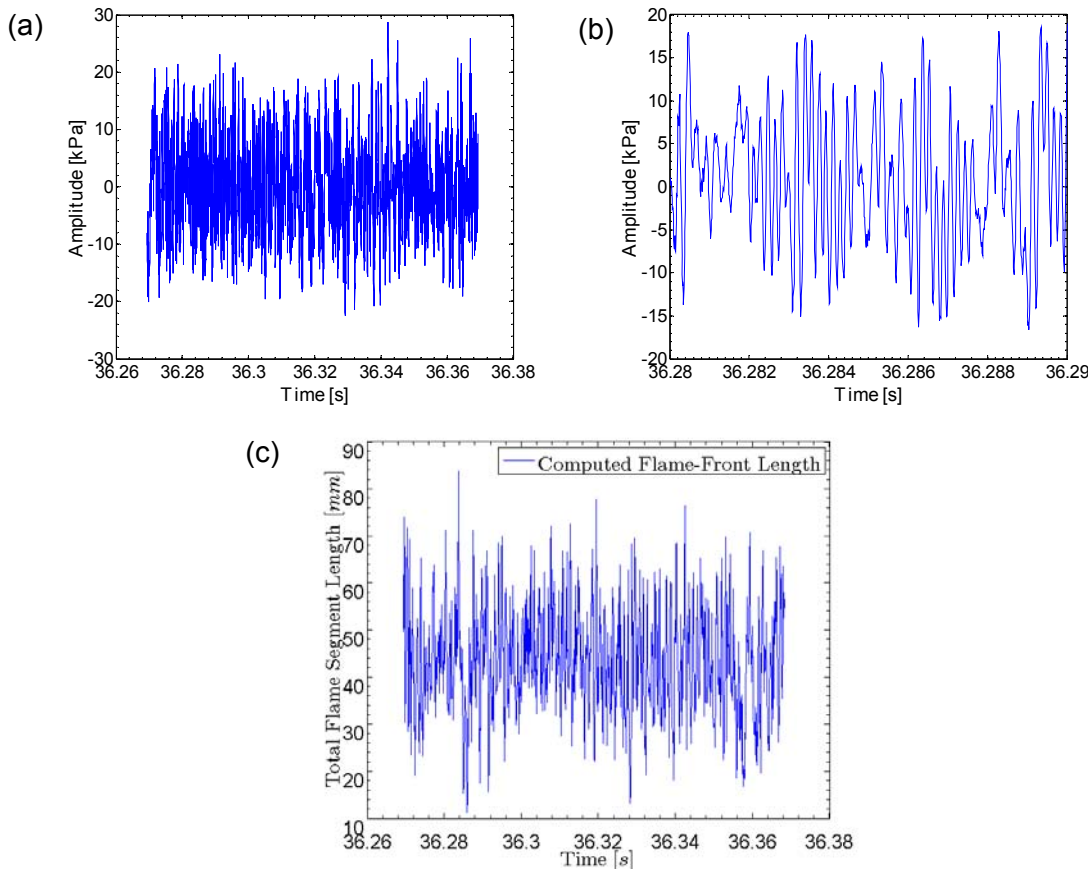


Figure 41: High pass filtered pressure measurements for PLIF 19 test case (a) over the time slice selected for image analysis (b) shorter time slice for better visualization of data (c) computed flame front length time history based on flame front extraction of corrected PLIF images

Figure 42 below shows the power spectral density of the pressure measurement and the flame front length for the low equivalence ratio flame. Contrary to the PSD spectrum with a large number of unsteady modes seen at a higher equivalence ratio, the PSD at an equivalence ratio of 0.44 shows low amplitude pressure modes from 1L – 5L with amplitudes that are comparable to each

other. The flame front spectrum indicates a dominant mode near the frequency of the 3L acoustic mode, with a few weaker modes. The power spectral density plots are plotted on a linear scale for clarity.

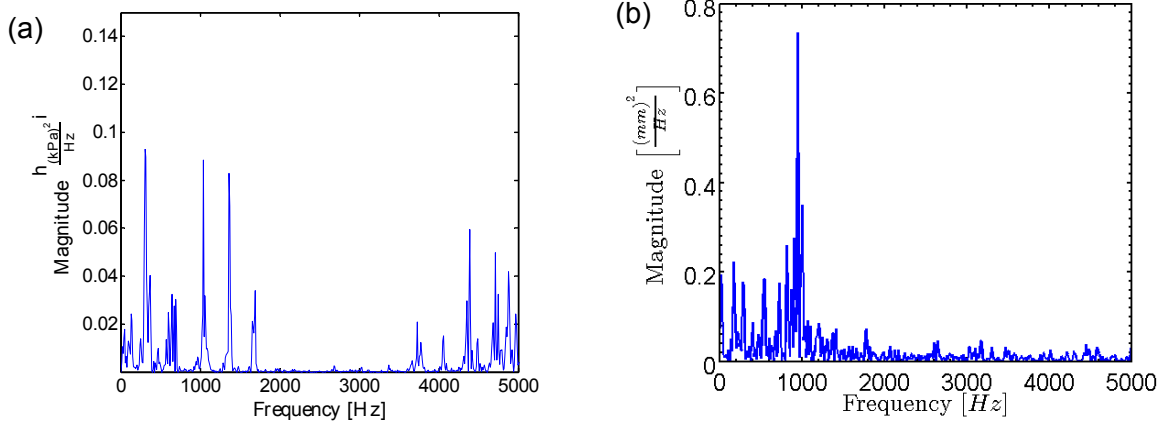


Figure 42: Power spectral density (a) high pass filtered pressure data (b) flame front length

### 3.4.2.2. Flame Front Extraction

Figure 43 below shows a representative snapshot of the OH-PLIF image at an equivalence ratio of 0.44. The image on the left is the corrected raw image, the one in the center is the enhanced image using the procedure laid out in the previous section for  $\phi = 0.6$  flame. The extracted flame-front (in black) overlaid on the corrected image is shown in the image on the right. The major difference between the images at the low equivalence ratio compared to the  $\phi = 0.6$  case is that the flame is lifted from the dump plane by as much as 10 mm. It retains the V-shape characteristic of a swirl stabilized flame but changes in time as the amplitude of the pressure fluctuations are modulated from low to high.

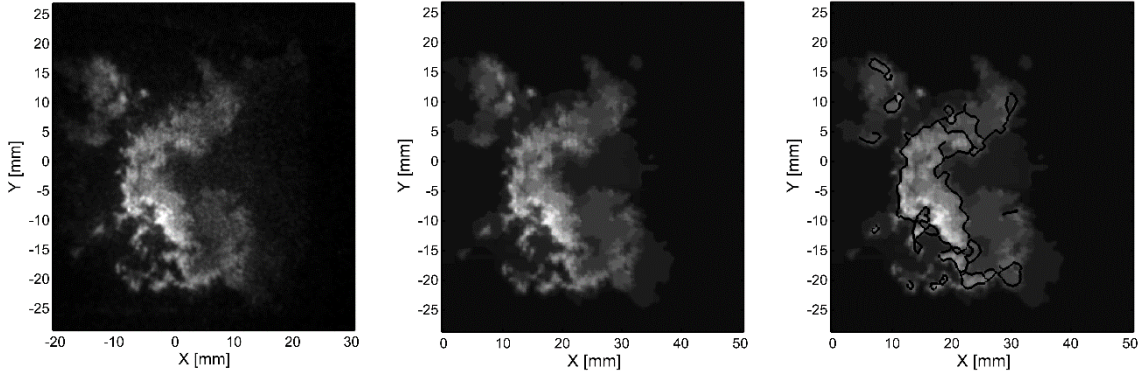


Figure 43: Instantaneous snapshots (a) corrected (b) enhanced and (c) overlaid with flame-front

### 3.4.2.3. Flame Surface Density

Figure 44 shows the flame surface density plot for the low equivalence ratio test case. The contour plot shows higher intensity regions further away from the dump plane centered within the lower intensity regions. The flame is symmetric about the axis of the combustor. The flame is also

spread across a longer area in the combustor extending approximately 35 mm from the dump plane. The spread was limited to approximately 20 mm for  $\phi = 0.6$ . This shows that at a lower equivalence ratio the flame shape is less compressed and the thermal power is distributed over a large area leading to weaker interactions with the combustor acoustics than at higher equivalence ratio where the flame is shorter and the thermal power is concentrated in a smaller volume.

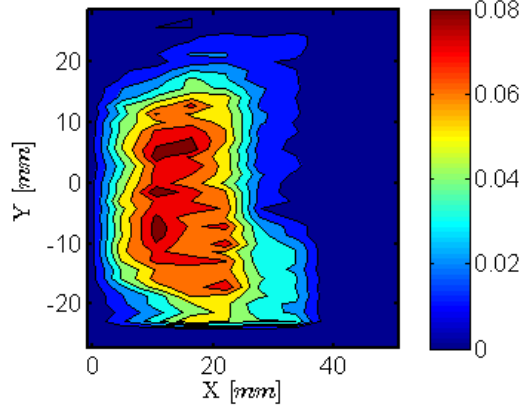


Figure 44: Flame Surface Density for the PLIF19 test case

#### 3.4.2.4. **Dynamic Mode Decomposition Analysis**

Figure 45 below shows the DMD energy spectrum for the PLIF spectrum. A strong peak is identified at a frequency of 1012 Hz which corresponds to the 3L acoustic mode in the combustor. The same frequency is identified in the pressure and the flame front spectra shown in *Figure 42*. A large number of peaks are present around the strong 3L frequency that show similar behavior to the 3L peak. These could also be artifacts of a 2D image of a 3D swirling flow. A high energy mode is present at a low frequency of  $\sim 20$  Hz which shows a slow longitudinal motion. Only the 3L mode is discussed in the following paragraphs.

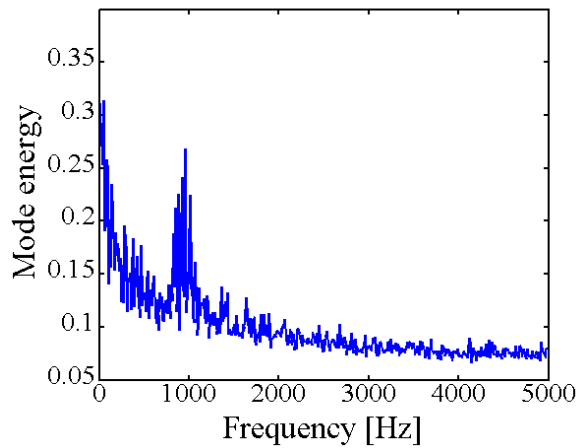


Figure 45: DMD energy spectrum for PLIF19

#### 3.4.2.4.1. Cycle Analysis:

Figure 46 below shows snapshots representing one acoustic cycle (0 to  $T$  s) starting from maximum of the OH signal at  $t = 0$  to a local minimum of the OH-signal at  $t = T/2$  and back to a maximum OH-signal at the end of the cycle for the 1012 Hz DMD spatial mode. The separation in time between snapshots is 1 ms. At  $t=0$ , the OH-signal is at its maximum and the high intensity regions are present near the periphery of the combustor. Two smaller lobes of lower intensity are concurrently present more than 10 mm removed from the dump plane near the central axis of the combustor inside the higher intensity regions. As the cycle progresses, these lobes are pushed out towards the periphery and higher intensity regions from the flame are transported towards the center of the combustor from  $t=2T/10$  through  $t=T/2$ . At  $t=T/2$ , the OH-signal is at its minimum near the dump plane. At this instant the local expansion draws more fuel and air into the combustor near the central axis of the combustor while the burnt gases travel back towards the periphery preheating the reactants. At  $t=9T/10$  the OH-signal is almost at its highest point again and the cycle is repeated thereafter.

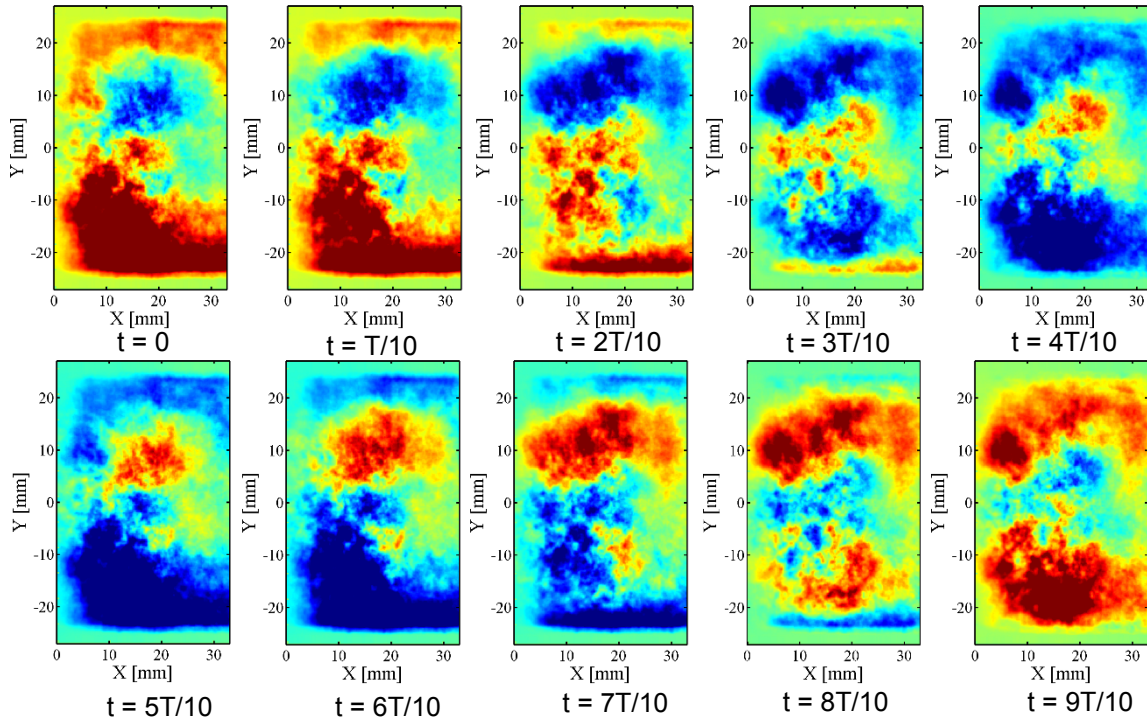


Figure 46: OH-PLIF images reconstructed from the DMD mode for an acoustic cycle at the 3L frequency of 1012 Hz

#### 3.4.2.5. Analysis of raw corrected images:

Corrected OH-PLIF images over a course of 2.4 ms are shown below in Figure 47. The significant modulation in the pressure fluctuation amplitude across the 1L-5L modes and consequently the flame shape makes it difficult to track a particular mode or structure through the image sequence. The main conclusion that can be drawn from the sequence of images is that the flame is always lifted off 5-10 mm from the dump plane of the combustor.

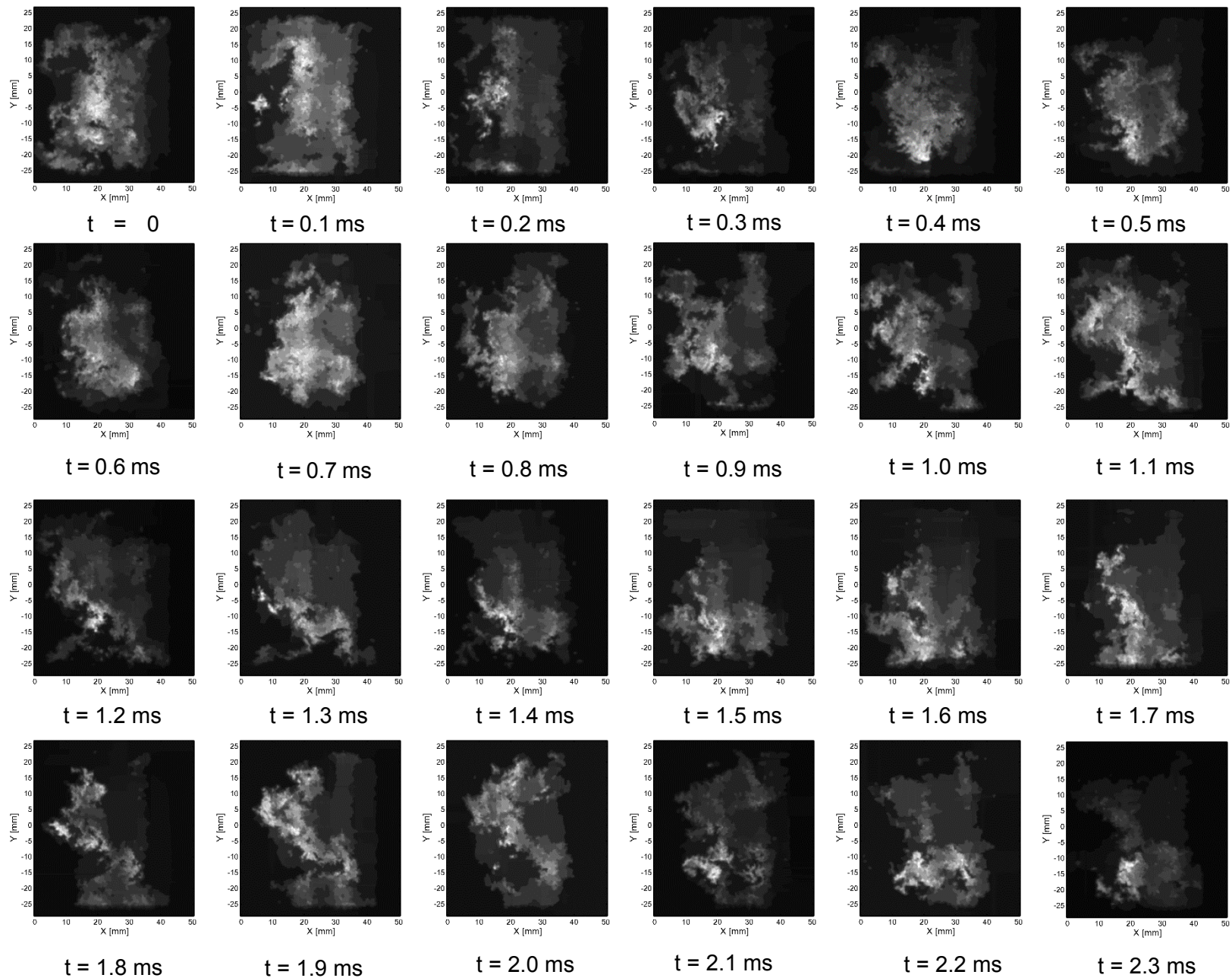


Figure 47: Instantaneous snapshots of the OH-PLIF signal over 2.4 ms

## 4. COMPUTATIONAL STUDY:

### 4.1. INLET STUDY

Dynamic flow response for different upstream inlet configurations were studied using a series of axisymmetric, cold flow simulations. The main objective was to design a simple and easily modeled inlet that introduced minimal unintended variables, e.g., entropy waves or other unsteadiness that could influence the combustion response. Four upstream inlet conditions were investigated: choked nozzle with a strong shock, choked nozzle with a subsonic diffuser, choked nozzle with a weak shock, and choked slot. These conditions were achieved by controlling the nozzle throat/slot area. The results of the study show that unsteadiness due to flow instabilities is unavoidable for all choked nozzle inlets, whereas the choked slot exhibits steady flow in spite of a large recirculation zone. Based on this result, the choked slot is recommended for the upstream inlet condition.

Results are summarized in Table 6. Distinct frequencies were observed in the mass flow and wall pressure fluctuations in the combustion chamber for all the nozzle inlet cases. It was concluded that the unsteadiness is unavoidable when a choked nozzle is employed as the upstream inlet condition. The choked slot case exhibited the most stable flow pattern as seen in Figure 48. The choked slot appears to be the best choice of inlet for the upstream configuration and is selected for the experimental studies.

Table 6 Summary of simulation results in terms of the inlet design

Case	Unsteadiness	Frequency (Hz)	Flow Features
Choked nozzle with a strong shock	Yes	9000	Oscillations with a shock train Lower pressure than chamber pressure by the supersonic flow until the center of air plenum
Choked nozzle with subsonic diffuser	Yes	6000	Typical hydrodynamic instabilities with large fluctuations of the mass flow rate and pressure
Choked nozzle with weak shock	Yes	6000	Typical hydrodynamic instabilities with small fluctuations of the mass flow rate and pressure
Choked slot	No	-	Large recirculation zone right after slots No unsteady motions in the air plenum

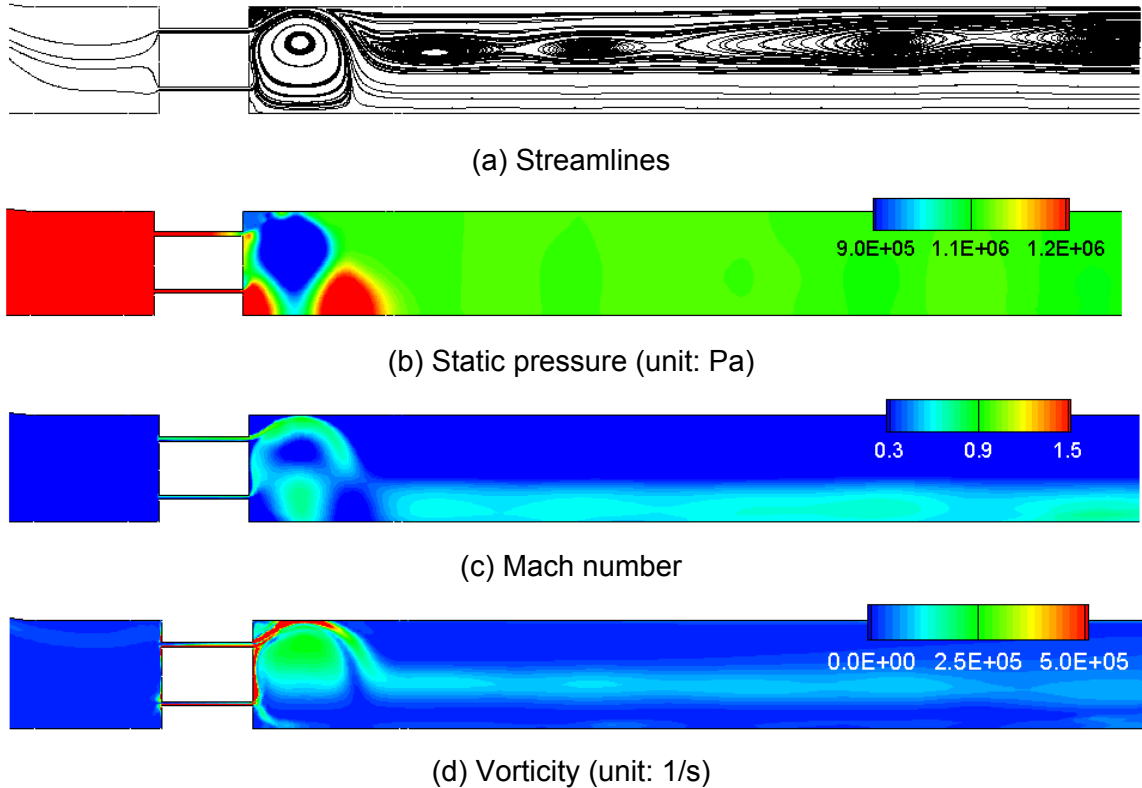


Figure 48 Upstream flow fields for the choked slot inlet

## 4.2. COMPUTATIONAL APPROACH

### 4.2.1. Computational Framework

The computational platform for the present simulations is an in-house code, GEMS (General Equation and Mesh Solver) [37-39]. GEMS is a fully unstructured, density-based finite volume solver with a second-order numerical scheme and an implicit, dual time procedure for time-accuracy. The capabilities of the code for capturing combustion dynamics and estimating instabilities have been successfully demonstrated for rocket engines combustors [40-42]. GEMS solves the Navier-Stokes equations in Detached Eddy Simulation (DES) mode along the continuity, energy and species equation described below.

$$\frac{\partial Q}{\partial t} + \nabla \cdot (F - F_v) = S \quad (1)$$

where the conservative variables,  $Q$ , inviscid and viscous flux vectors,  $F$  and  $F_v$ , and source term vector,  $S$ , are given by

$$Q = \begin{pmatrix} \rho \\ \rho \mathbf{Y} \\ \rho \mathbf{V} \\ \rho h^0 - p \\ \rho \mathbf{K} \end{pmatrix}, \quad F = \begin{pmatrix} \rho \mathbf{V}^T \\ \rho \mathbf{Y} \mathbf{V}^T \\ \rho \mathbf{V} \mathbf{V}^T + p \bar{\mathbf{I}} \\ \rho h^0 \mathbf{V}^T \\ \rho \mathbf{K} \mathbf{V}^T \end{pmatrix}, \quad F_v = \begin{pmatrix} 0 \\ \rho D \nabla \mathbf{Y} \\ -\bar{\tau} \\ \bar{\tau} \cdot \mathbf{V} - q \\ \mu_k \nabla \mathbf{K} \end{pmatrix} \quad \text{and} \quad S = \begin{pmatrix} 0 \\ \dot{\omega} \\ 0 \\ 0 \\ s_K \end{pmatrix} + S_L \quad (2)$$

The quantities;  $\rho$ ,  $\mathbf{V}$  and  $p$  represent the density, velocity vector and pressure, respectively;  $h^0$  is the stagnation enthalpy and  $\mathbf{Y}$  is a species mass fraction vector;  $\mathbf{K}$  represents the turbulence variable vector which includes turbulence kinetic energy and specific dissipation,  $k$  and  $w$ ; In the viscous flux,  $D$  is the molecular diffusion coefficient;  $\tau$  is the stress tensor and  $q$  is the heat flux;  $w$  and  $s_K$  are the reaction rate and sources of the turbulence transport equations, respectively. A pseudo-time term expressed in terms of the primitive variables,  $Q_p = [p \quad \mathbf{Y} \quad \mathbf{V} \quad T \quad \mathbf{K}]^T$  and a preconditioning matrix,  $\Gamma$ , is added to Eq. 3, so that the equation becomes:

$$\Gamma \frac{\partial Q_p}{\partial \tau} + \frac{\partial Q}{\partial \tau} + \nabla \cdot (F - F_v) = 0 \quad (3)$$

The matrix,  $\Gamma$  is chosen to control the artificial dissipation in the spatial discretization and the convergence of the pseudo-time iterations. The preconditioning matrix,  $\Gamma$  in the pseudo time term in Eq. (3), is defined by starting from the Jacobian of the conservative variables with respect to the primitive variables,  $\partial Q / \partial Q_p$ , as shown below:

$$\Gamma = \begin{pmatrix} \rho'_p & \rho_Y & 0 & \rho_T & 0 \\ \rho'_p \mathbf{Y} & \rho_Y \mathbf{Y} + \rho & 0 & \rho_T \mathbf{Y}^T & 0 \\ \rho'_p \mathbf{V} & \rho_Y \mathbf{V} & \rho \bar{\mathbf{I}} & \rho_T \mathbf{V}^T & 0 \\ \rho'_p h^0 - (1 - \rho h_p) & \rho_Y h^0 + \rho h_Y & \rho \mathbf{V}^T & \rho_T h^0 + \rho h_T & 0 \\ \rho'_p \mathbf{K} & \rho_Y \mathbf{K} & 0 & \rho_T \mathbf{K} & \rho \end{pmatrix} \quad (4)$$

where the primed quantities refer to scaled values that control the accuracy and efficiency of the pseudo-time iterations.

#### 4.2.2. Turbulence Model

The present simulations describe the large-scale, time-dependent turbulence motion by means of a Detached Eddy Simulation (DES) model [43, 44]. DES is a hybrid RANS/LES approach which combines the RANS model in the attached boundary layers with the LES method in the large separation and wake regions.

A DES model can be obtained from any RANS model and our DES formulation uses the  $k-\omega$  two-equation model with the appropriate modifications. Switching from RANS to LES mode is enabled by appropriately reducing the dissipation term in turbulent kinetic energy transport equations. Specifically, the DES model replaces the length scale with the minimum of the length scale defined in turbulence model for RANS and maximum spacing of the local grid as:

$$l_{DES} = \min(l_{k-\omega}, C_{DES}\delta) \quad (5)$$

where  $\delta = \max(\Delta x, \Delta y, \Delta z)$  represents the maximum grid spacing in any direction and  $C_{DES}$  is a model constant and set equal to 0.78 as recommended by Travin et al.[45];  $l_{k-\omega}$  is the length scale of Wilcox's [46]  $k-\omega$  two equation model for the turbulence closure in RANS and it is defined as

$$l_{k-\omega} = \frac{k^{1/2}}{\beta^* \omega} \quad (6)$$

where,  $\beta^*$  is a model constant. This definition of the length scale by Eq. (6) ensures that the RANS mode is utilized near the wall surface in which the high grid aspect ratio is typically expected. Finally, the dissipation term in the transport equation of the turbulence kinetic energy is replaced by

$$\beta^* \rho k_w = \frac{\rho k^{3/2}}{l_{DES}} \quad (7)$$

This modification ensures that the resulting sub-grid model reduces to a Smagorinsky-like model at equilibrium.

#### 4.2.3. Combustion Model

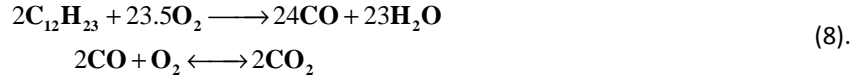
The species equations are solved directly and turbulence transport in the species equations is modeled using the classical gradient model with a constant Schmidt number. Laminar finite rate chemistry model is used to evaluate the reaction rate. Although flamelets and transported-FMDM models are popular in unsteady LES simulations, their capabilities for predicting combustion/acoustic interaction problems are not well-established, particularly, because these models are based upon constant pressure flame assumptions. Two sets of chemical kinetics have been tried to assess the effects of chemistry on combustion instability predictions.

For the first set of chemical kinetics, the six chemical species considered for the propellant combination in the LDI combustor are  $C_{12}H_{23}$ ,  $O_2$ ,  $CO_2$ ,  $H_2O$ ,  $CO$  and  $N_2$ , which considers the fuel as  $C_{12}H_{23}$  to approximate the experimental Jet-A fuel. A simplified two-step, five species global reduced mechanism [47] has been incorporated in the present study,



**IMPORTANT:** it should be notified that there is a mistake with regards to an unbalance in the O element in the equation above. The two-step chemistry here has been used in most of the LDI computation studies so far and the effects of the O element unbalance are being evaluated with

the corrected version of chemistry as baseline cases. Relevant results can be updated later once the simulations are done with corrected chemistry,



The second set of chemical kinetics consists of 18 step reactions including 15 species with  $\text{C}_{11}\text{H}_{21}$  as a surrogate of Jet-A fuel [48], which provides a more detailed description of the chemical reactions,

NO.	Reaction
1	$\text{C}_{11}\text{H}_{21} + \text{O}_2 = 11\text{CH} + 10\text{H} + \text{O}_2 + \text{G}/0.8, 0.8$
2	$\text{CH} + \text{O}_2 = \text{CO} + \text{OH} + \text{G}/1.0, 1.0$
3	$\text{CH} + \text{O} = \text{CO} + \text{H} + \text{G}/1.0, 1.0$
4	$\text{H}_2 + \text{O}_2 = \text{H}_2\text{O} + \text{O}$
5	$\text{H}_2 + \text{O} = \text{H} + \text{OH}$
6	$\text{H} + \text{O}_2 = \text{O} + \text{OH}$
7	$\text{H}_2\text{O} + \text{O}_2 = 2\text{O} + \text{H}_2\text{O}$
8	$\text{CO} + \text{OH} = \text{CO}_2 + \text{H}$
9	$\text{CO} + \text{H}_2\text{O} = \text{CO}_2 + \text{H}_2$
10	$\text{CO} + \text{H}_2 + \text{O}_2 = \text{CO}_2 + \text{H}_2\text{O}$
11	$\text{N} + \text{NO} = \text{N}_2 + \text{O}$
12	$\text{N} + \text{O}_2 = \text{NO} + \text{O}$
13	$\text{N} + \text{OH} = \text{NO} + \text{H}$
14	$\text{N} + \text{N} + \text{M} = \text{N}_2 + \text{M}$
15	$\text{H} + \text{N}_2\text{O} = \text{N}_2 + \text{OH}$
16	$\text{N}_2 + \text{O}_2 + \text{O} = \text{N}_2\text{O} + \text{O}_2$
17	$\text{N}_2\text{O} + \text{O} = 2\text{NO}$
18	$\text{N}_2\text{O} + \text{M} = \text{N}_2 + \text{O} + \text{M}$

#### 4.2.4. Fuel Spray Model

Modeling of direct injection sprays for gas turbine engines has been developed for combustion dynamics problems. This method combines sub-models for atomizing, vaporizing and reacting sprays. Key physical events considered in the present model include free-surface jet in the atomizer, primary and secondary breakup, droplet vaporization, mixing and burning. The models are implemented within an Lagrangian-Eulerian framework, where the droplet phase is described by Lagrangian dynamics and the vaporized fuel is input as a source term along with associated momentum and energy terms in the Eulerian gas-phase equations.

##### Lagrangian-Eulerian Approach

The Lagrangian formulation for the liquid particle motion is expressed as a set of ordinary differential equations for the Lagrangian solution variables,  $Q_L$ , as:

$$\frac{dQ_L}{dt} = \frac{d}{dt} \begin{pmatrix} \mathbf{X} \\ \mathbf{U} \\ T_l \\ m_l \\ r \end{pmatrix} = \begin{pmatrix} \mathbf{U} \\ F_D(\mathbf{V} - \mathbf{U}) \\ \dot{m}_v [c_p(T_g - T_l) - L_v] / m_l C_l \\ -\dot{m}_v \\ -\dot{m}_v / (4\pi r^2) \end{pmatrix} \quad (9)$$

where  $\mathbf{X}$ ,  $\mathbf{U}$ ,  $T_l$ ,  $m_l$  and  $r$  are the components of the Lagrangian solution vector and these variables represent the position and velocity vector, temperature, mass and radius for the liquid particle, respectively. The first and second rows represent the motion of particle drops in which only the drag is considered as an external force. In the source of second row,  $F_D$  is a drag parameter accounting for  $F_D = \frac{3}{8} \frac{C_D}{r} \frac{\rho_g}{\rho_l} |\mathbf{U} - \mathbf{V}|$  in which  $\mathbf{V}$  is the carrier gas velocity vector and the drag coefficient follows Putnam's formulation [49] based on the spherical drop assumption.

$$C_D = \begin{cases} 0.44 & \text{Re} < 1000 \\ \frac{24}{\text{Re}} \left( 1 + \frac{1}{6} \text{Re}^{2/3} \right) & \text{Re} > 1000 \end{cases} \quad (10)$$

where Reynolds number,  $\text{Re}$ , is defined as  $\frac{\rho_g d}{\mu_g}$ . The third row in Eq. (9) represents the energy equation for the liquid particle. This equation assumes the uniform temperature inside the liquid particle. The source term consists of the net sensible enthalpy transfer,  $c_p(T_g - T_l)$  and the latent heat of vaporization,  $L_v$ , and  $m_l C_l$  represents the heat capacity of the liquid particle. The fourth row accounts for the mass balance during vaporization. The corresponding source term is the vaporization rate,  $\dot{m}_v$  which is evaluated by means of the classical D<sup>2</sup>-law:

$$\dot{m}_v = -2\pi r \rho_g D_s \text{Sh} \ln(1 + B_M) \quad (11)$$

where  $D_s$  is a diffusion coefficient at the liquid surface and Sh is a Sherwood number;  $B_M$  is the Spalding mass transfer number given by

$$B_M = \frac{Y_{F,s} - Y_{F,\infty}}{1 - Y_{F,s}} \quad (12)$$

where  $Y_F$  is the fuel species, subscripts  $s$  and  $\infty$  indicate the surface and far field, respectively. The last row accounts for the particle radius reduction due to the vaporization. The set of Lagrangian phase equations, Eq.(9), is integrated explicitly and the Lagrangian time step is determined by consideration of the time scales of the particle lifetime, atomization initiation time and Eulerian time step, etc. All other physical properties of the liquid particle are updated every time step as well.

Lagrangian phase equations are coupled with the Eulerian phase through the source term vector,  $S$ , in Eq. (2) to account for the influence of liquid phase physics on the gas phase. Mass, chemical species, momentum and energy transfer from the Lagrangian phase are served as the source of Eulerian phase.

$$S_L = \frac{d}{dt} \begin{pmatrix} \rho \\ \rho\mathbf{Y} \\ \rho\mathbf{V} \\ \rho h^0 - p \\ \rho\mathbf{K} \end{pmatrix} = \begin{pmatrix} \sum_N n\dot{m}_v \\ \sum_N n\dot{m}_v \\ \sum_N n(\dot{m}_v \mathbf{U} - m_l \dot{\mathbf{U}}) \\ \sum_N n(\dot{m}_v h_v - \dot{m}_v Q_d) \\ 0 \end{pmatrix} \quad (13)$$

where subscript  $N$  and  $n$  represent the number of parcel and the number of drops in an individual parcel respectively.

### *Injection and Atomization Model*

Details of the present fuel spray modeling implementation can be found in Yoon et al. [25, 50]. There are three major models for the description of spray atomization: atomizer free surface flow, primary and secondary atomization models. The first model describes the atomizer free surface flow. Independent calculation of the free surface internal flow in the atomizer provides the spray injection conditions of the Lagrangian spray particles. Ashraf and Jog's numerical model [51] is employed for the present study. This model directly solves the two phase flow using the Eulerian Volume-Of-Fluid (VOF) Method and provides the spray angle, liquid sheet thickness and velocity. This information is delivered to the second model, for primary atomization. The primary atomization is described by the linear stability analysis of the liquid sheet proposed by Senecal et al.[52] Using the liquid sheet thickness and velocity, the most unstable wavelength and maximum growth rate are determined by dispersion relation derived from linear stability theory, and ligament and drop sizes produced from the liquid sheet are then calculated. Lagrangian drops produced by the primary atomization are defined at the exit plane of the atomizer and then undergo the secondary atomization process, which is represented by the third model. During secondary atomization, the drops may be broken up by several kinds of modes. The secondary atomization model developed in the present study covers the full Weber number range typically encountered in gas turbine combustors. Depending on the Weber number range, appropriate secondary atomization models are applied that include the Taylor Analogy Breakup (TAB) [53], Kelvin Helmholtz (KH) and Rayleigh-Taylor (RT) models [54-56].

For  $11 < \text{We} < 40$ , the TAB model is applied. This model was proposed by O'Rourke and Amsden [53] and is based on the classical analogy between an oscillating and distorting droplet and a spring mass system. It presumes that the external, restoring and damping forces in a spring mass system correspond to the drag, surface tension and viscous forces in a drop oscillation and distortion process.

$$\frac{d^2 y}{dt^2} = \frac{C_f}{C_b} \frac{\rho_g}{\rho_l} \frac{u^2}{r^2} - \frac{C_k \sigma}{\rho_l r^3} y - \frac{C_d \mu_l}{\rho_l r^2} \frac{dy}{dt} \quad \text{where } y = \frac{x}{C_b r}$$

breakup occurs when  $y > 1$

$$y(t) = \text{We}_c + e^{-(t/t_d)} \left[ (y_0 - \text{We}_c) \cos(\omega t) + \frac{1}{\omega} \left( \frac{dy_0}{dt} + \frac{y_0 - \text{We}_c}{t_d} \right) \sin(\omega t) \right] \quad (14)$$

$$\text{where } \text{We}_c = \frac{C_f}{C_k C_b} \text{We} \quad \text{and} \quad \omega = \sqrt{\frac{C_k \sigma}{\rho_l r^3} - \left( \frac{C_d}{2\mu_l \rho_l r^2} \right)^2}$$

$$\text{where } \text{We}_c = \frac{C_f}{C_k C_b} \text{We} \quad \text{and} \quad \omega = \sqrt{\frac{C_k \sigma}{\rho_l r^3} - \left( \frac{1}{3} \right)^2}$$

The recommended model constants from the literature are  $C_b = 0.5$ ,  $C_k = 8.0$ ,  $C_d = 5.0$  and  $C_f = 1/3$ .

For  $40 < \text{We} < 350$ , the KH model is used. It was originally formulated by Reitz [54] and is based on the Kelvin-Helmholtz (KH) instability phenomenon. Here, the results of the linearized stability analysis are directly used in determining the important parameters in the atomization process. For easier use of the linear stability analysis results, the maximum growth rate,  $\Omega$ , and corresponding wavelength,  $\Lambda$ , of the Kelvin-Helmholtz instability mode are expressed by curve-fits in terms of non-dimensional numbers as,

$$\Omega_{\text{KH}} \left[ \frac{\rho_l a^3}{\sigma} \right]^{0.5} = \frac{(0.34 + 0.38 \text{We}_g^2)}{(1 + \text{Oh})(1 + 1.4 \text{Ta}^{0.6})} \quad (15)$$

$$\frac{\Lambda_{\text{KH}}}{a} = 9.02 \frac{(1 + 0.45 \text{Oh}^{0.5})(1 + 0.4 \text{Ta}^{0.7})}{(1 + 0.87 \text{We}_g^{1.67})^{0.6}} \quad (16)$$

where  $\text{We}_g$  is the Weber number for the gas phase,  $\text{We}_g = \frac{\rho |\mathbf{U} - \mathbf{V}|^2 d}{\sigma}$ ,  $\text{Oh}$  is the Ohnesorge number,  $\text{Oh} = \nu_1 \sqrt{\frac{\rho_l}{\sigma a}}$  and  $\text{Ta}$  is the Taylor parameter,  $\text{Ta} = \text{Oh} \sqrt{\text{We}_g}$ . The liquid breakup is modeled by adding new child parcels and their size is determined by

$$r_c = B_0 \Lambda_{\text{KH}} \quad (17)$$

where  $B_0$  is a model constant and set equal to 0.61. Simultaneously, the parent drop size is reduced by

$$\frac{da}{dt} = -\frac{(a - r)}{\tau} \quad (18)$$

where  $\tau$  is a time constant and determined from

$$\tau = 3.726 B_1 a / \Lambda_{\text{KH}} \Omega_{\text{KH}} \quad (19)$$

Here the drop size constant  $B_0 = 0.61$  and breakup time constant  $B_1 = 10.0$  as recommended by Reitz [57]. Child parcels are released when the stripped mass removed from the parent parcel exceeds a few percent of the average injected parcel mass.

Lastly, for high Weber number ( $\text{We} > 350$ ) the Rayleigh-Taylor (RT) [54] model is applied with KH model. RT model is based on drop acceleration normal to the interface between two fluids that can drive the instability. Taking the external force acting on the droplet to be given by the aerodynamic drag, the acceleration can be expressed by dividing the drag force by the droplet mass:

$$a = \frac{3}{8} C_D \frac{\rho_g u_r^2}{\rho_l r} \quad (20)$$

Based on the linearized instability analysis by Chang, the wavelength and frequency of the fastest growing waves are determined as:

$$\Lambda_{\text{RT}} = 2\pi \sqrt{\frac{3\sigma}{a\rho_l}} \quad (21)$$

$$\Omega_{RT} = \sqrt{\frac{2a}{3}} \left[ \frac{a\rho_i}{3\sigma} \right]^{1/4} \quad (22)$$

The droplet breakup is allowed to occur when the RT wavelength,  $\Lambda_{RT}$ , is smaller than the droplet diameter until the RT breakup time,  $\tau_{RT} = 1/\Omega_{RT}$ .

#### 4.2.5. Computational Geometry and Operating Conditions

The geometry of the single LDI element used in the simulation is shown in Fig. 49, which was the same as the one used in the companion experiments. The choked inlet slots (Detail A) and an exit nozzle (Detail C) are used to guarantee acoustically reflecting boundary conditions to sustain combustion instabilities in both the simulations and the experiments. Fuel injector (Detail B) sits in the converging-diverging section connecting the air plenum and combustor with the swirler. Preheated air comes through the choked inlet slots and enters the converging-diverging section through the air plenum. Hot air mixes with fuel spray from the fuel injector near the swirler and reacts in the combustor. The length of the air plenum and combustor are adjusted so that it supports a 3/8 acoustic wave in the air plenum and 1/2 wave in the combustor. This configuration has been reported to show lowest pressure oscillations in the experimental parametric studies by Gejji et al. [58]. Operating conditions for the simulations in this section are focused at the high inlet air temperature ( $T_{air} = 800K$ ) and high equivalence ratio ( $\phi = 0.6$ ) case with the fuel nozzle located at the venturi throat. As shown in Figure 50, simulations do not match measurements for this case, therefore this condition will be used to assess the effects of different spray models to see if any improvement in the comparison can be made.

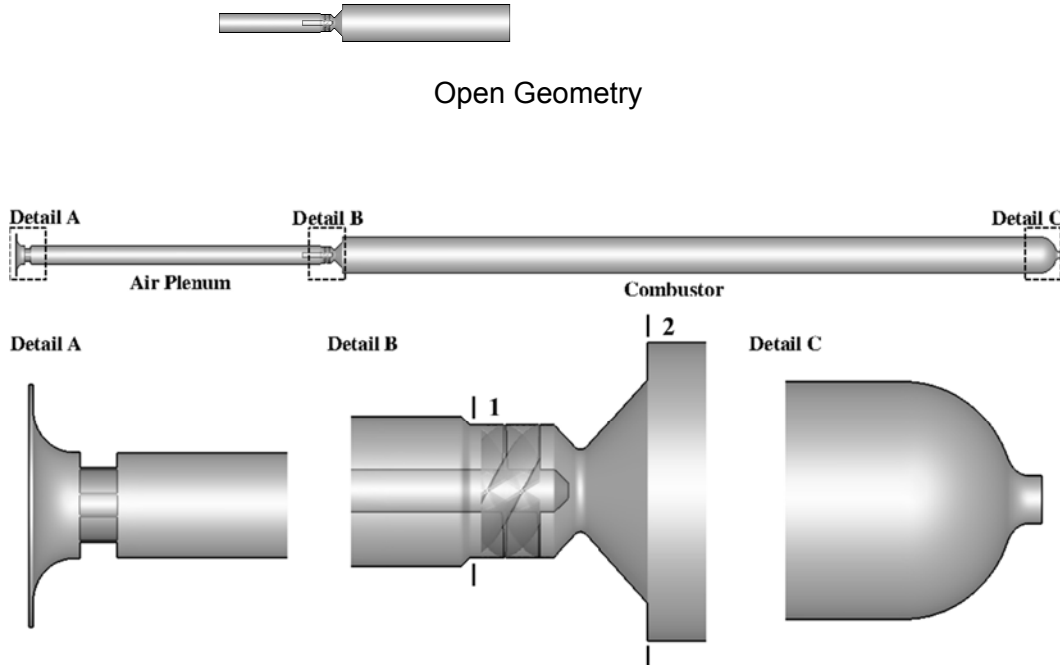


Figure 49. Computational geometry of LDI gas turbine combustor.

#### 4.3. PRESSURE COMPARISON BETWEEN EXPERIMENT AND SIMULATION

Figures 50 and 51 below show the comparisons of pressure signal between measurement and prediction at high and low equivalence ratios, respectively. The pressure signals have been high-

pass filtered and taken at the same location near the combustor head section for both experiment and simulation. The simulations are performed with the Weber-number-adaptive spray model.

For the high equivalence ratio (Fig. 50), a peak-to-peak pressure fluctuation amplitude around 0.1 MPa can be seen in both experiment and simulation with the fuel nozzle located 2.66 mm upstream of the venturi throat. Also, the 4L and 8L acoustic modes can be clearly identified in the power spectral density plots. However, the multiple modes between 6 and 8 kHz (identified in most test configurations) cannot be fully captured in the simulations. When the fuel nozzle is put at the venturi throat, the simulation severely under-predicts the pressure fluctuation amplitude. The experimental measurements show higher pressure amplitude when the fuel nozzle is at the venturi throat than when it is located upstream of the venture throat, but the computational results show the opposite trend.

For the low equivalence ratio case (Fig. 51), lower peak-to-peak pressure amplitude (around 30 to 40 kPa) can be observed in both experiment and simulation. The 1L acoustic mode is more distinguishable in the PSD plots than in the high equivalence ratio case. The dominant acoustic modes have been shifted to higher 5L and 6L acoustic modes. In the experiment, an even distribution in the PSD can be observed for lower frequencies (1L to 4L), while in the simulation, a collapse in PSD of 2L to 4L modes can be found. The simulation under-predicts both the PSD and the frequencies of responses higher than 6kHz while, in the experiment, the high frequency peak lies around 7kHz and has comparable PSD as 1L.

Overall, the simulations predict reasonable pressure amplitudes and captures the dominant acoustic frequencies measured in the experiments for both high and low equivalence ratios when fuel nozzle is upstream of the throat, but it does not capture the high frequency modes between 6 and 8 kHz. Larger disagreement between experiment and simulation is observed when fuel nozzle at the throat. It is speculated that the We-adaptive models may be overly sensitive to the dynamics arising from placing the fuel nozzle at the throat.

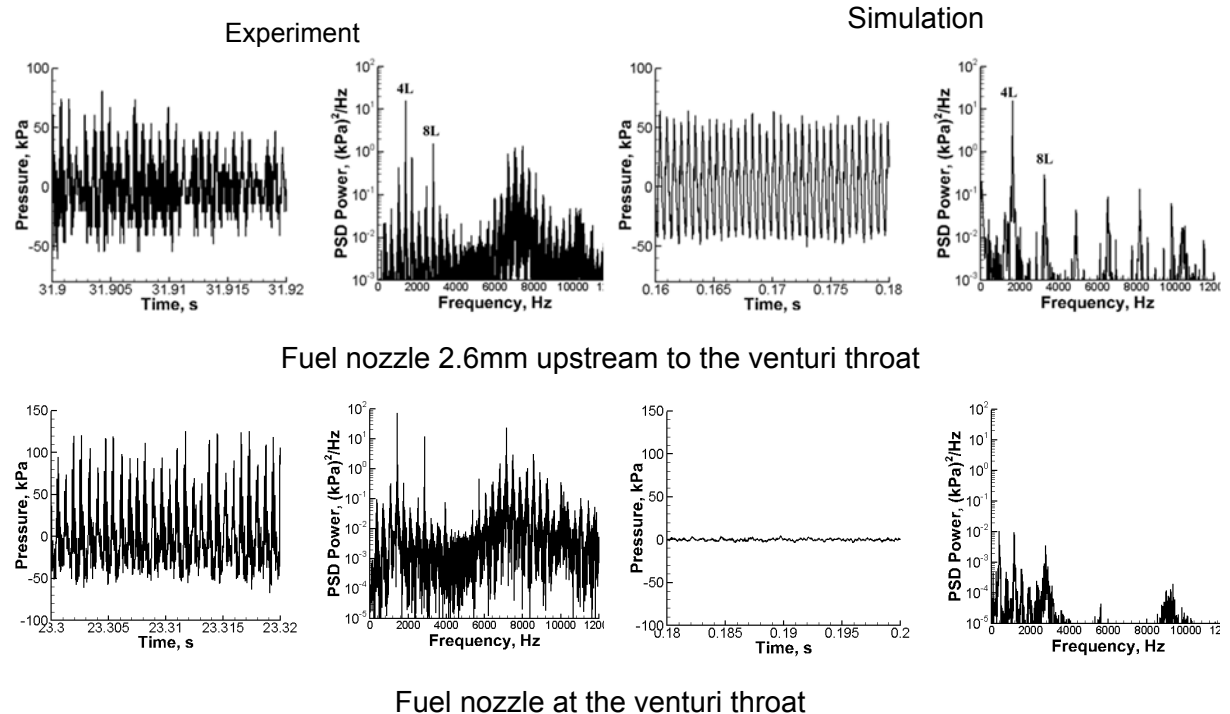


Figure 50. Experiment and simulation comparison for  $T_{air} = 800K$  and  $\Phi = 0.6$ .

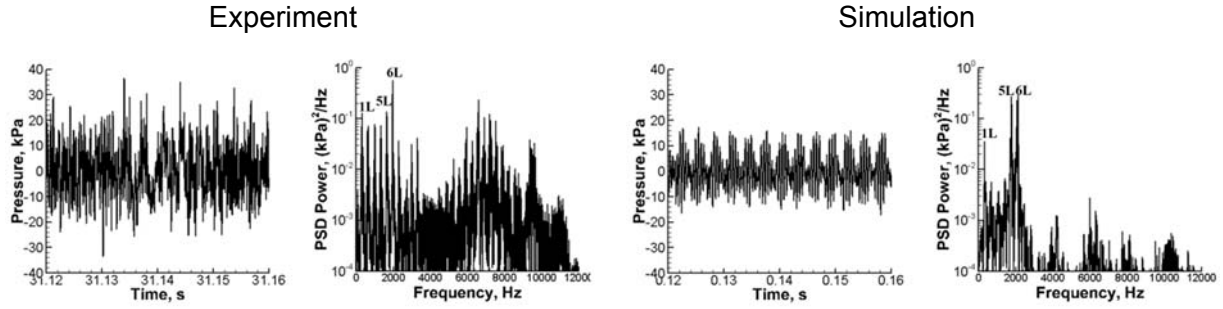


Figure 51. Experiment and simulation comparison for  $T_{air} = 800K$  and  $\phi = 0.36$  with fuel nozzle upstream to the venturi throat.

#### 4.4. EFFECT OF FUEL SPRAY MODELING IN COMBUSTION INSTABILITY PREDICTIONS

The efforts in fuel spray modeling are summarized in Table 7 for LDI simulations with the fuel nozzle located at the venturi throat. It was reported in Ref. [21] that simulations with the hybrid model matched the experimental pressure measurements (dominant frequencies and amplitudes) reasonably well when the fuel nozzle was located upstream of the venturi throat, but the pressure amplitude was severely under-predicted when the fuel nozzle was located at the throat. As shown in Fig. 50, the experimental measurements show higher pressure amplitude when the fuel nozzle is at the venturi throat than when it is located upstream of the venturi throat, but the computational results show the opposite trend. Detailed investigations of underlying physical phenomena leading to combustion instabilities were further conducted by Huang et al. [20] for the low equivalence ratio case ( $\phi = 0.36$ ) which showed good agreement with experimental data.

Table 7 Summary of fuel spray modeling effects on predicting combustion instability (fuel nozzle is located at the venturi throat).

Operating Conditions	Case Name	Total peak-to-peak pressure amplitude (%)	Dominant Acoustic Mode	Secondary Atomization Model
$T_{air} = 800K$ , $\phi = 0.6$	Experiment	15	4L	NA
$T_{air} = 750K$ , $\phi = 0.6$	Case 1: Log Normal Distributed Drop Injection	11	1L	No
	Case 2: Single Drop Injection	7	2L	KH
	Case 3: Hollow Cone Injection	0.24	4L	KH
$T_{air} = 800K$ , $\phi = 0.6$	Case 4: LISA + Hybrid Secondary Breakup Model	0.5	3L	Hybrid TAB/KH/RT

Poor agreement between experiment and simulation is seen for the case with the fuel nozzle at the throat. A further and careful assessment is made to evaluate the fuel spray modeling effects

on the combustion instability predictions. Simulation results are compared between cases with different fuel nozzle locations to obtain some basic understanding of potential modeling issues that exist in the current simulations. As shown in Fig. 50, the simulations with the fuel nozzle upstream of the throat provide better agreement with the experimental measurements and, therefore, it is useful to compare this case with the one where the fuel nozzle is at throat to help understand the possible modeling issues. The comparisons are focused on the heat release distribution, axial velocity and spray characteristics as shown in Fig. 52. The background contours are heat release rate (left) and axial velocity (right). The drop radius is represented by the spray drop size in the figure and the colors on the spray drops represent the magnitude of temperature (left) and Weber number (right). One black iso-line of stoichiometric gaseous fuel mass fraction indicates the distribution of vaporized gaseous fuel.

In Fig. 52, it can be observed that there are more spray drops left in the venturi when the fuel nozzle is located at the throat. Many small-size drops are observed between the middle of the diverging section and the dump plane, indicating a slow breakup process and vaporization, which can be attributed to the insufficient spray drop breakup described by the models. Therefore, TAB and KH secondary breakup models are studied individually first by tuning the model constants to reduce the drop size after secondary breakup and also to accelerate the breakup process.

It is also noted in Fig. 52 that the Weber number of drops is higher with the fuel nozzle located upstream of the throat and the fuel spray models described in part 4.2.4 (primary: LISA and secondary: TAB/KH/RT) are highly dependent on Weber number. Because of this sensitivity to We, a small discrepancy may cause a large deviation in the spray predictions, and consequently affect the production of gaseous fuel and hence heat release distribution. Instead of applying a model for primary breakup, we look to specify a spray drop distribution that can be tuned to obtain reasonable combustion instability predictions.

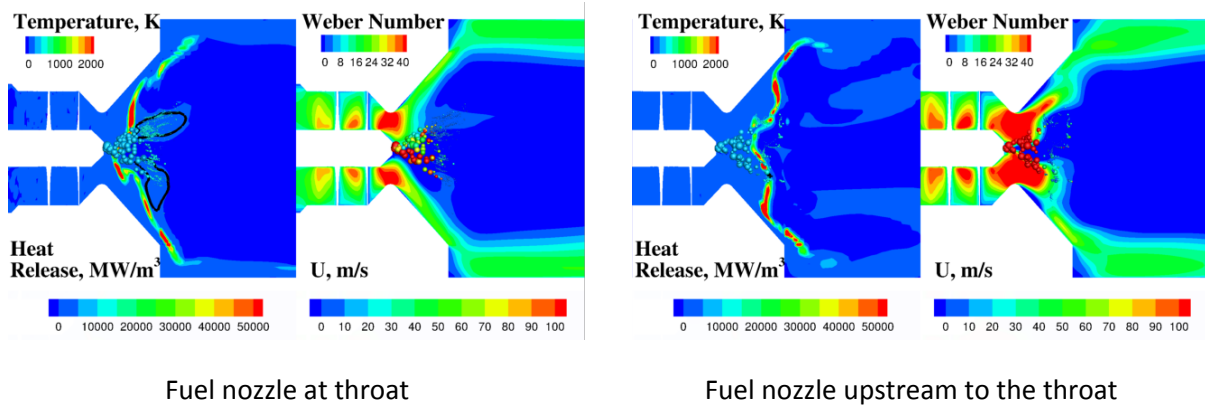


Figure 52. Instantaneous heat release distribution, axial velocity and spray characteristics comparisons between simulations with fuel nozzle at throat and upstream to the throat.

#### 4.4.1. Effects of Secondary Breakup Model

Both TAB and KH/RT models are applied and tuned individually to systematically assess the effects of secondary breakup model. The discussion is mainly focused on the tuning of KH/RT model.

##### 4.4.1.1. Tuning of TAB model

Due to the fact that the TAB model has five independent controlling model constants, its tuning is questionable. At any rate, in this study only one constant  $C_f$  is selected for simplicity. In Eq. (14), by increasing the value of  $C_f$ , the value of  $We_C$  is increased, which increases the possibility

of TAB-type of breakup process to occur. The tuning effects of the TAB model on the pressure signal predictions are summarized in Table 8 and the computed pressure signals by tuning  $C_f$  value are shown and compared in Fig. 53. Comparing the Case A1 here and Case 4 (which model corresponds to the pressure signal results shown in bottom of Fig. 50), small improvements in predicted pressure amplitude can be observed and the 3L acoustic mode is more dominant in PSD plot. Increasing  $C_f$  to 1.0 helps improve the pressure prediction, but further improvement is not achieved when  $C_f$  is further increased to 2.0, in which case the 1L mode starts to dominate over the 3L response. Overall, tuning the value of  $C_f$  is shown to provide small improvements on the predictions, but the overall effects are insignificant as evident in the pressure time histories and PSD's shown in Fig. 53.

Table 8. Summary of TAB model tuning effects on pressure signal predictions.

Operating Conditions	Case Name	Total peak-to-peak pressure amplitude (%)	Dominant Acoustic Mode	Secondary Atomization Model
$T_{air} = 800K$ , $\phi = 0.6$	Case A1: Baseline $C_f = 1/3$	0.7	3L	TAB
	Case A2: $C_f = 1.0$	0.8	3L	
	Case A3: $C_f = 2.0$	1.0	1L	

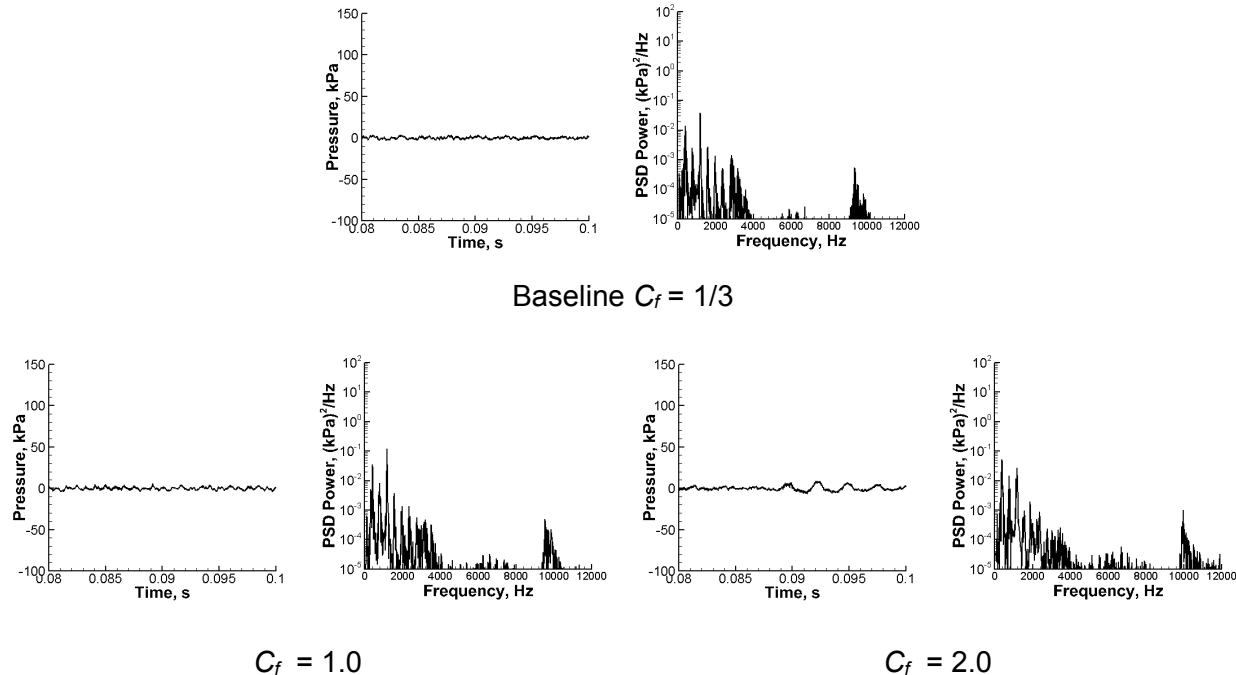


Figure 53. Comparisons of TAB model constants tuning effects on pressure predictions.

#### 4.4.1.2. Tuning of KH model

The two model constants  $B_0$  and  $B_1$  in the KH model are varied to promote more secondary breakup. The constant  $B_0$  controls the child drop size after breakup as shown in Eq. (17) and  $B_1$  determines the breakup time in Eq. (19). By decreasing  $B_0$ , the size of the child drops after secondary breakup is expected to decrease; whereas by decreasing the value of  $B_1$ , the secondary breakup process is expected to be faster. Both of these effects are aimed at accelerating the secondary breakup process, thereby decreasing the child drop size and generating more gaseous fuel.

Table 9. Summary of KH model tuning effects on pressure signal predictions.

Operating Conditions	Case Name	Total peak-to-peak pressure amplitude (%)	Dominant Acoustic Mode	Secondary Atomization Model
$T_{\text{air}} = 800\text{K}$ , $\phi = 0.6$	Case B1: Baseline $B_0 = 0.61$ , $B_1 = 10.0$	0.5	3L	KH/RT
	Case B2: $B_0 = 0.5$ , $B_1 = 10.0$	0.7	3L	
	Case B3: $B_0 = 0.2$ , $B_1 = 10.0$	1.1	1L	
	Case B4: $B_0 = 0.61$ , $B_1 = 2.0$	0.7	3L	

The KH model tuning effects are summarized in Table 9 and the predicted pressure comparisons are shown in Fig. 54. By using only the KH/RT model to describe secondary atomization, the baseline case (Case B1) shows a small improvement in capturing the dominant 3L frequency compared with the hybrid model (Case 4) in Figure 54. As discussed above, using only the TAB model also improved the prediction slightly. These results may therefore indicate some inherent limitations of hybrid model in combining TAB and KH/RT models based on the Weber number.

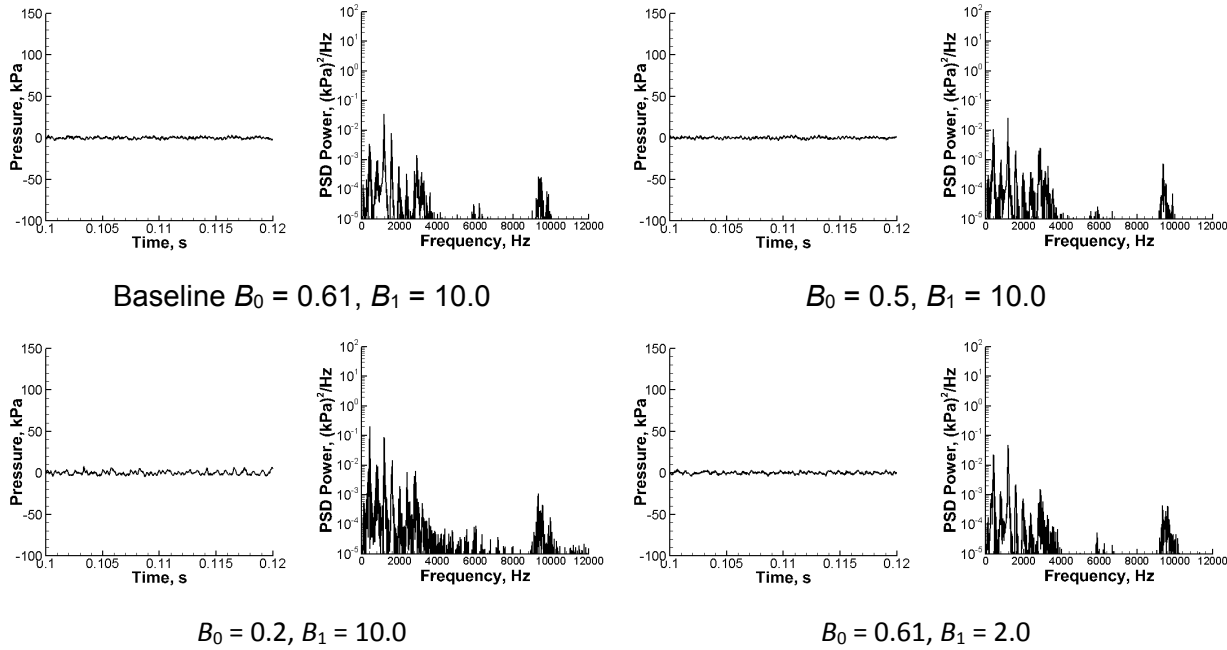


Figure 54. Comparisons of KH model constants tuning effects on pressure predictions.

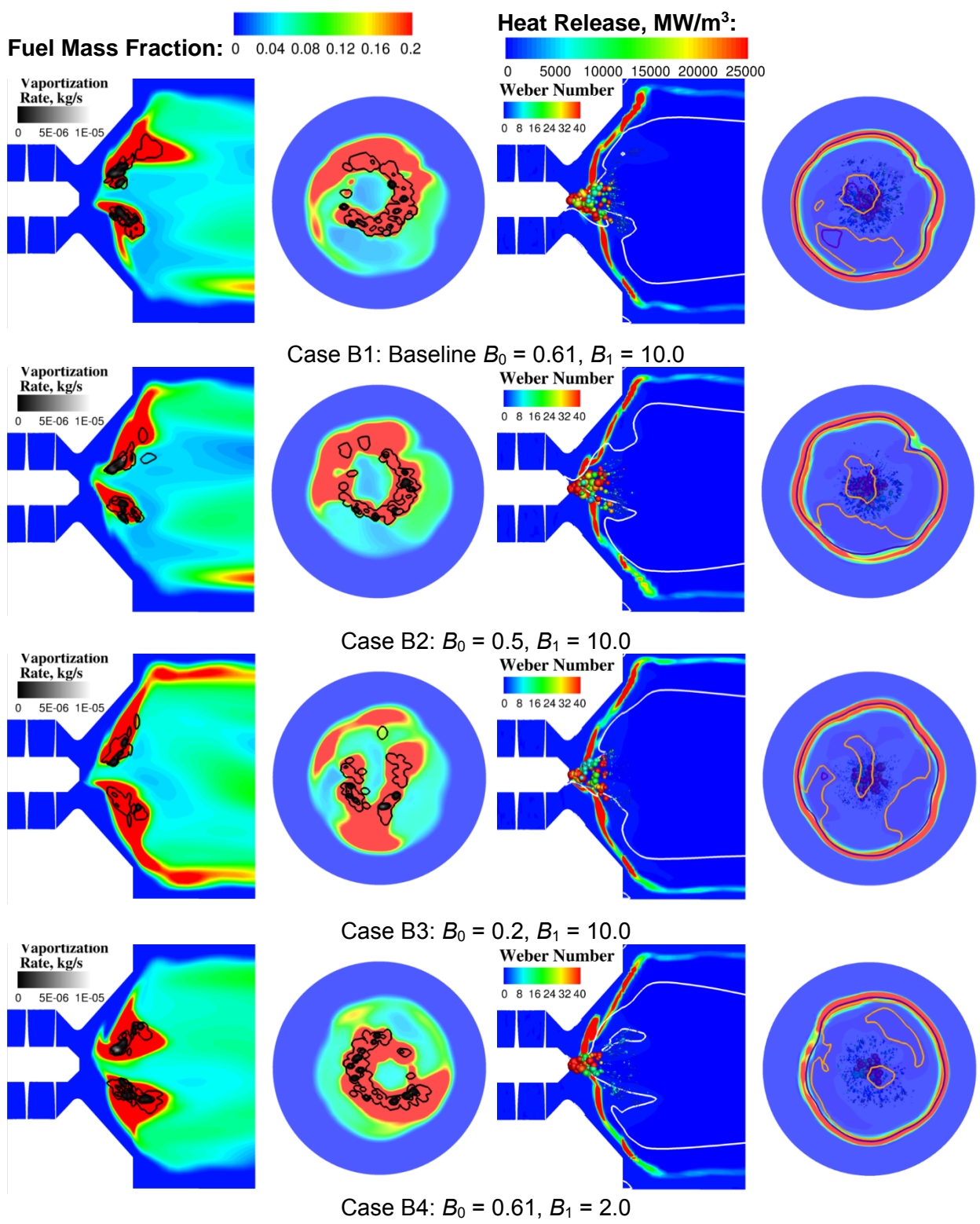


Figure 55. Comparisons of KH model constants tuning effects on predictions of vaporized fuel and heat release distribution.

The first tuning step serves to decrease the value of  $B_0$  while keeping  $B_1$  the same (Case B2 and Case B3); this leads to a nominal pressure amplitude increase and, eventually, the 1L acoustic mode becomes more excited than the 3L mode. The second step serves to decrease the value of  $B_1$  to accelerate the spray breakup (Case B4). Again, the predicted pressure amplitude increases somewhat with the 1L and 3L appearing as the most two dominant modes observed in the PSD plot in Fig. 54. However, the overall effects in improving combustion instability predictions are not significant and the simulations still under-predict the pressure amplitude compared with experimental measurements.

To further understand the effects of model tuning and to help guide fuel spray modeling improvements, the spray characteristics, gaseous fuel mass fraction and heat release rate distributions are compared for different KH model constants and are shown in Fig. 55. The vaporized fuel mass fraction is shown as the background rainbow contour and the vaporization rate is shown as contour lines in grey scale in the left column. The heat release is shown as the background rainbow contour with fuel spray drops colored by the Weber number. An iso-line of zero axial velocity is highlighted in white to represent the Vortex Breakup Bubble (VBB), which was determined to be responsible for the major mechanism to sustain combustion instability in the LDI combustor. A cross-sectional view is selected 1mm downstream of the dump plane to visualize the three-dimensional effects in each figure and iso-lines of gaseous fuel mass fraction are overlapped in heat release contour.

In the side view, the spatial distributions of the vaporization rates for all four cases look similar and follow the hollow cone configuration as specified by the fuel spray injection with a cone angle around  $65^\circ$ . In the cross-sectional view, the spatial distributions of the vaporization rate show a spiral structure, which is driven by the strong swirling flow generated by the swirler upstream. Cases B1 and B2 have similar asymmetric gaseous fuel distributions in the side view and similar spiral structures as the vaporization rate in cross-sectional view.

In Case B3, the fuel distribution is more symmetric and stretched in the side view. Moreover, with reduced model constant  $B_0$ , it can be seen that more small-size drops with lower Weber number are generated in the chamber compared with Case B1 and B2. Those small drops can be easily driven by the flow-field, following the VBB outline and vaporizing in downstream locations. This is probably the reason that the gaseous fuel distribution in Case B3 assembles the shape of the VBB and more fuel is present in the chamber.

In Case B4, the fuel distribution is also different from the other three cases. With model constant  $B_1$  reduced, the secondary atomization process occurs faster and consequently even more small-size drops are generated than in Case B3. This accelerated KH breakup model produces small drops at a high rate, which in turn limit the time for the flow-field to interact with the small drops and therefore the gaseous fuel distribution here is more compact and more restricted to the diverging section.

Though differences can be observed in the fuel distributions and spray characteristics by tuning the KH model constants, the heat release distributions look very similar for all four cases and the tuning effects on the VBB are also not very significant, which explains why the improvements in pressure predictions (in Fig. 54) are not significant either. These results suggest that stronger effects may arise in the early stages of fuel spray formation such as the free surface flow inside fuel injector and the primary atomization process. Accordingly, the results in the next section are focused on the effects of primary atomization on the fuel spray distribution.

#### **4.4.2. Effects of Fuel Spray Distribution**

Instead of including a primary breakup model, a specified fuel spray distribution with hollow cone configuration is applied to assess the effects of fuel spray distribution on combustion

instability predictions. In these studies, the hybrid model is retained to describe secondary atomization. The types of distributions and their effects on the pressure predictions are summarized in Table 10 and the predicted pressure signals are shown in Fig. 56. Compared with the tuning studies of secondary breakup models, it is apparent that the improvements on pressure signal predictions by specifying a drop distribution are more significant.

Table 10. Summary of fuel spray distribution effects on pressure signal predictions.

Operating Conditions	Case Name	Total peak-to-peak pressure amplitude (%)	Dominant Acoustic Mode	Secondary Atomization Model
$T_{\text{air}} = 800\text{K}$ , $\phi = 0.6$	Case C1: Uniform spray distribution ( $d_{\text{mean}} = 78 \mu\text{m}$ )	20	3L/1T	Hybrid TAB/KH/RT
	Case C2: Log-normal spray distribution ( $d_{\text{mean}} = 56 \mu\text{m}$ )	4	4L	
	Case C3: Log-normal spray distribution ( $d_{\text{mean}} = 78 \mu\text{m}$ )	1.5	3L	
	Case C4: Log-normal spray distribution ( $d_{\text{mean}} = 156 \mu\text{m}$ )	8	1T1L	

The predicted pressure signal seems to be very sensitive to the specified fuel spray distribution based on Table 10 and Fig. 56. By using a uniform fuel spray distribution with mean diameter of  $78 \mu\text{m}$  (Case C1), which is comparable to the liquid sheet thickness obtained from the offline VOF computation described in section 4.2.4, the predicted pressure amplitude is closer to experiment measurement shown in Figure 50. The 3L mode is predicted to be dominant, which is close to the 4L mode observed in the experiments. However, the response at 1T is over-predicted while the frequencies that lie in between the 3L and 1T modes are under-predicted.

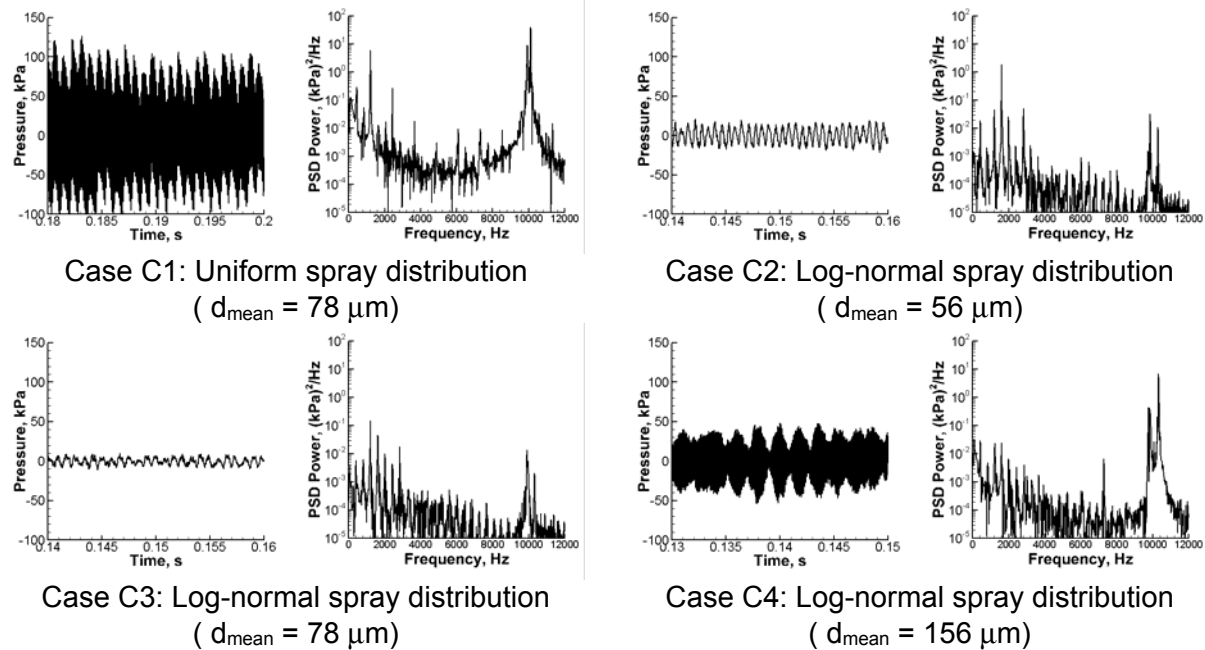


Figure 56. Comparisons of fuel spray distribution on pressure predictions.

Use of a log-normal distribution with a mean diameter of 56  $\mu\text{m}$  (comparable to drop size measured from the atmospheric spray measurement), shifts the dominant acoustic frequency to the 4L mode in agreement with the experiments, but the pressure amplitude is under-predicted (Case C2). Moreover, increasing the mean diameter in the log-normal distribution does not help improve the pressure predictions. Case C3 predicts the 3L mode as the dominant frequency but the pressure amplitude is even lower than Case C2. Further doubling the mean drop size (Case C4), the prediction in pressure amplitude is improved and getting closer to the experimental measurements, but 1T-1L acoustic mode is predicted to be the most dominant mode while the contributions of the longitudinal acoustic modes are significantly under-predicted.

Detailed comparisons on the fuel spray distribution effects are shown in Fig. 57. The contents of these plots are similar to the plots in Fig. 55. The distributions of gaseous fuel mass fraction, heat release and spray characteristics are studied specifically. One major difference due to the replacement of the primary breakup LISA model with a specified drop distribution is that the heat release level has been increased significantly, which may be related to the improvements in predicted pressure oscillation amplitudes. With more unsteady heat release coupled with pressure fluctuations, the driving of instability becomes stronger. Moreover, another important difference is that the spray drop sizes left in the domain in Cases C1 and C3 are much smaller than those in Cases B1 - B4. It should be noted that the initial drops injected to the chamber are of similar size ( $\sim 78\mu\text{m}$ ) for these cases. This indicates that the LISA model under-predicts the spray breakup process. More importantly, it indicates the great degree of sensitivity of combustion instability predictions to local spray drop distribution, breakup and vaporization phenomena.

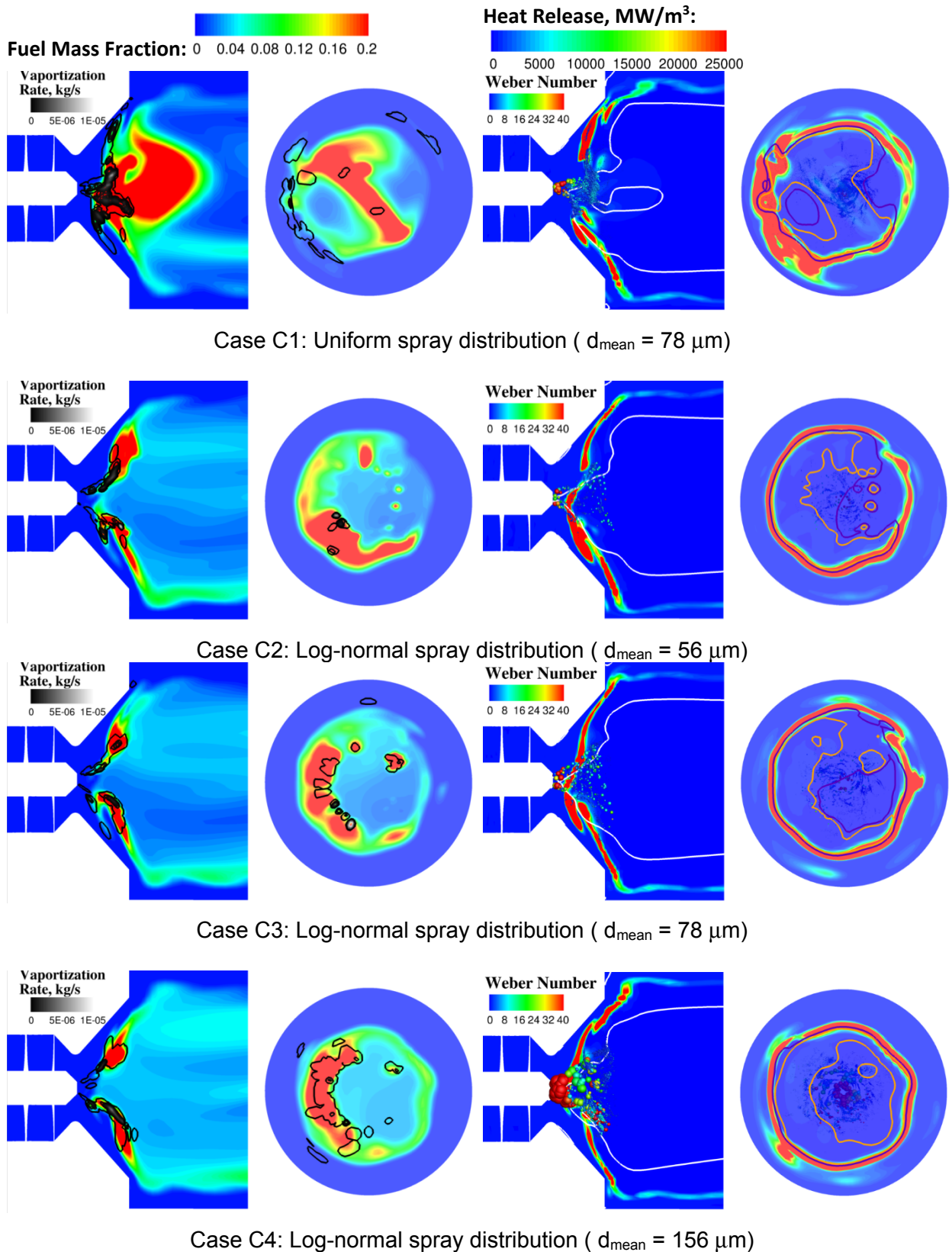


Figure 57. Comparisons of fuel spray distribution on predictions of vaporized fuel and heat release distributions.

Very different behavior can also be observed by comparing results using uniform drop distribution and those using a log-normal distribution. For the uniform distribution case (C1), the high vaporization rate is concentrated near the central region, which generates a large amount of gaseous fuel there. For all the log-normal distribution cases (C2, C3 and C4), the vaporization rates follow a hollow-cone-like structure (consistent with the spray injection configuration). Also, the heat release rate in Case C1 is much lower in the center region where fuel is rich and it is more concentrated in space while the log-normal distribution cases predict a more extended and stretched flame. The concentrated heat release distribution can be the reason why the predicted pressure amplitude is higher when using uniform distribution. In addition, an intact VBB can be observed in Case C1, which weakens the center reversing flow and allows the vaporized fuel to accumulate. In contrast, for the other cases, the VBB structure is complete and the strong reversing flow in the center forces the vaporized fuel to follow the bubble outline and form a conical shape. It is therefore evident that the type of spray drop distribution can be critical for determining the predicted flow-field and the associated combustion response.

Cases C2 - C4 use the log-normal distribution but the mean drop diameter is varied. Other than the difference in the spray drop size, these three cases predict similar spatial distributions of the vaporized fuel mass fraction, spray vaporization rate and heat release but interestingly show very different instability behaviors as summarized in Table 10 and Fig. 56. This indicates the strong sensitivity of predicted pressure oscillations to the mean spray drop size. As shown in Fig. 50 (bottom left), a very rich frequency spectrum has been found in the measured pressure signal. Therefore, small changes in the spray distribution can trigger a different mode of coupling of the unsteady combustion response with any specific frequency in the spectrum.

Overall, replacing the primary breakup model with a specified spray drop distribution and applying some moderate amount of adjustment in distribution are seen to have significant effects in combustion instability predictions. However, the predictions can be very sensitive to the distribution specified and the distribution adjustment needs to be performed very carefully to reach reasonable agreement with the experimental measurement. More specifically, these results point to the need for more directly coupled *ab initio* models of the atomizer free surface flow and the primary atomization processes, thereby avoiding *ad hoc* assumptions of droplet distributions that are likely to be problem-dependent.

#### **4.5. EFFECTS OF CHEMICAL KINETICS**

A more detailed mechanism (18-step as shown in section 4.2.3) is applied and compared with the case with two-step global reactions to evaluate the effects of chemical reactions. The predicted high-pass filtered pressure signals are shown in Fig. 58 with two equivalence ratios. The simulations are still in progress so preliminary results are shown here.

With a more detailed chemical model, the predicted pressure oscillation amplitude is more comparable to the measurement shown in Figs. 50 and 51 but a bit under-predicted. The 4L acoustic mode is dominant at high equivalence ratio with a comparable amplitude of the 5L mode, which is not observed in either the experiment or the simulation using two-step chemistry. It seems that more frequencies can be observed using more detailed chemical model, especially enabling the simulation to predict the responses in between 6 and 8 kHz. Because the cases are still in progress, more studies are needed to fully assess the effects of chemical model in predicting combustion instability in this LDI model combustor.

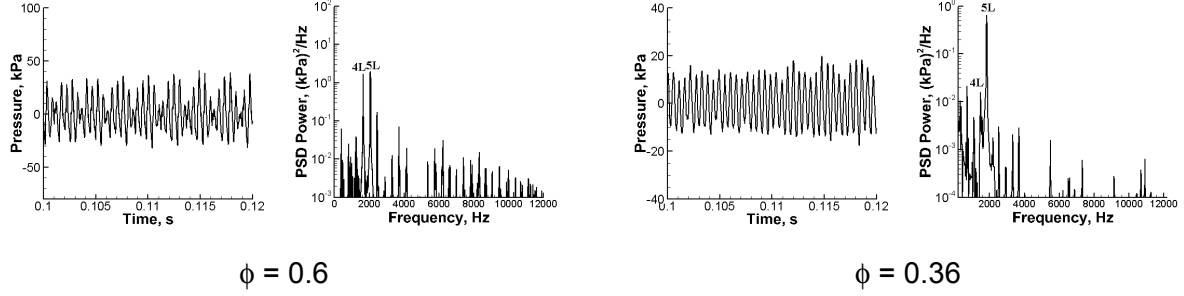


Figure 58. Simulation results for  $T_{air} = 800\text{K}$  with detailed chemical kinetics.

#### 4.6. IDENTIFICATION OF INSTABILITY MECHANISMS

Both simulations and experiments indicate the presence of multiple modes, with pressure oscillation amplitudes ranging over an order of magnitude that are strongly dependent on combustor resonance and equivalence ratio. There is a lesser effect on nozzle location, although the simulation disagrees with the experiment on its effect on limit cycle amplitude. It was suggested that the We-adaptive atomization modeling may be a source of the difference and static input provided better results. Modeling studies also showed that reaction modeling had an important effect, and showed coupling between hydrodynamics and acoustics. All these results strongly suggest a complex coupling between resonant flow dynamics, extinction and ignition, and acoustics. The simulation results were examined at the condition where there was most agreement with experiment to investigate potential mechanisms for the instability.

Results from the simulation with fuel nozzle upstream of the venturi throat at low equivalence ratio ( $\phi = 0.36$ ) are examined in detail to identify the underlying instability mechanisms. First, open geometry simulations made in the absence of strong acoustic forcing are presented to show the natural hydrodynamic modes that exist in the single-element LDI combustor. It is assumed that the absence of a contraction far downstream has negligible effect on the VBB mode. The hydrodynamic modes are established based on Dynamic Mode Decomposition (DMD) analysis of the open geometry results. Then, snapshots of the flow over one cycle of instability are shown. DMD analysis of the closed geometry simulation is performed for more detailed studies. The major findings and observations from the simulations can be summarized as follows:

1. The presence of a natural hydrodynamic Vortex Bubble Breakdown (VBB) mode – and its coupling with the chamber acoustic modes leads to instabilities at higher acoustic modes.
2. A Precessing Vortex Core (PVC), is also identified through DMD analysis and presents strong swirling dynamics in the venturi that corresponds to the high frequency content (6-8 kHz) observed in the pressure power spectra.
3. The presence of a potential nonlinear coupling between the dominant acoustic modes (6L) and the PVC hydrodynamic mode that may enhance intermediate frequencies around 4.6kHz.
4. The Rayleigh index spectrum identifies major instability driving at 5L/6L and PVC frequencies, which show dominance at different parts in the diverging section of the venturi. Comparable driving and damping regions are found at the 1L frequency, which produces a lower instability level than at 5L/6L.

#### 4.6.1. Open Geometry Simulation

The open geometry simulation was conducted at the baseline equivalence ratio ( $\phi = 0.36$ ), air temperature ( $T_{air} = 800K$ ) and mean chamber pressure ( $P_{back} = 1MPa$ ) to ensure that both spray and combustion are subject to similar conditions as in the closed geometry simulation. Examination of the pressure signal in the open-geometry simulation reveals that the acoustic perturbations are much lower than that in the closed geometry simulation and the natural acoustic frequency is around 850Hz as shown in Fig. 59. With weak contributions from acoustic field, focus of the reduced geometry simulation can be put on studying the naturally-occurring hydrodynamics and their effects on combustion.

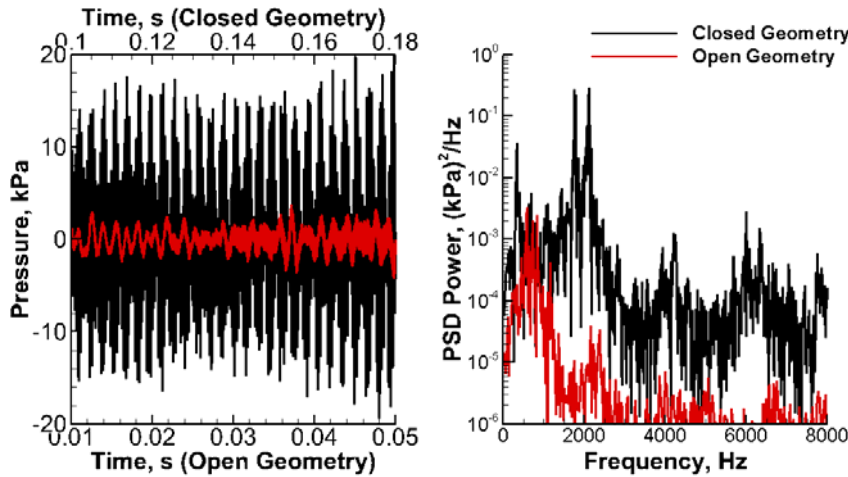


Figure 59. Comparisons of high-pass filtered pressure signals from closed & open geometry at chamber head section.

Figure 60 shows evidence of a vortex bubble breakdown (VBB) mode and its cyclic behavior over one period. Before proceeding to the analysis of the VBB modes found in our configuration, an overview of vortex breakdown in a high swirl number flow is provided. Vortex breakdown can be characterized as an abrupt axial flow deceleration leading to a stagnation point and region of reversed axial flow. It is usually represented using a zero-axial-velocity ( $U = 0$ ) iso-surface. A large amount of work on the mechanisms of vortex breakdown process can be found in non-reacting flow region [59-61]. Liang and Maxworthy [62] identified different states of vortex breakdown by varying the swirl number and found that the critical swirl number for vortex breakdown to appear is around 0.88 in their experiment (it should be noted that the swirl number of the swirler used in this configuration is 1); moreover, as the swirl number gets higher, the vortex breakdown bubble moves closer to the inlet swirler and the entrainment of surrounding fluid is accelerated. Self-excited/globally unstable VBB modes are also identified in both experiment [59-64] and direct numerical simulation [65]. Excitation of hydrodynamic instabilities by an acoustic field can generate relatively coherent flows, and flame perturbations, both of which can cause fluctuations in heat release that can further energize the acoustic modes [63, 66, 67]. VBB interactions with transverse acoustic field have been studied by Connor and Lieuwen [68]. It should be noted that most of the studies on vortex bubble breakdown above are performed with simple geometry configuration (e.g. dump plane) while the converging-diverging venturi here can increase the complexity of VBB physics in studying its interaction with acoustic field.

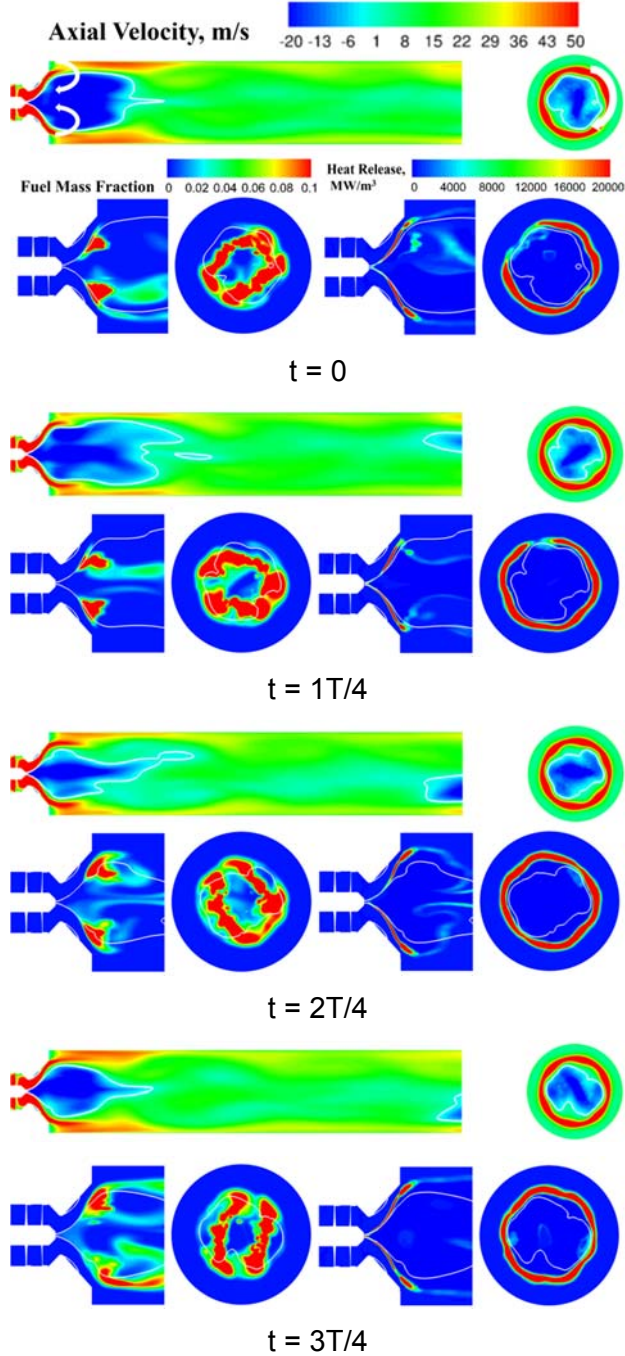


Figure 60. Time history of open geometry simulation for  $\phi = 0.36$   $T_{air} = 800K$  in one cycle of period (left: axial velocity; middle: fuel mass fraction; right: heat release; white line: contour line of  $U = 0$ ; cross section view is selected 1mm downstream to the exit of venturi).

The VBB mode in this configuration has a fundamental natural frequency of 575Hz identified using DMD analysis of results from the open geometry simulation with an open geometry (Figure 49). In Fig. 60, a contour line of zero axial velocity ( $U = 0$ ) was selected in each snapshot to visualize the mode in the region near the combustor head section. Flow inside the bubble (white line) travels upstream and flow outside travels downstream, triggering a pair of counter rotating vortices indicated by the white arrows in the first snapshot (top velocity contour). The swirling motion introduced by the air swirler upstream of the venturi produces a clockwise rotation of the

flow in the azimuthal direction, as seen in the cross sectional view near the exit of the venturi section.

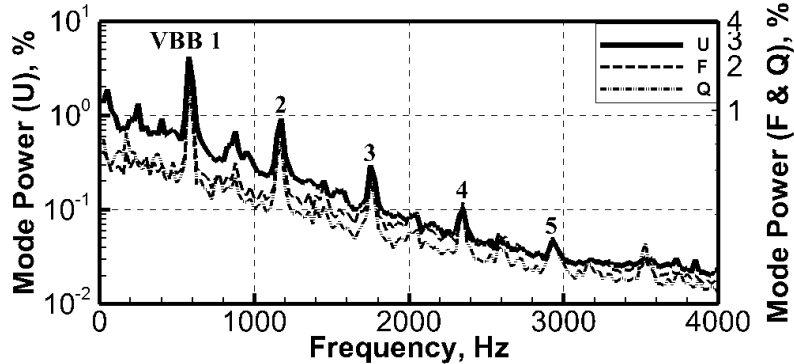


Figure 61. DMD frequency spectrum of axial velocity (U), fuel mass fraction (F) and heat release (Q) variations from open geometry simulation for  $\phi = 0.36$   $T_{air} = 800K$ .

The influence of the VBB process on combustion responses can be investigated by visualizing the fuel mass fraction and heat release contours at the bottom of each snapshot. At  $t = 0T/4$ , the vortex bubble is strong and compact. Starting from  $t = 0T/4$  to  $T/4$ , it grows and stretches downstream. During the growth, the reverse flow area (region with negative axial velocity inside the vortex bubble) increases and the forward flow area (region with positive axial velocity surrounding the vortex bubble) decreases. In that way, more fuel is brought back into the diverging section by the reverse flow and less can come out. With the fuel concentrated in the diverging section, the heat release distribution is compressed. The stretching of the vortex bubble is greatest at  $t = T/4$  beyond which it starts to break down. From  $t = T/4$  to  $3T/4$ , the bubble contracts and becomes more centered. As the bubble contracts, the reverse flow area decreases and there are large areas of forward flow around the combustor periphery that bring fuel out of the diverging section downstream into the combustor. The heat release distribution also moves further downstream, along the periphery of the chamber.

The use of Dynamic Mode Decomposition (DMD) provides a clear insight into dynamic patterns of the quantities of interest. The DMD procedure is similar to Proper Orthogonal Decomposition (POD) but whereas POD typically has multiple frequencies associated with each mode, each DMD mode only contains a single frequency [69]. Comparisons between the DMD and POD analyses applied to axial combustion instabilities by Huang et al. [70] has led to the conclusion that the underlying physics can be more efficiently understood with DMD, especially when there are strong instabilities present.

Here, the DMD is performed to analyze the fluctuating parts of quantities shown in Fig. 60. The frequency spectra of the VBB, the fuel mass fraction, and the heat release modes are plotted in Figure 61, which clearly show the coupled behavior of the three quantities. As mentioned above, the fundamental frequency is around 575Hz, which corresponds to the first VBB mode (VBB1). Well-defined higher harmonics of VBB modes can also be clearly identified from the spectra. We also note that the DMD spectrum does not show any significant acoustic mode content in the chamber for this open geometry simulation though a weak peak around 850Hz is still observable in the spectra. We will contrast this later with the spectrum corresponding to the closed geometry simulation.

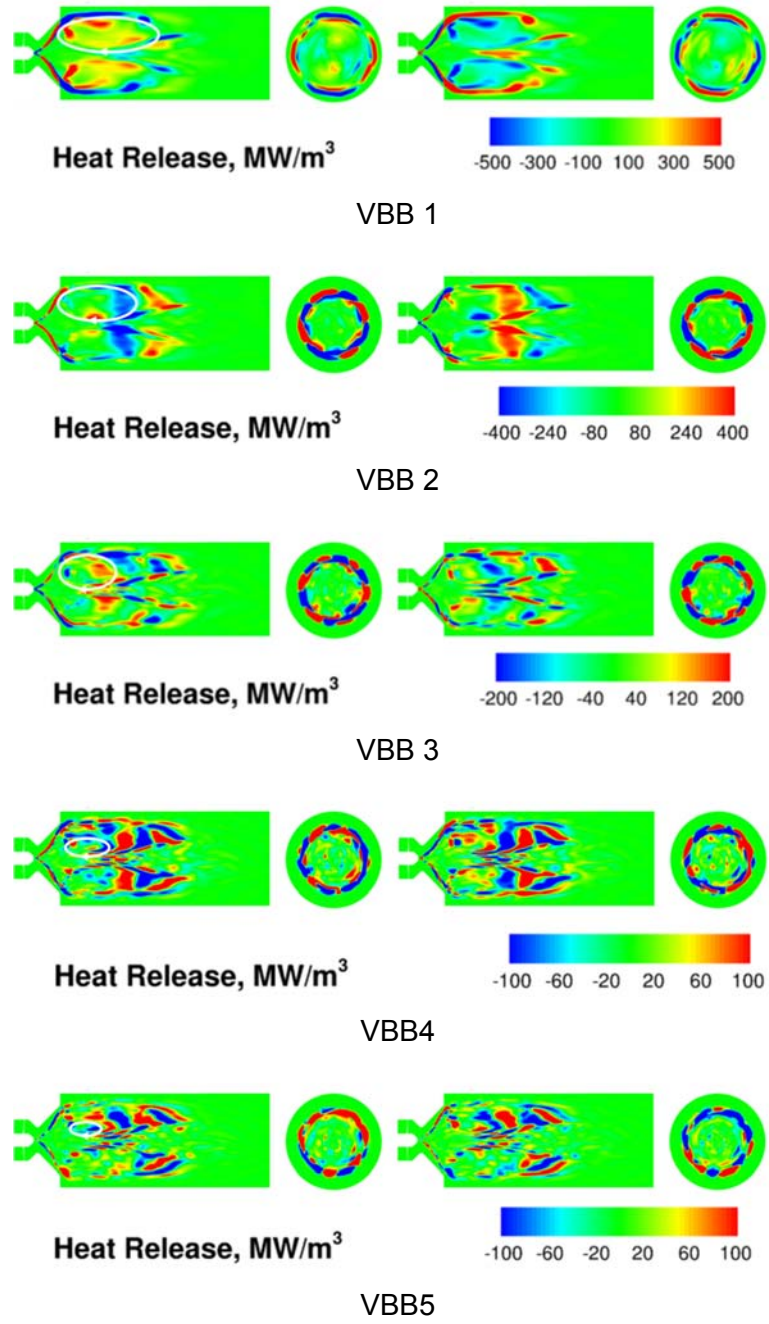


Figure 62. Heat release VBB modes reconstructed from DMD analysis for open geometry simulation for  $\phi = 0.36$   $T_{\text{air}} = 800\text{K}$  (cross section view is selected 1mm downstream to the exit of venturi).

Responses of heat release fluctuations are reconstructed at each harmonics of VBB modes using DMD modes and are shown in Fig. 62. Two representative time instants were selected based on the status of vortex bubble. Snapshots at left represent dynamic responses of heat release during bubble growth ( $t = T/4$  in Fig. 60) when heat release in the diverging section increases and is compressed towards the chamber center line. Snapshots on the right show the responses during bubble contraction ( $t = 3T/4$  in Fig. 60) when heat release decreases in the diverging section and is more stretched towards the chamber wall. Heat release occurs in the

shear layer and follows the vortex bubble. The vortex bubble sizes under each VBB harmonics are highlighted using white circles on the left of Fig. 62. At harmonics, the bubble size decreases and more spatial variations of heat release can be observed from both the side and cross-section views. Therefore, a shorter turnover time of flow-field and a faster bubble size contraction/growth rate should be expected at higher VBB harmonics.

The existence of natural hydrodynamic modes (VBB) provides a strong driving force for local combustion responses and as a result increases the opportunities of specific acoustic modes to be locked in with those VBB modes. The frequencies of the VBB modes observed in the open geometry simulation and the acoustic modes in the closed geometry simulation are summarized in Table 11. The VBB3 and 5L modes have closest frequencies and are expected to have a better probability to couple. However, it should be noted that the frequency of VBB modes here are weakly influenced by the acoustic field and it could be expected that stronger acoustic interactions in a closed chamber may cause a shift in the behavior of the VBB modes and hence a shift in the combustion response [68]. These details will be discussed in greater detail in the following section that considers the closed geometry simulation results.

Table 11. Summary of frequencies of hydrodynamic modes and acoustic modes identified in LDI combustor using open and close geometry simulation respectively.

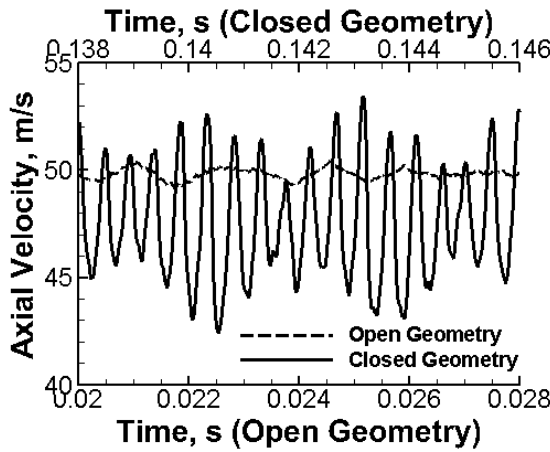
VBB Mode	Frequency, Hz	Acoustic Mode (Longitudinal)	Frequency, Hz
1	575	1	330
2	1175	2	650
3	1750	3	1075
4	2350	4	1450
5	2926	5	1800
		6	2125

#### 4.6.2. Closed Geometry Simulation

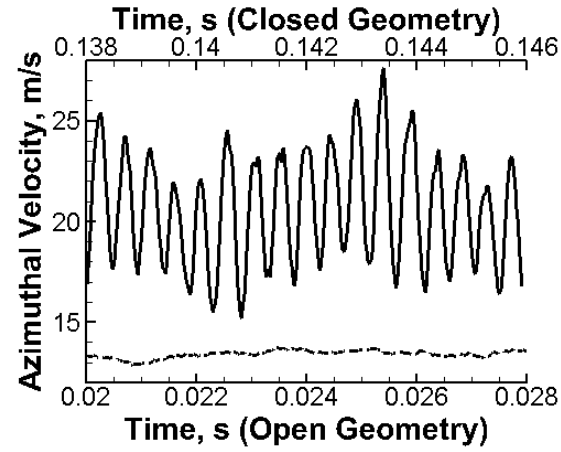
In this section, we examine the important instability mechanisms observed in the LDI combustor by considering an analysis of the results of an acoustic cycle corresponding to the closed geometry simulations. This case corresponds to the PSD results in Figure 51, which are dominated by 5L and 6L acoustic response. Two mechanisms are noted: first, enhanced vaporization of fuel droplets due to the incoming compression wave; and secondly, interactions between the compression wave and the hydrodynamic modes that determines the fuel distribution and triggers enhanced mixing. In addition, DMD analysis is used to elucidate the other important physical interactions in LDI combustor. A second hydrodynamic Precessing Vortex Core (PVC) mode, is identified as the source of high frequency pressure oscillations between 6 and 8kHz observed in the PSD plots (Figure 51). The potential for nonlinear interactions between the dominant acoustic modes (5L and 6L) and the PVC mode is also discussed. Lastly, a Rayleigh index spectrum is established using DMD analysis to highlight important dynamics and to identify driving/damping locations.

Before detailed discussions of instability mechanisms, it is necessary to obtain some preliminary understanding of acoustic effects on the flow-field. To do that, the velocities from open and closed geometry simulations are compared at two representative locations highlighted in Figure 49 (Detail B). The velocities are volume-averaged at each location. Location 1 is selected to monitor the inlet axial velocity to the swirler, which largely determines the states of hydrodynamics occurring downstream. As shown in Fig. 63 (left), with stronger pressure oscillations in closed geometry simulation (Fig. 59), the inlet axial velocity has higher fluctuating amplitude than that in open geometry. However, it can also be indicated that the mean axial

velocity decreases when stronger acoustic forcing is present in closed geometry. In that way, the frequencies of VBB modes are expected to be lower in closed geometry simulation than those observed in open geometry. The azimuthal velocity downstream shows the opposite trend with stronger pressure oscillations as shown in Fig. 63 (right). The swirling effect seems to be more significant in closed geometry than in open one, which can be the origin of the PVC mode mentioned above.



Axial velocities monitored at location 1



Azimuthal velocities monitored at location 2

Figure 63. Comparisons of axial and azimuthal velocities between open and closed geometry simulation.

#### 4.6.2.1. Cycle Analysis

Figure 64 shows a pressure-time trace taken at the combustor dump plane from the simulations and two dominant acoustic cycles can be identified. First, the pressure fluctuates mainly at the 5L and 6L frequencies. Second, modulations in the pressure amplitude can be observed at the 1L frequency. Cycle analysis is performed based on one specific 6L acoustic cycle highlighted in Fig. 65. Five time instants are selected to examine the physics as shown in Fig. 65. The acoustic goes through a slow expansion from Time 1 to 3 and a rapid compression from Time 3 to 5 at the chamber head section. In addition, the corresponding axial (from location 2) and azimuthal (from location 1) velocity signals are extracted from Fig. 63 to help understand the interactions between fluid dynamics and acoustics.

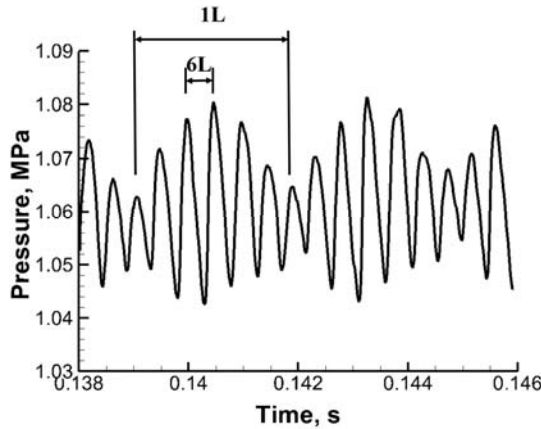


Figure 64. Pressure-time trace taken at the combustor dump plane (location 1 highlighted in Figure 49).

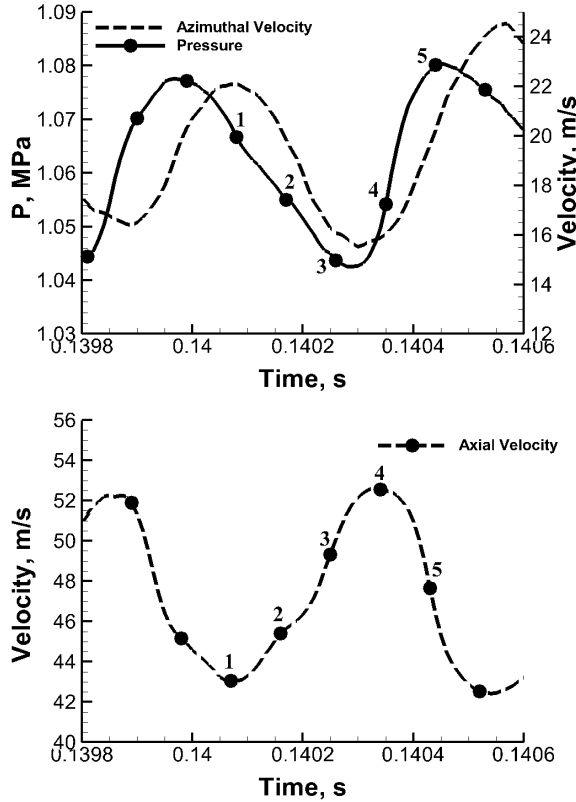


Figure 65. Acoustic cycles defined based on 6L frequency (the pressure and azimuthal velocity, top, are monitored at location 1 and the axial velocity, bottom, and is monitored at location 2 highlighted in Figure 49).

Figures 66 and 67 show a series of plots for the five points in the cycle marked in Fig. 65. Figure 66 limits the side-view of pressure and axial velocity contours to the first 25% of combustor length to focus on the dominant acoustic mode. The iso-surface of zero axial velocity is overlapped and colored by pressure on the plots to visualize the vortex breakdown bubble. The cross-sectional view is selected 1mm downstream of the dump plane to visualize the three-dimensional effects in the combustor. Figure 67 shows the behaviors of spray and combustion in the diverging section of the venturi and just downstream of the dump plane, where most of their dynamics happen. A white iso-line of  $U = 0$  is marked in each subplot to locate the vortex breakdown bubble. Fuel mass fraction contours are shown on the left with the fuel vaporization rate overlapped and colored in grey scale. Heat release contours are shown on the right with the fuel droplets sized by the radius and colored by the Weber number. Contour lines of fuel mass fraction are attached on the heat release contours in the cross-sectional views. The cross-sectional views are selected at the same location as those used in Fig. 66.

Starting from time 1 to 3, as shown in left column of Fig. 66 (a) to (c) the acoustic wave travels downstream and experiences expansion in chamber head section. The pressure in the combustor head section is decreasing from its maximum value in Fig. 65 (top) and the upstream inlet axial velocity starts to increase from its minimum in Fig. 65 (bottom), during which the axial velocity field in the venturi is also expected to increase. This decreases the local swirling number and as a result swirling velocity downstream decreases in Fig. 65 (top). This can also be indicated by comparing the cross-section axial velocity contours at times 1, 2 and 3 during which the swirling effects are strongest at Time 1 and getting weaker as it steps to Time 2 and 3. Clear azimuthal variations can be observed at Time 1 while the distributions are more uniform at Time 2 and 3. Though the axial flow is weakened in the venturi section, the forward flow area is bigger than the

reverse flow area in chamber head section, which indicates the vortex bubble contraction as discussed in part 4.6.1 and this state sustains throughout the acoustic expansion (Time 1 to 3).

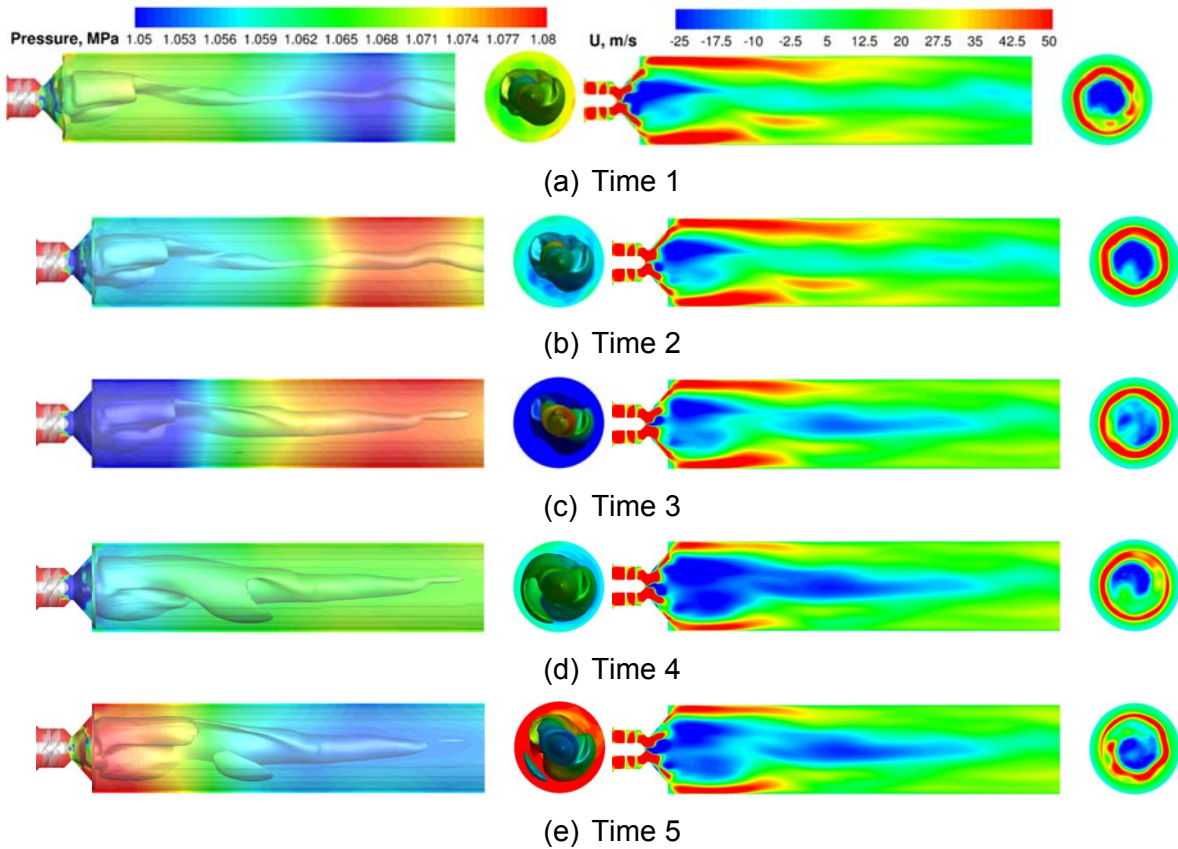


Figure 66. Time history of pressure and velocity field in closed geometry simulation for  $\phi = 0.36$   $T_{air} = 800K$  in one 6L cycle (The iso-surface represents the Vortex Breakdown Bubble ( $U=0$ ) and colored by pressure; cross section view is selected 1mm downstream to the exit of venturi).

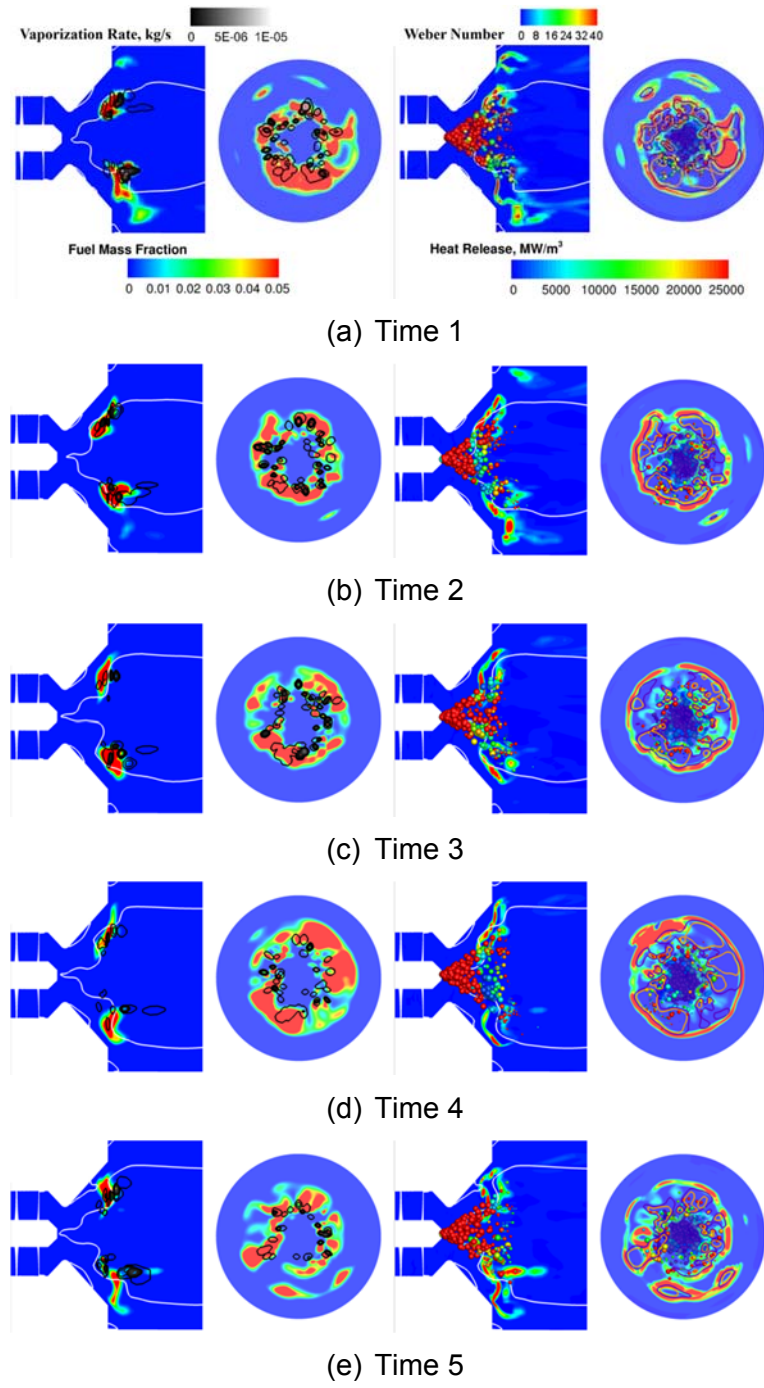


Figure 67. Time history of combustion and spray characteristics in closed geometry simulation for  $\phi = 0.36$   $T_{air} = 800K$  in one 6L cycle (left - fuel mass fraction and fuel vaporization rate; right - heat release with spray drops overlapped, sized by radius and colored by Weber number; white line: contour line of  $U = 0$ ; cross section view is selected 1mm downstream to the exit of venturi).

At Time 1, a well-defined spray cone angle can be identified ( $\sim 64^\circ$ ). Because pressure is relatively high at Time 1, a high Weber number is observed that are relatively unstable and are broken up into small drops in the diverging section. Moreover, the high pressure wave compresses the vapors, increases gas-phase density and thereby increases fuel spray vaporization so that fuel mass fraction level increases. During the expansion of acoustic wave, the vortex bubble is at its contraction and similar to the observations in Fig. 60, gaseous fuel follows the compressed bubble, extends into the combustor, and results in a more distributed heat release that stretches into the combustor as well.

At Time 2, the Weber number decreases with the decreasing pressure, less secondary atomization occurs, and a higher number of larger drops are left in the diverging section. Vaporization is slower compared with Time 1, causing a reduction in the level of gaseous fuel and heat release. The vortex bubble almost reaches its most contracted state beyond which the bubble starts to grow.

At Time 3, the local pressure field transfers from an expansion to a compression. Pressure reaches its minimum in chamber head section and acoustic compression wave starts to be reflected back downstream as shown in Fig. 66(c) (left). A negative pressure gradient is established near the head section, which brings reverse axial flow to the vortex bubble as shown in Fig. 66(c) (right). Stepping from Time 2 to 3, the bubble finishes its contraction and starts to grow, during which both the fuel and heat release distribution are anchored within the diverging section as shown in Fig. 67(c).

As the acoustic wave starts travelling upstream the compression progress starts from Time 3 to 5. As shown in Fig. 65, a rapid pressure rise can be observed, during which the inlet axial velocity increases first, peaks at Time 4 and then decreases till Time 5. This keeps the downstream azimuthal velocity low from Time 3 to 4 and promotes a sharp increase from Time 4 to 5. Due to amplified reverse axial flow brought by the strong reflected compression wave, the forward flow area shrinks and the reverse flow area grows as shown in the right column of 66(c) to (e). According to the discussion in part 4.6.1, this indicates vortex bubble growth. The acoustic compression process is coupled with vortex bubble growth.

From Time 3 to 4, as pressure increases, the Weber number becomes higher, and smaller drops are generated in the diverging section due to the secondary atomization. The compression wave promotes vaporization of these small droplets leading to a build-up of gaseous fuel. Because the azimuthal velocity is low during this period, fuel/oxidizer mixing is slow, which allows more vaporized gaseous fuel to be accumulated in the diverging section. The accumulated fuel is anchored and pushed towards the incoming air flow by the growing vortex bubble.

The cycle is completed at Time 5 when the pressure reaches its maximum value. The azimuthal velocity also increases to nearly its maximum from Time 4 rapidly. This indicates a continuous acceleration of swirling flows in chamber head section, which enhances the fuel/oxidizer mixing and with the fuel accumulation and anchoring towards air flow from Time 4, high intensity of heat release is observed in Fig. 67 (e). These processes keep consuming the fuel so that less fuel can be seen in the diverging section at Time 5 than at Time 4. From Time 4 to 5, the vortex bubble finishes its maximum growth and starts to contract, bringing generated fuel and heat release cross the dump plane as it steps into a new cycle.

From the examination of the cycle described above, it is clear that the acoustic field plays an important role in affecting the spray breakup and vaporization. It also drives the vortex bubble through the axial velocity field. Enhanced breakup and vaporization of spray drops are observed when pressure is high in the chamber head section, which generates more gaseous fuel for reaction. During acoustic expansion the vortex bubble contracts and brings more fuel downstream into the combustor away from air flow; in addition, as the inlet axial velocity increases, the

downstream azimuthal velocity decreases, slowing down the mixing between fuel and air. The heat release is reduced and is more distributed spatially. During acoustic compression, the vortex bubble grows and pushes more fuel into the diverging section towards the incoming air. In the first half of acoustic compression, the downstream azimuthal velocity is low, which allows accumulation of vaporized fuel. In the second half, the accelerated swirling motion in the third direction helps enhance the fuel/oxidizer mixing and generate large amount of heat release in the combustor. From the cycle analysis, the interaction between acoustic forcing and vortex breakdown bubble is conjectured as the key to sustain the combustion instability in this LDI combustor configuration. The natural VBB modes observed in open geometry simulation (Figure 61) are postulated to be driven and modulated by the acoustic modes in the closed geometry so that specific VBB modes lock in with higher acoustic modes to reach limit cycle.

#### 4.6.2.2. DMD Analysis

DMD analysis of the pressure, axial velocity, fuel mass fraction, and heat release fluctuations from the closed geometry simulation is presented next. The DMD frequency spectra are shown in Fig. 68. The spectrum of pressure is similar to the PSD plot in Fig. 51, showing the dominance of the 5L and 6L acoustic modes. A direct coupling with these acoustic modes is evident by the corresponding modes in the fuel mass fraction and heat release at the same frequencies. The spectra also show very strong modes of fuel mass fraction and heat release at about 4.6 kHz and 6.8 kHz, which are not directly coupled to a strong acoustic mode. It should also be pointed out that the results are in contrast with the corresponding DMD spectrum for the open geometry shown in Figure 61. An examination of the modes at the frequencies highlighted in Fig. 68 is provided next.

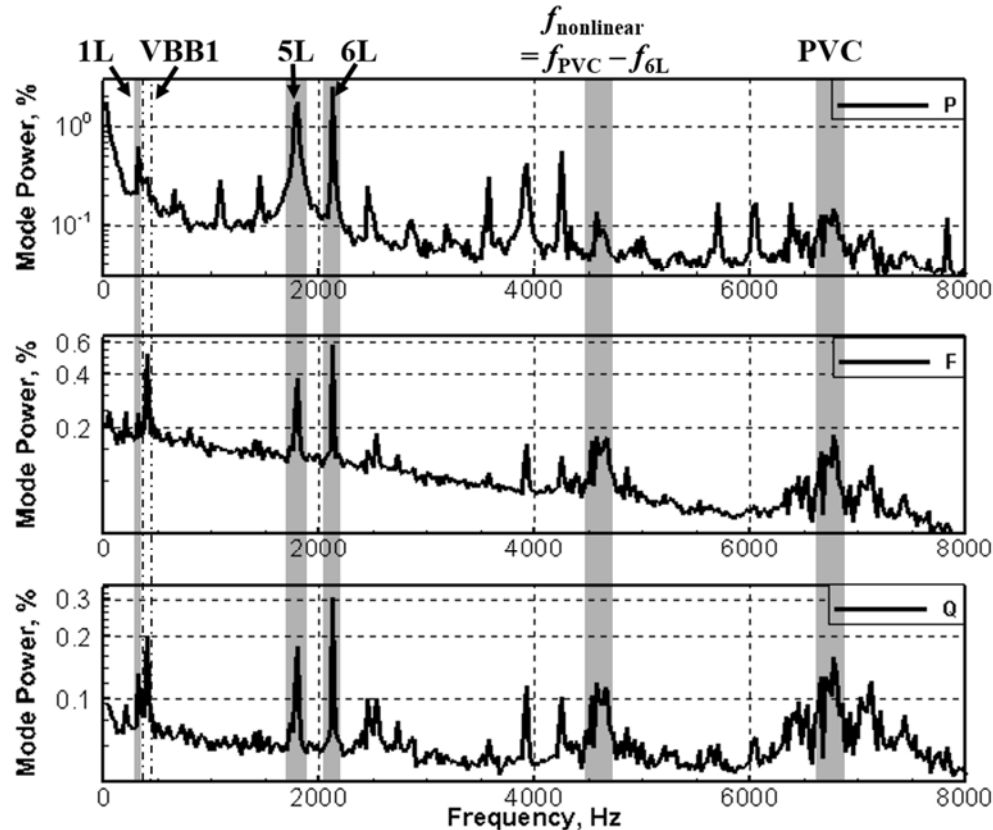


Figure 68. DMD frequency spectrum of pressure (P), fuel mass fraction (F) and heat release (Q) fluctuations from the closed geometry simulation for  $\phi = 0.36$   $T_{air} = 800K$ .

Starting from the responses at the most dominant acoustic frequencies (5L and 6L), and because of the similarity in the mode shapes, only a discussion of the 6L mode is included here. The major physics and coupling phenomena at these frequencies were discussed in the cycle analysis section. The reconstructed DMD responses help to extract specific mode shapes for the key physical quantities. Representative DMD responses at 6L acoustic wave compression are shown in Fig. 69 (consistent with Time 5 in Fig. 66 and 67). The spatial distributions of fuel mass fraction and heat release modes are fairly uniform in the azimuthal direction with a ring-like structure in the cross-sectional views, indicating the strong driving effect of the one-dimensional axial acoustic field. The heat release fluctuations closely follow the variations in fuel mass fraction. Variations in the radial direction are seen in both modes, but are most apparent in the heat release mode and arise due to the axial velocity distributions of the VBB mode. As shown in right column of Fig. 66, a strong reverse flow sits in the center region of combustor surrounded by weaker positive axial flow during acoustic compression. The reverse flow pushes fuel back towards the injector, while the outside flow convects the fuel downstream along the combustor wall. As discussed in part 4.6.2.1, at Time 5, the VBB has passed its maximum growth state and proceeds to contraction and therefore there is more fuel and heat release coming out of the diverging section in Fig. 69.

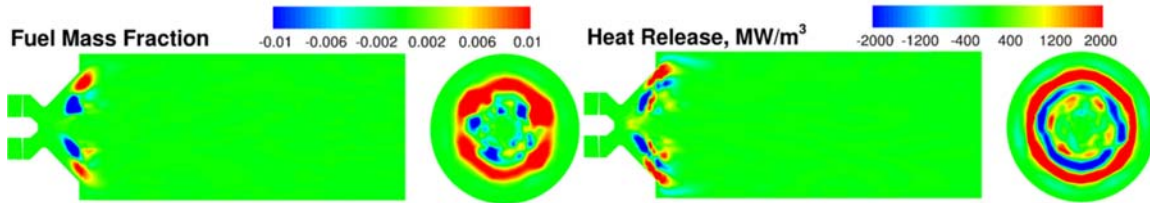


Figure 69. Representative reconstructed DMD responses at 6L for closed geometry simulation for  $\phi = 0.36$   $T_{air} = 800K$  (fluctuations of fuel mass fraction, left and heat release, right).

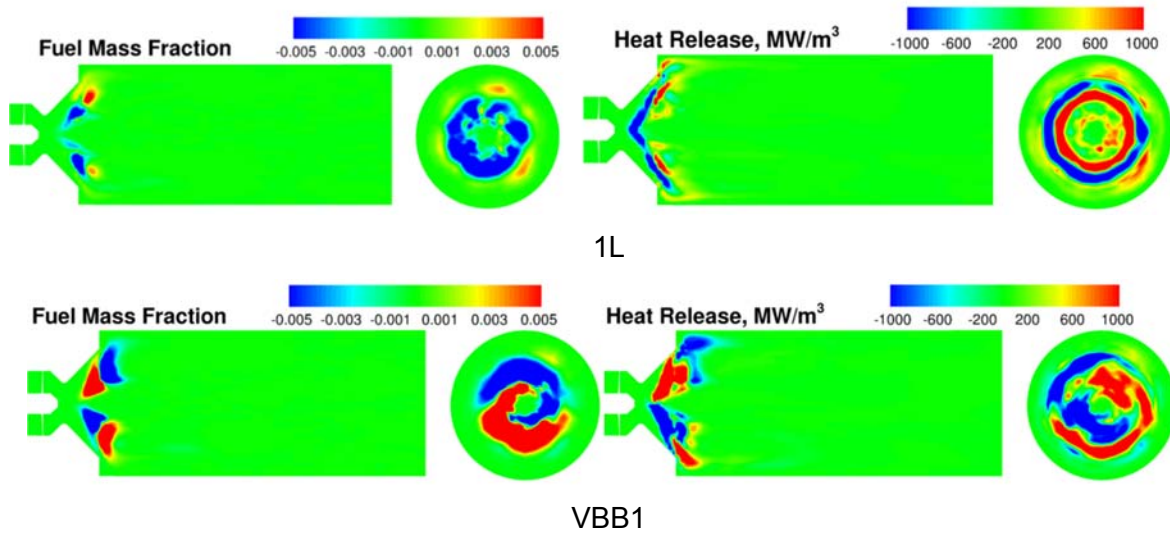


Figure 70. Representative reconstructed DMD responses at 1L (top) and VBB1 (bottom) frequencies for closed geometry simulation for  $\phi = 0.36$   $T_{air} = 800K$  (fluctuations of left: fuel mass fraction; right: heat release).

The DMD responses in the low frequency region are also interesting. In the open geometry simulation, with minimal acoustic influence, the vortex bubble breakdown is dominant at a fundamental frequency of 575Hz. Here in the closed geometry simulation, two frequency peaks are observed in the range of 300 to 450Hz. The 1L acoustic mode is around 330Hz and shows

dominance in pressure spectrum. The VBB1 mode is about 425Hz and is found in fuel mass fraction spectrum. Both 1L and VBB1 modes are found in the heat release spectrum. The representative DMD responses of the fuel mass fraction and heat release fluctuations at the two frequencies are shown in Fig. 70. Although the two frequencies are close, the mode shapes seem to be very different. The similarity between the 1L and 5L results can be seen by comparing Figs. 69 and 70 (top). As mentioned above, longitudinal acoustic modes drive the fuel and heat release with little azimuthal variation. However, the modal responses at the VBB1 frequency (425Hz) show distinct azimuthal variations. A helical structure is clearly indicated, and with the inclusion of the acoustic field, the distributions of fuel and heat release are seen to be more restricted within the diverging section and stretch to a lesser extent into the combustor compared to the analysis of open geometry simulation in Fig. 62.

In addition, as mentioned in discussing Fig. 63, the presence of the acoustic field alters the VBB frequencies from 575 to 425Hz. Table 12 shows this effect by summarizing the important VBB and acoustic frequencies. Compare the VBB mode frequencies with those corresponding to the open geometry given in Table 11. The closed geometry results indicate a close coupling between the VBB4 and the 5L acoustic modes, and between the VBB5 and the 6L acoustic modes. In fact, these couplings may help explain the dominance of the 5L and 6L modes for this case as seen in the pressure spectra in Figure 51. For low frequencies, the presence of two distinct modes (1L and VBB1) also helps explain the amplitude modulations at the 1L frequency observed in Fig. 65(a). We note, however, the 95Hz ( $\sim 30\%$  of 1L) frequency difference provides a less direct coupling between the 1L and VBB1 modes than the higher modes which drive the dominant response.

Table 12. Summary of frequencies of hydrodynamic modes and acoustic modes identified in LDI combustor using closed geometry simulation.

VBB Mode	Frequency, Hz	Acoustic Mode (Longitudinal)	Frequency, Hz
1	425	1	330
2	850	2	650
3	1275	3	1075
4	1700	4	1450
5	2125	5	1800
6	2400	6	2125

In the high frequency region ( $>5\text{kHz}$ ), an identifiable peak at around  $6.8\text{kHz}$  can be observed in the frequency spectra of both fuel mass fraction and heat release. This peak can also be found in the pressure spectra but it is weaker than the longitudinal acoustic modes. This response at high frequency corresponds to the hydrodynamic Precessing Vortex Core (PVC) mode, the characteristics of which were introduced by Syred [11]. The representative responses of pressure, fuel and heat release fluctuations at PVC frequency are shown in Fig. 71. Evidence of a strong swirling flow can be seen in the cross-sectional view of each variable. The flow swirls at a high rate azimuthally while, in the axial direction, the top and bottom distributions are observed to be out-of-phase, which indicates a swirling core pattern in the diverging section. The influence of the PVC mode on the acoustic field is mainly concentrated in the diverging section and has a much weaker effect on the acoustic field in the combustor downstream of the dump plane. The helical

wave present in the pressure mode shape indicates that the flow dynamics plays a more important role on the pressure than acoustics. More importantly, this strong swirling mode can be responsible for the high azimuthal velocity state when pressure is high in the chamber head section and inlet axial velocity is low (Fig. 65), during which swirling effects are expected to be dominant.

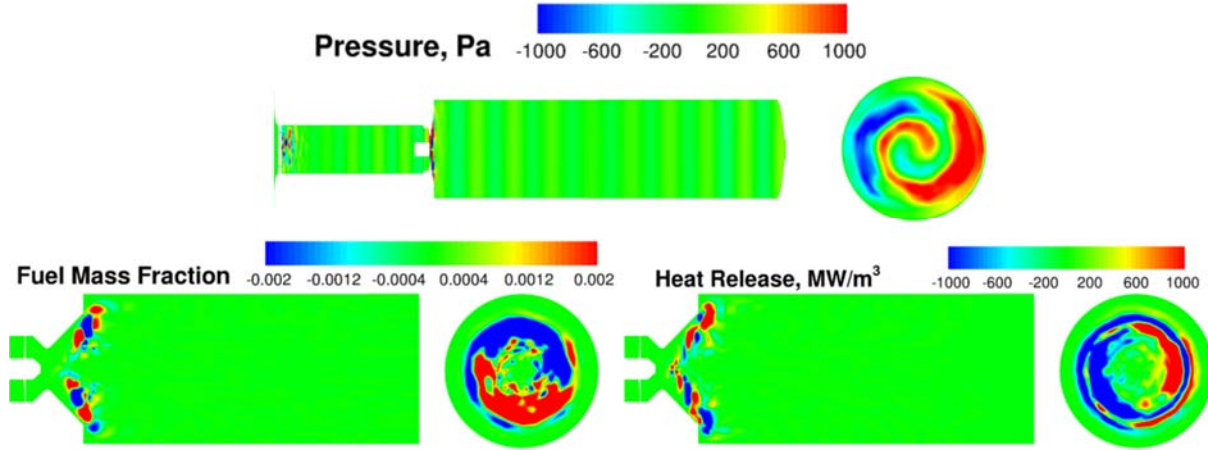


Figure 71. Representative reconstructed DMD responses at PVC1 frequency for closed geometry simulation for  $\phi = 0.36$   $T_{\text{air}} = 800\text{K}$  (fluctuations of top: pressure; bottom left: fuel mass fraction; bottom right: heat release).

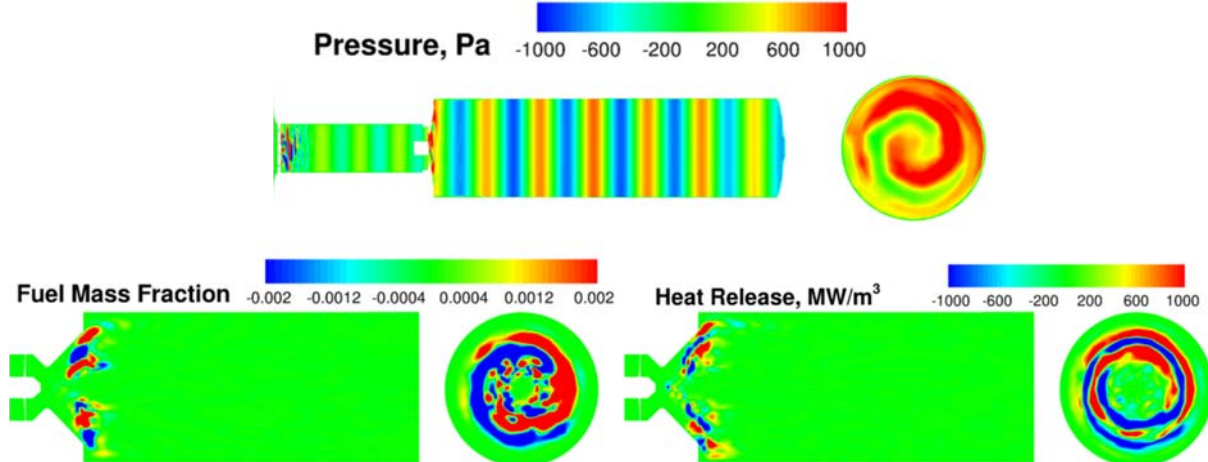


Figure 72. Representative reconstructed DMD responses at nonlinear coupled frequency for closed geometry simulation for  $\phi = 0.36$   $T_{\text{air}} = 800\text{K}$  (fluctuations of top: pressure; bottom left: fuel mass fraction; bottom right: heat release).

In the single LDI element configuration, the presence of hydrodynamic responses due to geometric effects and flow conditions can also potentially interact with the acoustic field in the combustor through nonlinear coupling. The evidence of that can be inferred from the peak standing at 4.6 kHz in the DMD frequency spectrum shown in Fig. 68. That frequency is close to the difference between PVC and 6L frequencies ( $f_{\text{nonlinear}} = f_{\text{PVC}} - f_{\text{6L}}$ ). The presence of nonlinear coupling in a premixed swirling flow combustor was discussed by Palies et al. [13, 14]. Representative responses at the nonlinear coupled frequency are shown in Fig. 72. Both the characteristics of longitudinal acoustic modes and PVC modes can be found in the plots. In the three cross-sectional views in Fig. 72, dominant swirling motions can be identified, which suggest

the influence of flow field. In the sectional views, pressure shows a clear 13L mode shape in the combustor and, unlike the PVC modes, in Fig. 72, an equal weighting between the longitudinal acoustics and the PVC pressure mode can be observed here. For the fuel mass fraction and heat release, the influence of the acoustic modes is not easily identifiable and the spatial distributions of both still follow a swirling pattern with some compression in the axial direction, which might suggest potential acoustics coupling.

#### 4.6.2.3. Rayleigh Index Analysis

A Rayleigh index [71] frequency spectrum is established using DMD modes from part 4.6.2.2 as a measurement of the couplings between pressure and heat release oscillations. Local values of Rayleigh index are calculated using each individual DMD mode, which contains single frequency content,

$$\Re(f_k, x_i) = \frac{1}{T} \int_{t_0}^{t_0+T} p'(f_k, x_i, t) \dot{q}'(f_k, x_i, t) dt \quad (23).$$

The calculated Rayleigh index is integrated over the whole computation domain to obtain a total measurement at each frequency and generate the index spectrum as shown in Fig. 73,

$$\Re_{\text{total}}(f_k) = \frac{\int \Re(f_k, x) dx}{V} \quad (24).$$

The Rayleigh index frequency spectrum provides a direct measurement of driving (+ index)/damping (- index) between pressure and heat release at each frequency. Most of the indices are positive at frequencies ranging from 200 to 8000Hz, which indicates that heat release is being added during pressure rise and combustion and acoustics are driving each other. 5L and 6L are the two most dominant peaks found in the spectrum, consistent with the PSD analysis in Fig. 50 and DMD frequency spectrum in Fig. 68, which confirms that in this single-element LDI combustor, heat is being added in such a way to drive higher acoustic modes. A 1L peak is also identifiable but 1.5 order-of-magnitude lower in index level than 5L/6L. The third strongest peak in Rayleigh index spectrum is observed at the PVC frequency, which indicates driving from the strong swirling dynamics in the diverging venturi identified in Fig. 71.

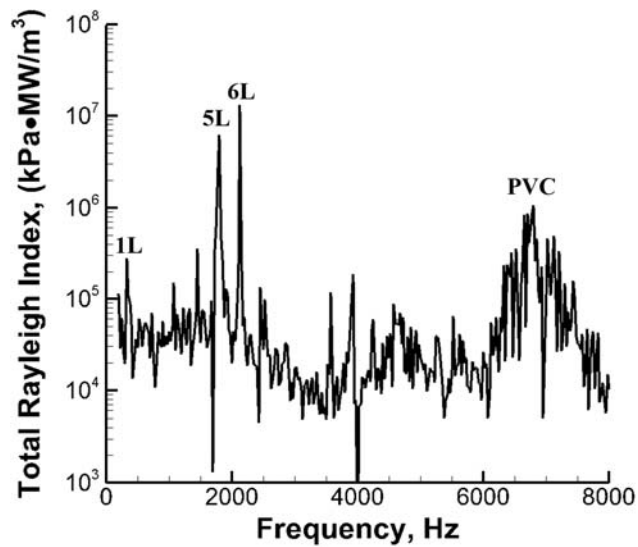


Figure 73. Rayleigh index spectrum of the closed geometry simulation for  $\phi = 0.36$   $T_{\text{air}} = 800\text{K}$ .

Rayleigh index spatial distributions are investigated in details at frequencies highlighted in Fig. 73 and are shown in Fig. 74. Three axial locations are selected to visualize the three dimensional effects. Rayleigh indices at longitudinal frequencies (1L, 5L and 6L) show similar spatial distributions with main damping region (-) in between two major driving regions (+) and damping effects are more dominant upstream close to the fuel injector while most of the driving region are found more downstream close to the dump plane. Also it appears that most of the pressure and heat release couplings are observed in between axial locations 2 and 3, where the vortex bubble is approximately located. But it should also be noted that the axial distribution of Rayleigh indices gets more compact as it goes to higher acoustic modes, which can be attributed to the fact that the scale of vortex bubble decreases and bubble contraction/growth rate is higher at higher VBB modes as discussed in part 4.6.1 and in part 4.6.2 (4.6.2.1 & 4.6.2.2), it is postulated that those higher VBB modes are driving higher acoustic modes. In that way, the couplings between pressure and heat release are expected to be more spatially compact at higher frequencies. Moreover, Rayleigh index at 1L shows comparable driving and damping regions while 5L and 6L show more driving than damping, which helps explain why 1L is not as dominant as 5L and 6L. The Rayleigh index at PVC frequency is different from the other three. The correlations between pressure and heat release oscillations are high close to the throat (between location 1 and 2) while get weaker as it goes downstream. This indicates the swirling effects observed in Fig. 71 are dominant at the inner section of the diverging part while acoustic effects are stronger at the outer section close to the chamber.

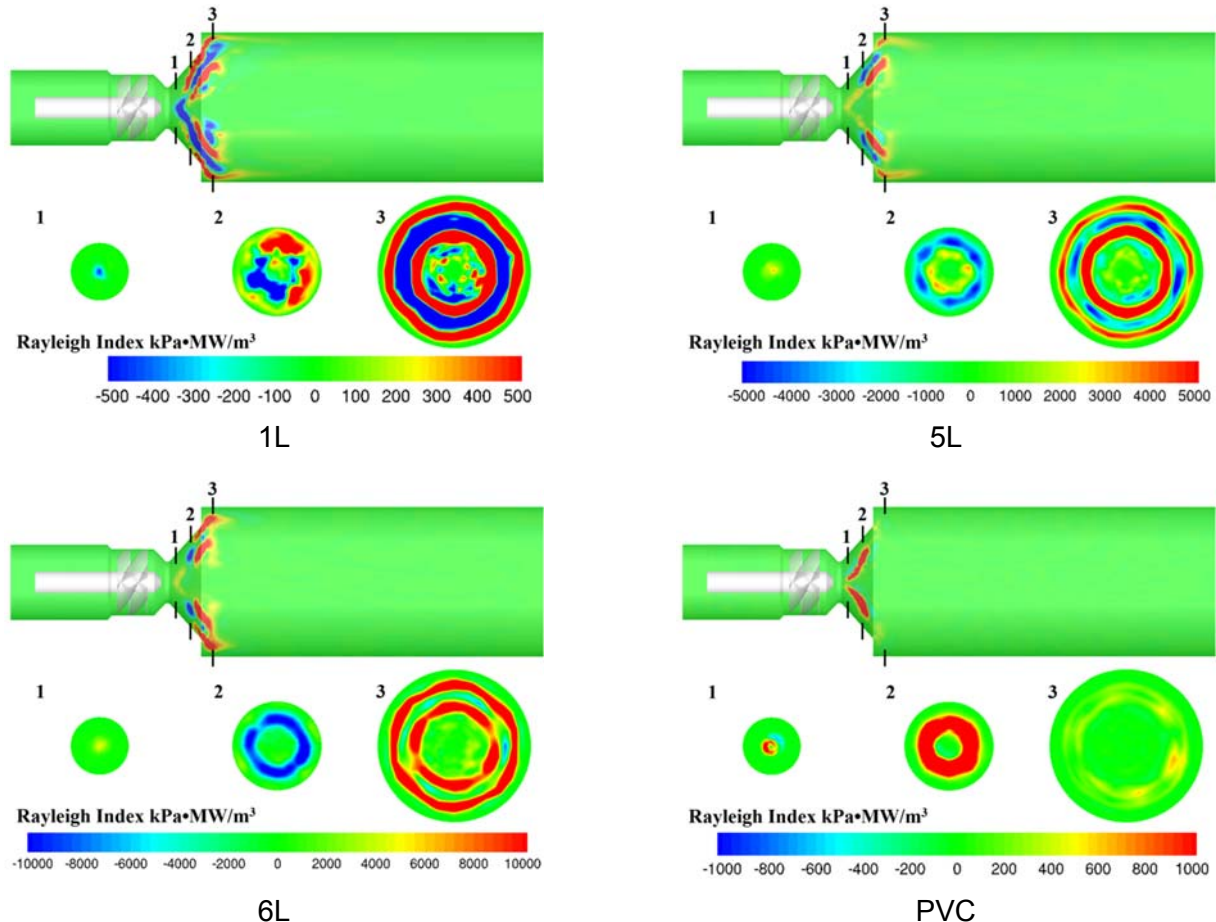


Figure 74. Spatial distribution of Rayleigh index at specific frequencies highlighted in Fig. 73.

## 5. CONCLUSIONS AND RECOMMENDATIONS

A concurrent effort comprising simulation and experiment was undertaken to assess the ability of high-fidelity models to predict combustion dynamics in lean-burning systems. Initial project goals included assessment of the simulation at pressure oscillation levels of about 1% of mean pressure, and at a frequency of about 400 Hz. To ensure the same physics were represented in the experiment and the simulation, strict requirements were placed on self-excitation, boundary conditions, and measurement accuracy. A prototypical lean-direct-inject combustor was designed in a modular configuration so that a suitable geometry could be found by test. The combustor comprised a variable length air plenum and combustion chamber, air swirler, and fuel nozzle located inside a subsonic venturi. The venturi cross section and the fuel nozzle were consistent with previous studies.

Test pressure was 1 MPa and variables included geometry and acoustic resonance, inlet temperatures, equivalence ratio, and type of liquid fuel. High-frequency pressure measurements in a well-instrumented metal chamber yielded frequencies and mode shapes as a function of inlet air temperature, equivalence ratio, fuel nozzle placement, and combustor acoustic resonances. The parametric survey was a significant effort, with over 100 tests on eight geometric configurations. A good dataset was obtained that could be used for both operating-point-dependent quantitative comparisons, and testing the ability of the simulation to predict more global trends.

Results showed a very strong dependence of instability amplitude on the geometric configuration of the combustor, i.e., its acoustic resonance characteristics, with measured pressure fluctuation amplitudes ranged from 5 kPa (0.5% of mean pressure) to 200 kPa (~20% of mean pressure) depending on combustor geometry. The stability behavior also showed a consistent and pronounced dependence on equivalence ratio and inlet air temperature. Instability amplitude increased with higher equivalence ratio and with lower inlet air temperature. Target amplitudes and frequencies were reached at an air inlet temperature of 800 K and an equivalence ratio <0.45; this point was used for many of the comparisons.

At higher equivalence ratio, where the combustor was relatively unstable, bands of modes around 1400 Hz and 6 kHz were prevalent, with the 4L mode typically being the most dominant mode. At the most stable conditions, near lean blow-out, acoustic energy was distributed across several (1L-5L) low amplitude modes. An increase in the 1L mode amplitude coincided with the reduction in strength of the other modes. A strong modulation in the dynamic pressure is present, with oscillations ranging from 0.5% to 2% of mean pressure. The difference in the energy spectrum between the high-equivalence-ratio cases, with a dominant 4L mode, and the low equivalence ratio case with more dispersed modal energy provided a good test for the simulation. A pronounced effect of fuel nozzle location on the combustion dynamics was also observed. Combustion instabilities with the fuel nozzle at the throat of the venturi throat were stronger than in the configuration with fuel nozzle 2.6 mm upstream of the nozzle.

A second set of dynamics data was based on high-response-rate laser-based combustion diagnostics using an optically accessible combustor section. High-frequency measurements of OH\*-chemiluminescence and OH-PLIF and velocity fields using PIV were obtained at a relatively stable, low equivalence ratio case and a less stable case at higher  $\phi$ . A gradient-based edge detection routine was used to extract the flame-front location from the OH-PLIF images. Planar flame surface density calculated using the extracted flame-front showed a compact flame ( $L_f \sim 25$  mm) at  $\phi=0.6$  and a more diffuse flame ( $L_f \sim 35$  mm) at  $\phi=0.44$ . Dynamic mode decomposition analysis of the flame front shows a strong flame response at the 4L and 8L acoustic mode frequencies for  $\phi=0.6$  and at the 3L frequency for  $\phi=0.44$ , while a response at the other acoustic

mode frequencies is not captured. PIV measurements were performed at 5 kHz for non-reacting flow but glare from the cylindrical quartz chamber limited the field of view to a small region in the combustor. Full data analysis of the OH-PLIF and PIV measurements and comparisons with the simulation results have not been completed.

A phase Doppler particle analyzer (PDPA) was used to measure the drop size distribution and droplet velocities for an unconfined spray at atmospheric pressure. The measurements were performed with and without a co-flow of air around the fuel nozzle. Drop sizes of 15-70  $\mu\text{m}$ , axial droplet velocities up to 15 m/s and a spray cone angle of 68-70° were measured. Simulations at the conditions of the spray experiment were performed in which the measured spray cone angle and drop sizes were input to the model. Use of atmospheric pressure drop size measurements as input to the simulation did not provide the results that matched the high pressure, reacting flow measurements. Good spray measurements for the multi-distillate fuels used in this study at high pressure, reacting flow conditions are needed to provide appropriate data for model validations.

The computational framework used for the assessment was the General Equation and Mesh Solver (GEMS). More than 15 two-dimensional cases were run for parametric preliminary assessment of the code's predictive capability. A total of 25 three-dimensional cases were run using configurations consistent with experiment (two fuel nozzle locations and three equivalence ratios). Another five three-dimensional cases were run with an unconfined geometry to study the hydrodynamic effects. Two cases at  $\phi=0.36$  and 0.60 are still running with an 18-reaction-set kinetics model and will provide results for comparison with simulations using two-step global reactions.

Quantitative and qualitative comparisons were made for five different combinations of geometry and operating condition that yielded discriminating stability behavior in the experiment. Comparisons were made on the basis of trends and pressure mode data. Submodels for chemical kinetics and primary and secondary atomization were also tested against the measured behavior. Replacing the primary breakup model with a specified spray drop distribution and applying moderate adjustment in the distribution had a significant effect on the prediction. Hence, for a limited range of application, a simple and efficient model could potentially give good results. The predictions can be very sensitive to the stipulated distribution and its adjustment needs to be performed carefully to reach good agreement with the measurement. It is important to understand the limits of the model's applicability. Any model should be tested against the most relevant experimental data available.

Preliminary results from a simulation using an 18-reaction kinetics model indicated that the predicted pressure oscillation amplitude is closer to measurement but a bit under-predicted. Similar to the experiment, the 4L acoustic mode is dominant at higher equivalence ratio. The simulation predicts similar strength of the 5L mode, which is not observed in the simulation using two-step chemistry or the experiment. A higher number of predicted modes may be a consequence of the finer gradients calculated with the detailed reaction set.

Results from the simulation were used to study potential instability mechanisms. Dynamic mode decomposition (DMD) analysis of simulations of an "open-domain" combustor with presumably weak acoustic influences indicated the presence of a vortex breakdown bubble (VBB) mode, with a distinct response in the range around 1400 Hz, near the same frequency where the highest pressure oscillations were measured in the combustor. The VBB has strong spatial and temporal character and represents the contour of a surface representing local flow stagnation, with high potential for strong modal (temporal and spatial) interactions with the combustor thermoacoustics. The DMD analysis also showed that the pressure oscillations measured around 6-8 kHz were due to strong and dynamic swirling behavior in the diverging section of the venturi, i.e., a Precessing Vortex Core (PVC) instability. Guided by other investigations of premixed

gaseous fuel swirl combustors, nonlinear coupling between the dominant acoustic modes (5L/6L) and the PVC hydrodynamic mode was speculated to be the source of the generally weak pressure oscillations around 4.6 kHz, whose relative strength was highest for the case of the fuel nozzle located at the throat and high  $\phi$ . In addition to providing insight to mechanisms, this information can be used to conduct improved experiments that provide a better test of the simulation.

Investigation of the coupling mechanisms continued with analyzing the simulation results to calculate heat release and pressure modes. These were then used to calculate the Rayleigh index spectrum, which was used to identify sources and sinks according to the Rayleigh criterion at 1L, 5L/6L, and PVC frequencies. Axial slices of the Rayleigh index showed complex and highly-three dimensional reacting flow in the diverging section of the venturi.

Overall, the ability of the simulation to match experimental data and trends was encouraging. For a point-wise comparison, at the low equivalence ratio baseline condition the predicted instability amplitude was 14.5 kPa compared to the measured value of 20 kPa. More generally, the dependence on equivalence ratio was matched. Another important area of general agreement was that both experiment and simulation typically presented a bimodal distribution of acoustic modes usually centered around 1400 and 6000 Hz. Although the exact modal energy distribution was not matched, the dominance of a few modes or bands was seen in both experiment and simulation for high-amplitude instabilities. The flatter distribution of energy over more modes at low amplitudes was also seen in both experiment and simulation.

One trend that could not be matched was the effect of a change in the fuel nozzle placement. Whereas measurements indicated greater stability when the fuel nozzle was located slightly upstream of the throat of the subsonic venturi, the simulations predicted very stable behavior when the nozzle was located at the throat. Since the conditions in the throat are very dynamic and can have a strong effect on the Weber-number adaptive submodels that are used for secondary atomization, a more detailed study on the effect on the choice of atomization model was conducted. The results showed that a fixed input drop size could provide a better match of instability amplitude, whereas predictions using the We-number adaptive models gave better results with respect to the energy distribution of the dominant acoustic modes. These and other results strongly indicate the importance and necessity of reliable and validated *a priori* models of atomization.

The simulations predicted reasonable pressure amplitudes and captured the dominant acoustic frequencies measured in the experiments for both high and low equivalence ratios when the fuel nozzle is upstream of the throat, but did not capture the high frequency modes between 6 and 8 kHz. Larger disagreement between experiment and simulation is observed when fuel nozzle at the throat. It is speculated that at least some of this disagreement may be due to the Weber-number-adaptive models that may be overly sensitive to the strong dynamics in the throat region.

The results from the spray modeling study point to the need for more directly coupled *ab initio* models of the atomizer free surface flow and the primary atomization processes, thereby avoiding *ad hoc* assumptions of droplet distributions that are likely to be problem-dependent. In the near-term, and for limited ranges of operation, the use of two-constant empirical models (like We-dependent mean drop size and a stipulated shape of distribution) should be explored. Time- and space-resolved measurements of drop size distributions in a dynamic, high-pressure, reacting flow are needed to test all the models. Although it was not part of this study, the use of turbulent combustion models, such as Dynamic Thickened Flame models or flamelet models should be considered in future studies.

Based on preliminary results, comparisons between the optical measurements and the simulation were not as useful as was initially hoped. First and foremost, the complexity of the

highly intermittent and three-dimensional flow with strong swirl dynamics greatly complicates the interpretation of the two-dimensional images; reliable methods for analyzing the planar image for comparison to simulation need to be developed. Because the comparisons are made on the basis of OH concentration, detailed kinetics models must be used in the simulations and they must be validated in the range of equivalence ratios used in the experiment. Sampling even at 10 kHz provided marginal temporal resolution of swirling instabilities in the few kHz range. Furthermore, for the LDI configuration, much of the combustion occurs in the diverging section of the venturi, which was not accessible in this study. Fiber-optic-based emission measurements at key locations in the diverging section should be considered to confirm the precessing vortex core instability that was conjectured to be the source of the 6-8 kHz instabilities. Particle image velocimetry (PIV) may be the best direct method to test the simulations with regards to the VBB dynamics that were conjectured as being dominant in this study.

Complex nonlinear coupling processes between heat release, acoustics, and hydrodynamics have been shown to exist in premixed-gas, sudden-expansion combustors with swirl. The swirling, expanding flows in the diverging venturi section with complicated acoustic reflections may be introducing physics that are not easy to detect or understand. A systematic variation in geometry and swirl number that includes the sudden expansion used in most configurations may lead to a better understanding of these effects in the LDI configuration. A gaseous fuel should be used at first to eliminate the complicated and complex behavior that comes from atomization, vaporization, and drop transport. Future experiments should use test hardware designed for adiabatic operation so that the conditions in the simulations are better matched.

## 6. WORK IN PROGRESS

1. As mentioned in the report, a mistake in the two-step global chemical model is found and needs to be corrected to evaluate the effects in predicting the combustion instability. Two simulations are in progress at both high ( $\phi = 0.6$ ) and low ( $\phi = 0.36$ ) equivalence ratios as reference.
2. The simulations with 18-step chemistry are also in progress due to the heavy computational cost required for more detailed chemical model.
3. Once the simulation is done with more detailed chemical model, the predicted OH species can be used to compare with the measured OH-PLIF image directly to provide high quality validation for simulation results. Methods for comparisons are also included in future to explore the potential use of OH-PLIF images.
4. A coupled level-set/VOF approach is planned for implementation in GEMS to capture the free surface flow dynamics and its interaction with acoustic perturbation to provide higher fidelity predictions.
5. OH-PLIF measurements at 10 kHz repetition rates have been presented in this report. PIV measurements, non-reacting and with combustion, are currently in progress. Use of a circular cross-section poses challenges to performing PIV easily. In the circular chamber, the glare from the laser sheet reflects off the cylindrical surface and saturates the camera. These issues are currently being worked on.
6. The PIV measurements that are currently being performed will be followed by simultaneous OH-PLIF and PIV measurements at 10 KHz along with 100 kHz pressure measurements. These will be used for final comparisons with the simulation data.

## 7. PUBLICATIONS

### ***Conference Papers***

Yoon, C., Gejji, R., and Anderson, W., "Computational Investigation of Combustion Dynamics in a Lean Direct Inject Gas Turbine Combustor," AIAA-2013-0166, 51<sup>st</sup> AIAA Aerospace Sciences Meeting, Grapevine, TX, January 7-10.

Yoon, C., Gejji, R., Anderson, W., and Sankaran, V., "Effects of Fuel Spray Modeling on the Combustion Dynamics of Lean Direct Inject Model Combustor," ILASS-Americas 25<sup>th</sup> Annual Conference on Liquid Atomization and Spray Systems, Pittsburgh, PA, May 2013.

Gejji, R., Yoon, C., Sankaran, V., and Anderson, W., "A Parametric Study of Combustion Dynamics in a Single-Element Lean Direct Inject Gas Turbine Combustor: Part II, Experimental Investigation," AIAA-2014-0133, 52<sup>nd</sup> Aerospace Sciences Meeting, National Harbor, MD.

Huang, C., Yoon, C., Gejji, R., Anderson, W., and Sankaran, V., "Computational Study of Combustion Dynamics in a Single-Element Lean Direct Inject Gas Turbine Combustor," AIAA-2014-0620, 52<sup>nd</sup> Aerospace Sciences Meeting, National Harbor, MD.

Huang, C., Gejji, R., Anderson, W., Yoon, C., and Sankaran, V., "Combustion Dynamics Behavior in a Single-Element Lean Direct Injection (LDI) Gas Turbine Combustor," AIAA-2014-3433, 50<sup>th</sup> AIAA/ASME/SAE/ASEE Joint Propulsion Conference, Cleveland OH.

Huang, C., Gejji, R., Anderson, W., "Effects of Physical Modeling on Combustion Instability Predictions in a Single-Element Lean Direct Injection Gas Turbine Combustor," AIAA-2015-1569, 53<sup>rd</sup> Aerospace Sciences Meeting, Kissimmee, FL.

### ***Student Theses***

Huang, Cheng, PhD Thesis, "Multi-fidelity Computational Analysis of Combustion Instability", Purdue University, 2015.

Gejji, Rohan, PhD Thesis, "Experimental Investigation of Self-Excited Combustion Dynamics in a Lean Direct Inject (LDI) Combustor", Purdue University, 2015.

## REFERENCES

1. Abramzon, B. and W.A. Sirignano, Int. J. Heat Mass Transfer, 1989. **32**(9): p. 1605.
2. Awad, E. and F. Culick, Combust. Sci. Technol., 1986. **46**: p. 195.
3. Zellhuber, M., et al., *Experimental and numerical investigation of thermoacoustic sources related to high-frequency instabilities*. International Journal of Spray and Combustion Dynamics, 2014. **6**(1): p. 1-34.
4. Andrews, G.E., et al., *High-Intensity Burners with Low Nox Emissions*. Proceedings of the Institution of Mechanical Engineers, Part A: Journal of Power and Energy, 1992. **206**(1): p. 3-17.
5. Alkabie, H., G. Andrews, and N. Ahmad. *Lean Low NO<sub>x</sub> Primary Zones Using Radial Swirlers*, paper ASME 88-GT-245. in *ASME Gas Turbine and Aero Engine Congress and Exposition*. 1988.
6. Yi, T. and D.A. Santavicca, *Flame Spectra of a Turbulent Liquid-Fueled Swirl-Stabilized Lean-Direct Injection Combustor*. Journal of Propulsion and Power, 2012. **25**(5): p. 1058-1067.
7. Yi, T. and D.A. Santavicca, *Combustion Instability in a Turbulent Liquid-Fueled Swirl-Stabilized LDI Combustor*, in *45th AIAA/ASME/SAE/ASEE Joint Propulsion Conference & Exhibit*. 2009, American Institute of Aeronautics and Astronautics.
8. Yi, T. and D.A. Santavicca, *Flame Spectra of a Turbulent Liquid-Fueled Swirl-Stabilized LDI Combustor*, in *47th AIAA Aerospace Sciences Meeting including The New Horizons Forum and Aerospace Exposition*. 2009, American Institute of Aeronautics and Astronautics.
9. Bourguin, J.-F., et al., *Sensitivity of swirling flows to small changes in the swirl geometry*. Comptes Rendus Mécanique, 2013. **341**(1–2): p. 211-219.
10. Moeck, J.P., et al., *Nonlinear interaction between a precessing vortex core and acoustic oscillations in a turbulent swirling flame*. Combustion and Flame, 2012. **159**(8): p. 2650-2668.
11. Syred, N., *A review of oscillation mechanisms and the role of the precessing vortex core (PVC) in swirl combustion systems*. Progress in Energy and Combustion Science, 2006. **32**(2): p. 93-161.
12. Candel, S., et al., *Progress and challenges in swirling flame dynamics*. Comptes Rendus Mécanique, 2012. **340**(11–12): p. 758-768.
13. Palies, P., et al., *Nonlinear combustion instability analysis based on the flame describing function applied to turbulent premixed swirling flames*. Combustion and Flame, 2011. **158**(10): p. 1980-1991.
14. Palies, P., et al., *The combined dynamics of swirl and turbulent premixed swirling flames*. Combustion and Flame, 2010. **157**(9): p. 1698-1717.
15. Stöhr, M., C.M. Arndt, and W. Meier, *Effects of Damköhler number on vortex–flame interaction in a gas turbine model combustor*. Proceedings of the Combustion Institute, 2013. **34**(2): p. 3107-3115.
16. Stöhr, M., R. Sadanandan, and W. Meier, *Phase-resolved characterization of vortex–flame interaction in a turbulent swirl flame*. Experiments in Fluids, 2011. **51**(4): p. 1153-1167.

17. Stöhr, M., et al., *Dynamics of lean blowout of a swirl-stabilized flame in a gas turbine model combustor*. Proceedings of the Combustion Institute, 2011. **33**(2): p. 2953-2960.
18. Kim, K.T. and D.A. Santavicca, *Interference mechanisms of acoustic/convective disturbances in a swirl-stabilized lean-premixed combustor*. Combustion and Flame, 2013. **160**(8): p. 1441-1457.
19. de la Cruz García, M., E. Mastorakos, and A.P. Dowling, *Investigations on the self-excited oscillations in a kerosene spray flame*. Combustion and Flame, 2009. **156**(2): p. 374-384.
20. Cheng, H., et al., *Combustion Dynamics Behavior in a Single-Element Lean Direct Injection (LDI) Gas Turbine Combustor*, in *50th AIAA/ASME/SAE/ASEE Joint Propulsion Conference*. 2014, American Institute of Aeronautics and Astronautics.
21. Cheng, H., et al., *Computational Study of Combustion Dynamics in a Single-Element Lean Direct Injection Gas Turbine Combustor*, in *52nd Aerospace Sciences Meeting*. 2014, American Institute of Aeronautics and Astronautics.
22. Yu, Y.C., et al., *Effects of Mean Flow, Entropy Waves, and Boundary Conditions on Longitudinal Combustion Instability*. Combustion Science and Technology, 2010. **182**(7): p. 739-776.
23. Yen, Y., et al., *Examination of Spatial Mode Shapes and Resonant Frequencies Using Linearized Euler Solutions*, in *37th AIAA Fluid Dynamics Conference and Exhibit*. 2007, American Institute of Aeronautics and Astronautics.
24. Portillo, J., et al., *Application of a Generalized Instability Model to a Longitudinal Mode Combustion Instability*, in *43rd AIAA/ASME/SAE/ASEE Joint Propulsion Conference & Exhibit*. 2007, American Institute of Aeronautics and Astronautics.
25. Yoon, C., Gejji, R., and Anderson, W., *Computational Investigation of Combustion Dynamics in a Lean Direct Injection Gas Turbine Combustor*, in *51st AIAA Aerospace Sciences Meeting including the New Horizons Forum and Aerospace Exposition*. 2013, American Institute of Aeronautics and Astronautics.
26. Boxx, I., C.D. Carter, and W. Meier, *On the feasibility of tomographic-PIV with low pulse energy illumination in a lifted turbulent jet flame*. Experiments in Fluids, 2014. **55**(8): p. 1-17.
27. Eckbreth, A.C., *Laser Diagnostics for Combustion Temperature and Species*. 1996: Taylor & Francis.
28. Frank, J., M. Miller, and M. Allen, *Imaging of laser-induced fluorescence in a high-pressure combustor*, in *37th Aerospace Sciences Meeting and Exhibit*. 1999, American Institute of Aeronautics and Astronautics.
29. Salgues, D., et al., *Shear and Swirl Coaxial Injector Studies of LOX/GCH4 Rocket Combustion Using Non-Intrusive Laser Diagnostics*, in *44th AIAA Aerospace Sciences Meeting and Exhibit*. 2006, American Institute of Aeronautics and Astronautics.
30. Stopper, U., et al., *Experimental study of industrial gas turbine flames including quantification of pressure influence on flow field, fuel/air premixing and flame shape*. Combustion and Flame, 2013. **160**(10): p. 2103-2118.
31. Sadanandan, R., W. Meier, and J. Heinze, *Experimental study of signal trapping of OH laser induced fluorescence and chemiluminescence in flames*. Applied Physics B, 2012. **106**(3): p. 717-724.

32. Weber, V., et al., *Pixel-based characterisation of CMOS high-speed camera systems*. Applied Physics B, 2011. **103**(2): p. 421-433.
33. Sweeney, M. and S. Hochgreb, *Autonomous extraction of optimal flame fronts in OH planar laser-induced fluorescence images*. Applied Optics, 2009. **48**(19): p. 3866-3877.
34. Sadanandan, R., M. Stöhr, and W. Meier, *Simultaneous OH-PLIF and PIV measurements in a gas turbine model combustor*. Applied Physics B, 2008. **90**(3-4): p. 609-618.
35. Slabaugh, C.D., A.C. Pratt, and R.P. Lucht, *Simultaneous 5 kHz OH-PLIF/PIV for the study of turbulent combustion at engine conditions*. Applied Physics B, 2014: p. 1-22.
36. Boxx, I., et al., *3&#xa0;kHz PIV/OH-PLIF measurements in a gas turbine combustor at elevated pressure*. Proceedings of the Combustion Institute, (0).
37. Li, D., et al. *Computational framework for complex fluids applications*. in *3rd International Conference on Computational Fluid Dynamics, Toronto, Canada*. 2004.
38. Lian, C. and C. Merkle, *Contrast Between Steady and Time-Averaged Unsteady Combustion Simulations*, in *48th AIAA Aerospace Sciences Meeting Including the New Horizons Forum and Aerospace Exposition*. 2010, American Institute of Aeronautics and Astronautics.
39. Lian, C., G. Xia, and C. Merkle, *Impact of Source Terms on Reliability of CFD Algorithms*, in *19th AIAA Computational Fluid Dynamics*. 2009, American Institute of Aeronautics and Astronautics.
40. Matthew, E.H., et al., *Combustion Instability Mechanisms in a Pressure-coupled Gas-gas Coaxial Rocket Injector*, in *49th AIAA/ASME/SAE/ASEE Joint Propulsion Conference*. 2013, American Institute of Aeronautics and Astronautics.
41. Matthew, H., A. William, and M. Charles, *Combustion Instability Diagnostics Using the Rayleigh Index*, in *47th AIAA/ASME/SAE/ASEE Joint Propulsion Conference & Exhibit*. 2011, American Institute of Aeronautics and Astronautics.
42. Smith, R., et al., *Extraction of Combustion Instability Mechanisms from Detailed Computational Simulations*, in *48th AIAA Aerospace Sciences Meeting Including the New Horizons Forum and Aerospace Exposition*. 2010, American Institute of Aeronautics and Astronautics.
43. D. Basu, A.A., K. Das. *DES, Hybrid RANS/LES and PANS Models for Unsteady Separated Turbulent Flow Simulations*. in *ASME 2005 Fluids Engineering Division Summer Meeting*. 2005. Houston, Texas, USA.
44. Baurle, R.A., et al., *Hybrid Simulation Approach for Cavity Flows: Blending, Algorithm, and Boundary Treatment Issues*. AIAA Journal, 2003. **41**(8): p. 1463-1480.
45. Travin, A., et al., *Physical and Numerical Upgrades in the Detached-Eddy Simulation of Complex Turbulent Flows*, in *Advances in LES of Complex Flows*, R. Friedrich and W. Rodi, Editors. 2002, Springer Netherlands. p. 239-254.
46. Wilcox, D.C., *Turbulence Modeling for CFD*. 1994: DCW Industries, Incorporated.
47. Westbrook, C.K. and F.L. Dryer, *Simplified Reaction Mechanisms for the Oxidation of Hydrocarbon Fuels in Flames*. Combustion Science and Technology, 1981. **27**(1-2): p. 31-43.
48. Ajmani, K., K. Kundu, and P. Penko, *A Study on Detonation of Jet-A Using a Reduced Mechanism*, in *48th AIAA Aerospace Sciences Meeting Including the New Horizons*

*Forum and Aerospace Exposition.* 2010, American Institute of Aeronautics and Astronautics.

49. Putnam, A., *Integrable form of Droplet Drag Coefficient*. ARS Journal, 1961. **31**(10): p. 1466-1469.
50. Yoon, C., et al., *Computational Investigation of Combustion Instabilities in a Laboratory-Scale LDI Gas Turbine Engine*, in *49th AIAA/ASME/SAE/ASEE Joint Propulsion Conference*. 2013, American Institute of Aeronautics and Astronautics.
51. Ibrahim, A.A. and M.A. Jog, *Nonlinear Breakup Model for a Liquid Sheet Emanating From a Pressure-Swirl Atomizer*. Journal of Engineering for Gas Turbines and Power, 2007. **129**(4): p. 945-953.
52. Senecal, P., et al., *Modeling high-speed viscous liquid sheet atomization*. International Journal of Multiphase Flow, 1999. **25**(6): p. 1073-1097.
53. O'Rourke, P.J. and A.A. Amsden, *The TAB method for numerical calculation of spray droplet breakup*. 1987, SAE Technical Paper.
54. Beale, J.C. and R.D. Reitz, *Modeling spray atomization with the Kelvin-Helmholtz/Rayleigh-Taylor hybrid model*. Atomization and sprays, 1999. **9**(6).
55. Patterson, M.A. and R.D. Reitz, *Modeling the effects of fuel spray characteristics on diesel engine combustion and emission*. 1998, SAE Technical Paper.
56. Han, Z., et al., *Modeling atomization processes of pressure-swirl hollow-cone fuel sprays*. Atomization and Sprays, 1997. **7**(6).
57. Reitz, R.D., *Modeling atomization processes in high-pressure vaporizing sprays*. Atomisation Spray Technology, 1987. **3**: p. 309-337.
58. Gejji, R.M., et al., *A Parametric Study of Combustion Dynamics in a Single-Element Lean Direct Injection Gas Turbine Combustor: Part II: Experimental Investigation*, in *52nd Aerospace Sciences Meeting*. 2014, American Institute of Aeronautics and Astronautics.
59. Benjamin, T.B., *Theory of the Vortex Breakdown Phenomenon*. Journal of Fluid Mechanics, 1962. **14**(4): p. 593-629.
60. Billant, P., J.-M. Chomaz, and P. Huerre, *Experiment study of vortex breakdown in swirling jets.pdf*. Journal of Fluid Mechanics, 1998. **376**: p. 183-219.
61. Hall, M.G., *Vortex Breakdown*. Annu. Rev. Fluid Mech., 1972. **4**: p. 195-218.
62. Liang, H. and T. Maxworthy, *An experimental investigation of swirling jets*. Journal of Fluid Mechanics, 2005. **525**: p. 115-159.
63. Paschereit, C.O., E. Gutmark, and W. Weisenstein, *Excitation of Thermoacoustic Instabilities by Interaction of Acoustics and Unstable Swirling Flow*. AIAA Journal, 2000. **38**(6): p. 1025-1034.
64. Oberleithner, K., et al., *Three-dimensional coherent structures in a swirling jet undergoing vortex breakdown: stability analysis and empirical mode construction*. Journal of Fluid Mechanics, 2011. **679**: p. 383-414.
65. Ruith, M.R., et al., *Three-dimensional vortex breakdown in swirling jets and wakes: direct numerical simulation*. Journal of Fluid Mechanics, 2003. **486**: p. 331-378.
66. Huang, Y., S. Wang, and V. Yang, *Systematic Analysis of Lean-Premixed Swirl-Stabilized Combustion*. AIAA Journal, 2006. **44**.

67. Poinsot, T.J., et al., *Vortex-driven acoustically coupled combustion instabilities*. Journal of Fluid Mechanics, 1987. **177**: p. 265-292.
68. O'Connor, J. and T. Lieuwen, *Recirculation zone dynamics of a transversely excited swirl flow and flame*. Physics of Fluids, 2012. **24**(7): p. 075107.
69. Schmid, P.J., *Dynamic mode decomposition of numerical and experimental data*. Journal of Fluid Mechanics, 2010. **656**: p. 5-28.
70. Cheng, H., et al., *Analysis of Self-Excited Combustion Instability using Decomposition Techniques*, in *51st AIAA Aerospace Sciences Meeting including the New Horizons Forum and Aerospace Exposition*. 2013, American Institute of Aeronautics and Astronautics.
71. Strutt, J. W., *Theory of Sound*: V. 2. 1900: Dover Publications.